

# Spin polarization and attosecond time delay in photoemission from solids

THÈSE N° 8469 (2018)

PRÉSENTÉE LE 27 AVRIL 2018  
À LA FACULTÉ DES SCIENCES DE BASE  
GROUPE DIL  
PROGRAMME DOCTORAL EN PHYSIQUE

ÉCOLE POLYTECHNIQUE FÉDÉRALE DE LAUSANNE

POUR L'OBTENTION DU GRADE DE DOCTEUR ÈS SCIENCES

PAR

**Mauro FANCIULLI**

acceptée sur proposition du jury:

Prof. V. Savona, président du jury  
Prof. J. H. Dil, directeur de thèse  
Prof. M. Donath, rapporteur  
Prof. R. Kienberger, rapporteur  
Prof. F. Mila, rapporteur



ÉCOLE POLYTECHNIQUE  
FÉDÉRALE DE LAUSANNE

Suisse  
2018



# Acknowledgements

When writing the acknowledgements in a Ph.D. thesis, one usually starts with the official supervisors, who gave the great opportunity to work in their group, and then moves to the *actual* supervisor, who on the other hand provided precious daily support. In my case, Hugo Dil has been both of these. In fact, first of all he has given me the possibility to work on a stimulating project, having access to high level facilities and productive collaborations, and to participate in many conferences and experiments in Europe, U.S. and Japan. But most importantly, he has provided me a constant daily guidance, especially during the countless discussions over lunch we have had on scientific (and non-scientific) topics. Thank you for always being encouraging and for all the teachings.

All the experiments could not have been certainly possible without the help of other PhD students and postdocs. So thank you Stefan, Gabriel, Andrew and Eduardo for sharing your experience and company with me, it has been a pleasure to work with all of you and to spend all this (beam)time together. I also would like to thank all the present and past colleagues of the Spectroscopy of Novel Materials Group at PSI, with whom I have interacted in the past four years: Ming, Milan, Nick, Thorsten, Vladimir, Leo, Andreas, Fritz, Marco, Muntaser, Federico, Eugenio, Daniel, Alla, Yi, Christian, Jhonny, Marcus, Zhiming, Nan, Zoran, Victor, Adrian, Baiqing, Yaobo, Junzhang. They all gave me good inputs and were always a good company during my time at PSI. A particular thank to Juraj Krempaský, for involving me in his project on multiferroics and for his indestructible optimism.

For my PhD project I have met and worked also with several collaborators from other institutes. I am deeply grateful to Ulrich Heinzmann for his inspiring dedication and for sharing his invaluable knowledge. I thank very much Jan Minár and Henrieta Volfová for their calculations presented in this Thesis and for the many interesting discussions we have had in several occasions. Thanks also to Fabrizio Carbone, Enrico Giannini, Florian Speck and Thomas Seyller for providing some of the samples that I have measured. Very recently I had the great opportunity to perform experiments at the Institute of Solid State Physics of the University of Tokyo, and there I would like to thank Shik Shin, Fumio Komori, Koichiro Yaji, Ayumi Harasawa and Daiki Matsumaru for their inputs, collaboration, kindness and patience; a particular thank to Kenta Kuroda for our very long and fruitful discussions. Also thanks to László Forró and Edoardo Martino, for providing very nice samples for this project.

## Acknowledgements

---

During these four years, I also had the opportunity to collaborate on different side projects (not presented in this Thesis). For these, in particular, I would like to thank Vladimir Petrov for his teachings and his incredibly nice attitude. Among many others, I am grateful for their collaboration to Anna Isaeva, Alexander Zeugner, Paolo Sessi, Elia Razzoli, Sung-Kwan Mo, Christoph Tegenkamp, Jurek Sadowski, José Avila, Andreas Ney, Verena Ney, Dominik Kriegner.

Many ideas have been deepened and improved after fruitful discussions with people I met in different occasions, and in particular I would like to thank Lucas Plucinski, Jorg Schäfer, Ivo Souza, Ralph Claessen, Eberhard Riedle, Jürgen Henk, Karol Hricovini, Debora Pierucci and Walter Pfeiffer for their advices and inputs.

A special thanks to all the members of the jury for having kindly accepted this task, for the interesting discussions we have had in the past, and for their useful comments.

In my daily life at EPFL, I have interacted with many colleagues of the Institute, and in particular I would like to thank Marco Gioni for his availability and advices, Arnaud Magrez for giving me a glimpse on the world of crystal growing, and our secretaries Chantal, Carole and Nathalie for their kindness and helpfulness. It is also important to mention that life would have been much heavier at EPFL without the company of Gianmarco, Alberto, Silvan, Davide, Ilenia, Simon, Jens, Mathieu, Sara, Claudia, Simone, Fabio, Aparajita, Romana, and many others. In addition, the several international schools and conferences I have attended were not only meant to enrich my professional experience, but they also gave me the chance to have a lot of fun with many colleagues from all over the world, to whom I am grateful for the good times we have had together: from hiking and snowboarding in the Alps to swimming and surfing in the Atlantic.

A very special thank goes to Amerigo Solari, unforgettable professor at my high school, who unfortunately passed away way too early. He not only gave me a very solid base in mathematics and physics to tackle my future career, but also he transmitted me his great passion for these subjects, he sparked my interest in research and synchrotron facilities, and he taught me his peculiar, irruptive, resolute attitude to face the many obstacles and difficulties of working and personal life.

A great, great thank to my parents, for strongly supporting and encouraging me since I was born, understanding and without ever questioning my choices, and to my grandparents and relatives, for having accepted my quirks. I also want to mention and thank all of my friends, who did their parts to make me the person I am. They are scattered all around the world, and I want to mention all the ones I met during the different steps of my education in Lausanne, in Grenoble, in Milano, in Grosseto, and those who I know since my very early childhood in Porto Ercole.

And finally thank you Silvia, for being my solid source of serenity, for always listening to me, for being next to me even in my darkest hour, for sharing with me your life.

*Lausanne, March 2018*  
*Mauro Fanciulli*

# Résumé

Dans le processus de photoémission, un matériel excité par rayonnement ultraviolet émet des électrons. À partir de la mesure de l'énergie  $e$  et de la quantité de mouvement de ces soi-disant photoélectrons et en utilisant les lois de conservation, la spectroscopie de photoémission résolue en angle (ARPES) permet de reconstruire les propriétés électroniques d'un solide. En plus, la technique de spectroscopie de photoémission résolue en angle et en spin (SARPES) permet de mesurer aussi la polarisation de spin du faisceau des photoélectrons avec la résolution énergétique et angulaire typiques de la technique ARPES, nécessaires pour sonder les états dispersif d'un solide cristallin.

L'information de spin est strictement liée à la polarisation de spin des états électroniques mesurés, mais elle peut être modifiée par plusieurs facteurs pendant le processus de photoémission. En fait, même les électrons émis à partir d'un état initial dégénéré en spin peuvent manifester une polarisation de spin finie. Cet effet, qui à la fin est lié à des ruptures de symétrie dans l'expérience de photoémission, se produit quand il y a un phénomène d'interférence cohérent entre des différents canaux des éléments de matrice qui décrivent la transition. En particulier, en analogie avec le processus de scattering électronique, la polarisation de spin est lié à la différence de phase entre les éléments de matrice complexes associés aux canaux qui font interférence quantique.

Telle différence de phase à la base de la polarisation de spin est étroitement liée aussi à une autre quantité physique : le décalage temporel de Eisenbud-Winger-Smith (EWS). Malgré les difficultés fondamentales pour définir le concept du temps en mécanique quantique, le décalage temporel fut introduit pour décrire le processus de scattering électronique, et il peut être adapté pour étudier la chronoscopie du processus de photoémission. Grâce aux développements de la technologie laser pendant la dernière décennie, de nos jours on a à disposition des techniques de spectroscopie résolues en temps qui ont une résolution des attoseconds ( $1 \text{ as} = 10^{-18} \text{ s}$ ). Ces techniques, en mesurant le décalage temporel EWS relatif entre photoélectrons émis par des états différents, permettent de accéder au régime temporel fondamental de la photoémission sur échelle atomique.

Dans cette Thèse on présentera une voie alternative et indirecte pour sonder le processus de photoémission dans le domaine des attoseconds, en particulier sans l'utilisation des techniques laser résolues en temps, mais grâce à la mesure de la polarisation de spin. On introduira la relation mathématique entre la polarisation de spin obtenu à partir d'un état

## Résumé

---

dispersif d'un solide cristalline et le décalage temporel EWS. On discutera un model analytique où la dépendance de la polarisation de spin sur l'énergie de liaison est reliée à deux types de décalage temporel EWS : celui associé au processus de photoémission considéré comme un processus de scattering,  $\tau_{EWS}$ , et celui associé aux canaux d'interférence,  $\tau_{EWS}^s$ . On discutera aussi le sens physique de ces deux décalages temporels.

Dans cette Thèse on présentera aussi la première détermination expérimentale des décalages temporels EWS d'états dispersifs par la technique SARPES. En particulier, la technique principale utilisée dans cette Thèse est la SARPES basée sur radiation de synchrotron. Les résultats pour la bande  $sp$  bulk avec dispersion de l'électron libre d'un cristal single de Cu(111) fournissent  $\tau_{EWS}^s \approx 26$  as et  $\tau_{EWS} \approx 11$  as. En plus, les bands  $d$  aussi et les niveaux de cœur  $3p$  du cuivre montrent un certain grade de polarisation de spin. Des expériences faites sur le cuprate supraconducteur fortement corrélé  $\text{Bi}_2\text{Sr}_2\text{CaCu}_2\text{O}_{8+\delta}$  (BSCCO 2212) montrent des décalages temporels EWS qui sont au moins 3 fois que dans le Cu(111). Ce résultat suggère une possible dépendance des décalages temporels EWS sur les corrélations électroniques. Dans tous les états dispersifs on trouve une caractéristique polarisation double, possiblement liée à des corrections de self-energy du processus de photoémission. En plus, des récents mesures SARPES basée sur lumière laser sur BSCCO 2212 seront présentées.

Les résultats présentés dans cette Thèse ouvrent la rue à un type d'information qualitativement neuf qui est accessible par la technique SARPES, qui devient complémentaire à les spectroscopies avec résolution des attoseconds. Le model présenté aide à comprendre la polarisation de spin qui est obtenue par des calculs de photoémission one-step, où l'information temporelle devient donc accessible. Cette approche peut aider à comprendre la physique des différents matériaux d'intérêt, mais aussi à mieux interpréter l'information de spin obtenue expérimentalement avec la SARPES, même que à mieux décrire les bases de mécanique quantique du processus de photoémission.

**Mots clefs** : Physique des solides, photoémission, polarisation du spin, décalage temporel

# Sintesi

Nel processo di fotoemissione, un materiale eccitato con luce ultravioletta emette degli elettroni. Dalla misura dell'energia e della quantità di moto di questi cosiddetti fotoelettroni e dall'utilizzo di leggi di conservazione, la spettroscopia di fotoemissione risolta in angolo (ARPES) permette di ricostruire le proprietà elettroniche del materiale in considerazione. Inoltre, la tecnica di spettroscopia di fotoemissione risolta in angolo e in spin (SARPES) permette di misurare anche la polarizzazione di spin del fascio di fotoelettroni mantenendo la risoluzione energetica e angolare tipiche della tecnica ARPES, che sono necessarie per poter sondare gli stati dispersivi di un materiale cristallino.

L'informazione di spin è strettamente legata alla polarizzazione degli stati elettronici in esame, ma può essere modificata da diversi fattori durante il processo di fotoemissione. In effetti, perfino elettroni emessi da uno stato iniziale degenere in spin possono manifestare una polarizzazione netta. Questo effetto, che in fin dei conti è legato a rotture di simmetria nell'esperimento di fotoemissione, avviene a causa di un fenomeno di interferenza coerente tra diversi canali degli elementi di matrice che descrivono la transizione in esame. In particolare, in analogia con il processo di scattering elettronico, la polarizzazione di spin è legata alla differenza di fase tra i canali che interferiscono quantisticamente.

Tale differenza di fase alla base della polarizzazione di spin è strettamente legata anche ad un'altra quantità fisica: lo scarto temporale di Eisenbud-Wigner-Smith (EWS). Nonostante le difficoltà fondamentali che si incontrano nel definire il concetto di tempo in meccanica quantistica, lo scarto temporale EWS fu introdotto per descrivere il processo di scattering elettronico, e può essere adattato per studiare la cronoscopia del processo di fotoemissione. Grazie a notevoli sviluppi nella tecnologia laser nell'ultimo decennio, oggi si hanno a disposizione tecniche di spettroscopia risolte in tempo che raggiungono una risoluzione di attosecondi ( $1 \text{ as} = 10^{-18} \text{ s}$ ). Queste tecniche misurano lo scarto temporale EWS relativo tra fotoelettroni emessi da diversi stati e permettono di accedere al regime temporale fondamentale della fotoemissione su scala atomica.

In questa Tesi verrà presentata una via alternativa e indiretta per sondare il processo di fotoemissione nel dominio degli attosecondi, in particolare senza l'utilizzo di tecniche laser risolte in tempo, ma attraverso la misura della polarizzazione di spin. Verrà introdotta la relazione matematica tra polarizzazione di spin ottenuta da uno stato dispersivo di un solido e lo scarto temporale EWS. Verrà discusso un modello analitico dove la dipendenza della

polarizzazione di spin dall'energia di legame dell'elettrone è connessa a due tipi di scarto temporale EWS: quello associato al processo di fotoemissione considerato come un processo di scattering,  $\tau_{EWS}$ , e quello associato ai canali di interferenza,  $\tau_{EWS}^s$ . Verrà inoltre discusso il significato fisico di questi due scarti temporali.

In questa Tesi verrà anche presentata la prima determinazione sperimentale di scarti temporali EWS da stati dispersivi per mezzo della tecnica SARPES. In particolare, la tecnica principale utilizzata in questa Tesi è la SARPES basata su radiazione di sincrotrone. I risultati per la banda  $sp$  bulk a dispersione di elettrone libero di un singolo cristallo di Cu(111) forniscono  $\tau_{EWS}^s \approx 26$  as e  $\tau_{EWS} \approx 11$  as. Inoltre, anche le bande  $d$  e i livelli di core  $3p$  del rame mostrano un notevole grado di polarizzazione di spin. Esperimenti fatti sul cuprato superconduttore fortemente correlato  $\text{Bi}_2\text{Sr}_2\text{CaCu}_2\text{O}_{8+\delta}$  (BSCCO 2212) mostrano degli scarti temporali EWS che sono almeno 3 volte maggiori che nel Cu(111). Questo suggerisce una possibile dipendenza degli scarti temporali EWS dalle correlazioni elettroniche. In tutti gli stati dispersivi viene osservata una caratteristica doppia polarizzazione, possibilmente legata a correzioni di self-energy del processo di fotoemissione. Verranno presentate anche delle recenti misure su BSCCO 2212 fatte con SARPES basata su luce laser.

I risultati presentati in questa Tesi aprono la strada ad un tipo di informazione qualitativamente nuovo accessibile dalla tecnica SARPES, che diviene complementare alle spettroscopie con risoluzione negli attosecondi. Il modello presentato aiuta a comprendere la polarizzazione di spin ottenuta da calcoli di fotoemissione one-step, in cui l'informazione temporale diviene quindi accessibile. Questo approccio può aiutare a comprendere la fisica di diversi materiali di interesse, ma anche a meglio interpretare l'informazione di spin ottenuta sperimentalmente con la SARPES, così come a meglio descrivere le basi di meccanica quantistica del processo stesso di fotoemissione.

**Parole chiave:** Fisica dello stato solido, fotoemissione, polarizzazione di spin, scarto temporale



# Abstract

In the photoemission process electrons are emitted from a solid upon excitation with UV light. From the measurement of energy and momentum of these so-called photoelectrons and exploiting conservation laws, the angle-resolved photoemission spectroscopy (ARPES) technique allows to reconstruct the electronic properties of the solid. In addition, in spin- and angle-resolved photoemission spectroscopy (SARPES) the spin polarization of the photoelectron beam is measured while maintaining energy and momentum resolution of ARPES, required to probe a dispersive state of a solid.

The spin information is related to the spin polarization of the state under investigation, but can be modified for several reasons during the photoemission process. Indeed, even when the electrons originate from a spin-degenerate initial state, they can acquire a finite spin polarization. This effect, which is ultimately due to a symmetry breaking in the photoemission experiment, occurs when different channels in the matrix elements describing the transition coherently interfere. In particular, in analogy with the electron scattering process, the spin polarization is related to the phase shift between the complex matrix elements associated to the interfering channels.

The phase shift at the origin of the spin polarization is also closely related to another quantity: the Eisenbud-Wigner-Smith (EWS) time delay. Despite the fundamental difficulties to properly define the concept of time in quantum mechanics, the EWS time delay was introduced to describe the electron scattering process, and can be adapted to study the chronoscopy of the photoemission process. Thanks to advances in laser technology in the last decade, time-resolved spectroscopic techniques that reach attosecond ( $1 \text{ as} = 10^{-18} \text{ s}$ ) resolution are nowadays available. By measuring relative EWS time delays between photoelectrons from different states, they permit to access the fundamental time scale of photoemission at the atomic level.

In this Thesis, an alternative indirect way to probe the photoemission process in the attosecond domain without time-resolved laser techniques will be presented. The link between spin polarization from dispersive states of a solid and the EWS time delay will be introduced. An analytical model will be discussed, where the dependence of the spin polarization with binding energy is related to the EWS time delay of photoemission as a scattering process  $\tau_{EWS}$  and the EWS time delay between the interfering channels  $\tau_{EWS}^s$ . Hence it will be shown that by measuring the spin polarization of the photoelectrons without an explicit time resolution

## Abstract

---

in the experiment it is possible to indirectly determine the time scale of the photoemission process.

The first experimental determination of EWS time delays from dispersive states by SARPES will be also presented. Synchrotron radiation-based SARPES is the main technique used in this Thesis. Results for a single crystal of Cu(111) give  $\tau_{EWS}^s \approx 26$  as and  $\tau_{EWS} \approx 11$  as for the free-electron-like  $sp$  bulk-derived band. The spin polarization of the  $d$  bands and of the  $3p$  core levels of copper is also investigated. On the other hand, experiments on the strongly correlated cuprate superconductor  $\text{Bi}_2\text{Sr}_2\text{CaCu}_2\text{O}_{8+\delta}$  (BSCCO 2212) show EWS time delays that are at least 3 times larger than in Cu(111). A double polarization feature is observed for the dispersive states, which is likely related to self-energy corrections in the photoemission process. Recent results on BSCCO 2212 performed with laser-based SARPES will be also discussed.

The results presented in this Thesis pave the way for a qualitatively new kind of information accessible by the SARPES technique, which is complementary to attosecond-resolved spectroscopies. The model presented sheds light on the spin polarization that is obtained by one-step model photoemission calculations, where the time information becomes also available. This approach could help to advance in the understandings of the physics of materials of interests, in particular electronic correlations, but also to better interpret the spin information that is experimentally obtained in SARPES, as well as to describe the basics of the quantum mechanics of the photoemission process itself.

**Key words:** Solid state physics, photoemission, spin polarization, time delay

# Contents

<b>Acknowledgements</b>	<b>i</b>
<b>Abstracts (Français, Italiano, English)</b>	<b>iii</b>
<b>Preface</b>	<b>xi</b>
<b>1 Introduction</b>	<b>1</b>
1.1 The problem of time in quantum mechanics . . . . .	1
1.2 Attosecond-resolved photoemission spectroscopy . . . . .	5
1.3 The Eisenbud-Wigner-Smith (EWS) time delay . . . . .	7
1.4 An indirect way to time delay . . . . .	10
<b>2 Spin polarized electrons</b>	<b>13</b>
2.1 The spin quantum number . . . . .	13
2.1.1 Spin polarization . . . . .	16
2.2 The Pauli representation of spin . . . . .	17
2.2.1 The density matrix formalism . . . . .	18
2.3 Elastic relativistic electron scattering . . . . .	19
2.3.1 The Dirac equation . . . . .	19
2.3.2 Mott scattering . . . . .	20
<b>3 Photoemission spectroscopy</b>	<b>25</b>
3.1 The photoemission process . . . . .	25
3.1.1 The 3-step and the 1-step models of photoemission . . . . .	28
3.1.2 The "sudden" approximation . . . . .	31
3.1.3 Angle-resolved photoemission spectroscopy (ARPES) . . . . .	34
3.2 Spin- and angle-resolved photoemission spectroscopy (SARPES) . . . . .	35
3.2.1 3D Mott polarimeter at the COPHEE endstation . . . . .	36
3.3 Spin polarization in photoemission . . . . .	40
3.3.1 Spin-degenerate initial states: atomic photoionization . . . . .	41
3.3.2 Spin-degenerate initial states: solid state photoemission . . . . .	43
<b>4 From spin to time</b>	<b>47</b>
4.1 Phase shift as a common term . . . . .	47
4.2 Spin polarization in solids: geometrical correction . . . . .	48

## Contents

---

4.3	Estimate of time delays . . . . .	51
4.4	Influence of the radial terms on the estimate . . . . .	54
4.5	Spurious effects . . . . .	56
4.6	The case of a spin polarized initial state . . . . .	57
<b>5</b>	<b>Experimental results: the model system Cu(111)</b>	<b>61</b>
5.1	Characterization of Cu(111) crystal . . . . .	61
5.2	EWS time delays from the <i>sp</i> bulk band . . . . .	63
5.2.1	DFT calculations and the double polarization feature . . . . .	68
5.3	Spin-resolved survey of the <i>3p</i> core levels . . . . .	71
5.4	Spin polarization from the <i>d</i> bands . . . . .	73
<b>6</b>	<b>Experimental results: the strongly correlated material BSCCO</b>	<b>77</b>
6.1	Photoemission from BSCCO 2212 . . . . .	77
6.2	Spin polarization from the CuO <sub>2</sub> -derived band . . . . .	80
6.3	Estimate of EWS time delays . . . . .	81
6.4	Laser SARPES on BSCCO 2212 . . . . .	83
<b>7</b>	<b>Discussion on EWS time delays in photoemission and concluding remarks</b>	<b>89</b>
<b>A</b>	<b>Explicit formulas for the estimate of time delays</b>	<b>95</b>
A.1	Atomic photoionization . . . . .	95
A.2	Solid state photoemission . . . . .	96
<b>B</b>	<b>Further studies: quasi-free-standing graphene monolayer</b>	<b>97</b>
	<b>Bibliography</b>	<b>99</b>
	<b>Curriculum Vitæ</b>	<b>109</b>

# Preface

Angle-resolved photoemission spectroscopy (ARPES) is a well-established technique which allows to probe energy and momentum of electrons emitted from condensed matter upon UV or X-ray excitation (photoelectrons), and thus to reconstruct the electronic band structure of a solid. Spin-resolved ARPES, in addition, measures the spin polarization of the photoelectron beam, which can be polarized if the initial electronic state is polarized (as in ferromagnets, Rashba-like materials or topological insulators, for example), but also if quantum interference occurs during the photoemission process, as it is known since many decades. However, given the large interest in the physics of the materials of the first case, the second case has been in general less investigated, and only on localized states or without angular resolution.

The aim of this Thesis is to deepen the understanding of the spin polarization in photoemission from spin-degenerate states, in particular in the case of dispersive states, and to extract information about the interference process at its origin. The key quantity is the phase term of complex matrix elements describing the transition. This phase term is also closely related to the so-called Eisenbud-Wigner-Smith (EWS) time delay of photoemission, which is used to describe the chronoscopy of the process and can be probed by attosecond-resolved photoemission experiments. Therefore, in principle, it is possible to give an indirect estimate of the EWS time delay by measuring the spin polarization from spin-degenerate states. This estimate is the main topic of this Thesis.

The organization of the Thesis is the following:

- In **Chapter 1** the issue of describing time in quantum mechanics is briefly presented, discussing how state of the art techniques allow measurements in the attosecond (as) time domain, and showing the starting idea of indirectly accessing time delays in photoemission by the measurement of spin polarization.
- In **Chapter 2** the concept of spin is introduced and the effects on the spin polarization of an electron beam upon elastic scattering are reviewed. This phenomenon is at the basis of both the photoemission spin detector described in Chapter 3, and of the interference process in photoemission discussed in Chapter 3 and Chapter 4.

- In **Chapter 3** the basics of the photoemission process are introduced, with focus on the origin and the measurement of the spin polarization; the experimental setup of the COPHEE endstation at the Swiss Light Source is also described.
- In **Chapter 4** a semi-quantitative model that allows to estimate the EWS time delay in photoemission from a spin-degenerate state by measuring the spin polarization of the photoelectrons as a function of binding energy is presented. The case of spin-polarized states is also briefly discussed. In particular, the two quantities  $\tau_{EWS}$  and  $\tau_{EWS}^s$  are discussed and their link to the spin polarization is shown.
- In **Chapter 5** spin-resolved photoemission experiments on a crystal of copper are shown and discussed. Time delays of  $|\tau_{EWS}^s| \approx 26$  as and  $|\tau_{EWS}| \approx 11$  as are found.
- In **Chapter 6** similar results are presented for the cuprate superconductor  $\text{Bi}_2\text{Sr}_2\text{CaCu}_2\text{O}_{8+\delta}$ . The found EWS time delays are at least three times larger than in Cu(111). Recent experiments performed with laser-SARPES will be also shown.
- In **Chapter 7** the main findings of the Thesis are summarized, with a focus on the interpretation of time delays in photoemission, and with an outlook of future possible applications of the method presented in this Thesis.
- In **Appendix A** some explicit expressions of formulas introduced in Chapter 4 are given, whereas in **Appendix B** further studies of spin polarization from spin-degenerate states are briefly presented for a quasi-free-standing monolayer of graphene.

This Thesis has been submitted to the Doctoral School of Physics of the Basic Sciences Faculty at the École Polytechnique Fédérale de Lausanne (EPFL, CH-1015 Lausanne, Switzerland), in order to fulfill the requirements for obtaining a *Scientiæ Doctor* (Sc.D.) degree in Physics, equivalent to a *Philosophiæ Doctor* (Ph.D.) degree in Physics. The work has been carried out under the supervision of Prof. Hugo Dil at the Institute of Physics of EPFL, and most of the experiments were performed at the Surface and Interface Spectroscopy (SIS) beamline at the Swiss Light Source (SLS) of the Paul Scherrer Institut (PSI, CH-5232 Villigen, Switzerland). The laser SARPES experiment presented in Chapter 6 has been performed at the Laser and Synchrotron Research Center (LASOR) at the Institute for Solid State Physics of the University of Tokyo (ISSP, Kashiwa, Chiba JP-277-8581, Japan).

# 1 Introduction

*“Quid est ergo tempus? Si nemo ex me quaerat, scio; si quaerenti explicare velim, nescio.”*  
*“What then is time? If no one asks me, I know; if I wish to explain it to someone asking it,*  
*I do not know.”*

- Saint Augustine, *Confessions*, 11.14.17 (ca. 400)

In this Chapter the issue of dealing with time in quantum mechanics is briefly reviewed. Different attosecond resolved spectroscopy techniques are described, and the important concept to this Thesis of the Eisenbud-Wigner-Smith time delay is explained. The idea of indirectly evaluating time delays in photoemission by the measurement of spin polarization, the main result developed in the following Chapters, is introduced.

## 1.1 The problem of time in quantum mechanics

The nature of time has certainly been a central question since the very beginning of philosophy in the antiquity <sup>1</sup>. With the advent of modern science, when the description of the natural world started to be carried out with mathematical laws, Galilei's relativity and Newton's mechanics required time to be a background parameter, a universal and absolute coordinate to which a system could be referred to. This concept, which accurately matches the daily experience of time flowing, lasted for almost 300 years, until the scientific revolution initiated by Albert Einstein. However, even within the special relativity frame where time is modified depending on the velocity of the observer, it can still be considered as a global, external parameter once Lorentz transformations are carefully taken into account. It is only with general relativity that time - together with space - becomes a quantity that is influenced by the presence itself of matter, and thus cannot be considered as a global parameter.

---

<sup>1</sup> Among many renowned examples, it is worth to mention at least the following ones. Anaximander, one of the first known philosophers, already understood the importance of describing phenomena as a function of time [1]. Zeno of Elea pointed out the impossible consequences of dividing time into infinitesimal durations in the arrow's paradox [2]. Plato introduced the idea of time as an abstract frame to which movements are referred to [3]. For Aristotle, on the contrary, time has a logical meaning only in relation to movement [2], so that it could be defined as the measure of "kinetic length" [4].

## Chapter 1. Introduction

---

In the realm of quantum mechanics, on the other hand, time remains a global classical parameter, used to describe the dynamical equations by which all the physical observables vary. Such classical treatment of time in quantum mechanics is at the basis of the irreconcilability of this theory with general relativity, one of the biggest open questions of our times. A second connected big question concerns the direction of time. In daily experience, time is perceived as unavoidably flowing in only one direction, because of thermodynamical irreversibilities, but on a mathematical level quantum mechanics equations, as well as classical ones, can work correctly in both ways <sup>2</sup>.

Besides these problems connecting quantum mechanics to other realms, another main issue is raised within quantum mechanics itself. All the physical observables (energy, momentum, angular momentum...) are associated to self-adjoint operators on a Hilbert space. This naturally occurs also for the position of a particle:  $x \rightarrow \hat{x}$ . Time, on the other hand, cannot be promoted to an operator, but has to merely remain a scalar parameter. This argument has been made by Wolfgang Pauli [6] and has become the starting point of every discussion about time in quantum mechanics. He argued that since the Hamiltonian operator is often discrete and bound, it is formally not possible to construct a self-adjoint operator  $\hat{t}$  that would satisfy the canonical conjugate commutation relationship  $[\hat{H}, \hat{t}] = -i\hbar$ . This implies that time is not a physical observable [7]. Another curious difference between space and time can be seen in a very basic concept of quantum mechanics. An existing quantum particle is guaranteed to be found, at any time, *somewhere* in space by wavefunction normalization requirement (i.e.,  $\iiint_{-\infty}^{+\infty} |\psi|^2 d\mathbf{r} = 1$ ). However, there is no equivalent guarantee that such particle will be found, at a given position, *at some point in time*, even in an ideal eternal wait [8].

A consequence of these arguments involves the Heisenberg uncertainty principle. In fact, the well-known energy-time relationship

$$\Delta E \Delta t \geq \frac{\hbar}{2}, \quad (1.1)$$

even if it is commonly referred to as an Heisenberg uncertainty relationship, is only a general property of Fourier transformation, and is not well defined in quantum mechanics because of the absence of a time observable. A better formulation of the energy-time relationship is the following [9]:

$$\sigma_{\hat{H}} \sigma_{\hat{Q}} \geq \frac{\hbar}{2} \left| \frac{d\langle \hat{Q} \rangle}{dt} \right|, \quad (1.2)$$

where  $\sigma$  represents the standard deviation,  $\hat{H}$  is the Hamiltonian operator of the system and  $\hat{Q}$  is any observable not explicitly dependent on time ( $\frac{\partial \hat{Q}}{\partial t} = 0$ ). Defining  $\Delta E = \sigma_{\hat{H}}$  and  $\Delta t = \frac{\sigma_{\hat{Q}}}{|d\langle \hat{Q} \rangle / dt|}$  (here the definition of  $\Delta t$  already requires the classical variable of time), one then obtains Eq. (1.1). This relationship is often referred to as *Mandelstam-Tamm inequality* [9, 10].

---

<sup>2</sup> For a simple introduction to contemporary attempts to solve these issues and a nice discussion on the history and philosophy of time, see Ref. [5].



## 1.1. The problem of time in quantum mechanics

---

From Eq. (1.2) it follows that for a given uncertainty  $\sigma_{\hat{H}}$  the uncertainty of *any* observable  $\sigma_{\hat{Q}}$  is related to the *change in time* of the expectation value of the observable itself. In other words, the rate of change of any observable must be slow enough in order to have a good resolution in the measurement of energy, which does not set any restriction at all to the actual value of a measured time itself, once a measurement of time will be properly defined.

At this point, it is worth to mention that the differences between space and time in quantum mechanics are more subtle, as nicely explained by Jan Hilgevoord [11]. Indeed, to be precise, also *space* itself (in the sense of absolute coordinates, without considering the issue of general relativity) is not an observable, whereas only *position* with respect to the frame is. One should therefore rather consider the measurement of the *duration* of a time interval starting at some time reference ("time-zero"), in the same way as position being the length of a distance from some reference. Thus, the time equivalent of the position operator  $\hat{x}$ , usually called *arrival time*, is not a self-adjoint operator, but it can be shown to be at least a symmetric operator [12]. Also, it is possible to define several operators associated to time durations, usually called *sojourn times* and *time delays*, which are on the other hand associated to physical observables. This simple distinction highlights the important issue of defining time-zero for a time measurement, which is a recurrent and crucial difficulty in experiments. Also, it looks like that such simple naming nuance has solved the problem, but in practice different physical situations require different definitions which are not always easy to make compatible to each other [12, 13].

Without further discussing this extremely complex topic, the point here is that in standard treatments of quantum experiments, one usually takes into account the time duration only when looking at "macroscopic" classical time scales, in the sense of dynamical behaviour of complex collective phenomena. The flow of time can then be seen as in daily experience. On the other hand, when considering very basic quantum processes, time is not explicitly taken into account, and changes of states of a system are considered to be instantaneous. The term "macroscopic" should not be misleading: down to the picosecond ( $10^{-12}$  s) or even femtosecond ( $10^{-15}$  s) regime, processes such as tunneling, radiation-matter interaction, or the wavefunction collapse itself, can be safely considered to be instantaneous. This pragmatic solution has been the workaround of the issue for many decades, since it was anyway impossible to try to measure such extremely short time durations. Given that the timing of quantum phenomena on a theoretical level is primarily restricted to single events, the debate about the instantaneity of "quantum jumps", as named by Niels Bohr, has been relegated for decades to academic thought experiments [13]. For instance, Erwin Schrödinger, despite being against the idea of instantaneous quantum jumps, said in this regard: "*We never experiment with just one electron or atom or small molecule. In thought experiments we sometimes assume that we do, this invariably entails ridiculous consequences (...). In the first place it is fair to state that we are not experimenting with single particles any more that we can raise Ichthyosauria in the zoo*" [14]. Nowadays though, even if we do not breed dinosaurs yet [15], we do make experiments on individual systems. Also, we even manage to reach extremely small time resolution

## Chapter 1. Introduction

---

in ensemble experiments. Therefore two main points can be raised against instantaneous processes.

First, they are still not satisfactory. Even without considering the impossibility to define instantaneousness because of general relativity, it is difficult to accept that, for example, at the instant a photon gives its energy to an electron, at that very same instant the electron has already acquired that energy. This is what an instantaneous transition would imply, which goes against conservation of energy, and thus there must be some time delay between the two situations. But what happens in between? A continuous change sounds tricky, since it is not clear what would happen to quantized entities such as energy. Thus one could consider theories where the flow of time itself is quantized, so that a small but finite lapse is introduced. The lowest possible limit for such "quantum of time" would be the famous Planck time:  $t_P \approx 5.4 \times 10^{-44}$  s ( $t_P$  is related via the speed of light to the Planck length  $\ell_P$ , which is the Compton length of a particle of mass  $m$  when it is of the same order as the Schwarzschild radius of an object with mass  $m$ , and it is defined by universal constants). Other more advanced models introduce the quantum "chronon" as the time where light travels along the classical radius of an electron, or modifications of this idea [16, 17], which gives something of the order of  $\approx 10^{-23}$  s. Such time scales are nowadays impossible to probe, and are anyway still much shorter than what one would actually simply estimate for quantum basic atomic processes, which should occur in the **attosecond** ( $10^{-18}$  s) domain. Very naively, in 1 as light travels for about  $3 \text{ \AA}$ , which is of the order of an atomic size. Also, it is instructing to see how the unit of time in atomic units is  $t_{a.u.} = \frac{\hbar}{\alpha^2 m_e c^2} \approx 24$  as, which corresponds to the time it takes to an electron to perform one orbit of Hydrogen atom in the Bohr model.

Second, and far more important: "*Eppur si move!*"<sup>3</sup>, i.e., in this context, despite all the theoretical considerations *we do measure time delays as extremely short as a few attoseconds*. In the past fifteen years, advances in laser technology have opened up the possibility to investigate electronic dynamics in matter, in a new field called *attosecond physics* [18–22]. The processes that are tackled involve radiation-matter interaction, and can be divided mainly into two families: radiation-driven tunneling ionization, and photon absorption. In the first case, the interaction with the light electric field bends the atomic potential so that electronic bound states are allowed to tunnel outside the atom, and in some cases to eventually recollide back because of a resonant process with the oscillating electric field [23]. This allows to study the equivalent travel time of an electron during the tunneling process, a fundamental question in the history of quantum physics [24]. It involves the introduction of time as a complex quantity and there is not yet a fully accepted answer [25–30]. In the second case, the photon of the light provides enough energy to an electron to escape from the bound state, a process that is usually called *photoionization* in the case of atomic systems, and *photoemission* in the case of condensed matter targets. In this Thesis mainly the photoemission process will be considered, but a link to photoionization will be often made. Whereas the photoemission process will

---

<sup>3</sup> "Still, it moves!", famous quote by Galileo Galilei about Earth after his forced abjuration of heliocentrism to the Inquisition. It has actually be invented by Giuseppe Baretta in a reconstruction of the episode in his anthology *Italian Library*, 1757.

## 1.2. Attosecond-resolved photoemission spectroscopy

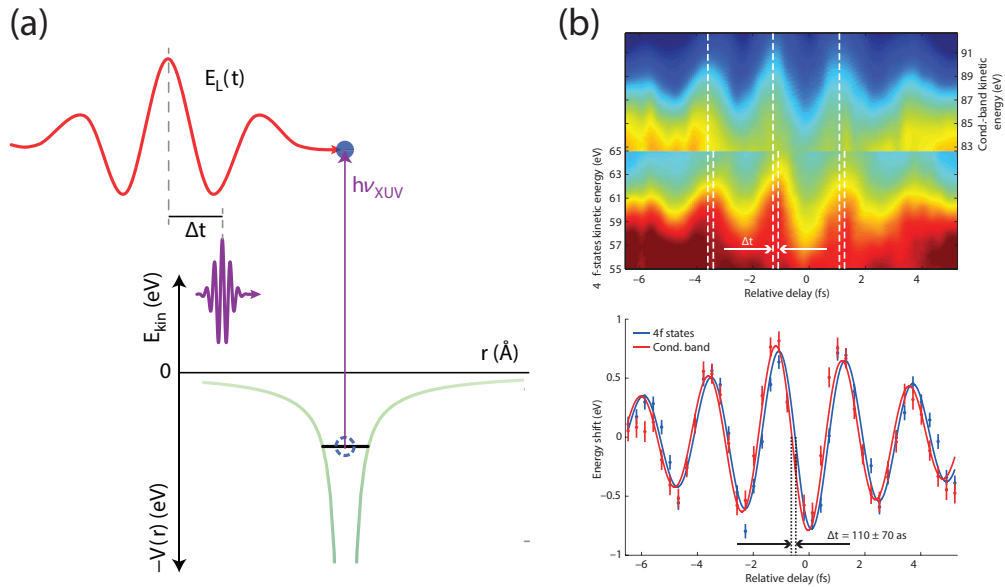


Figure 1.1: (a) Scheme of the streaking experiment (modified from Ref. [38]). (b) An example of a streaking spectrum on W(110) (from Ref. [36]).

be described in more details in Chapter 3, in the next Section only the salient features of attosecond-resolved photoemission techniques will be shortly presented.

## 1.2 Attosecond-resolved photoemission spectroscopy

All the current attosecond-resolved techniques are based on a pump-probe setup that relies on a  $\approx 100$  as ultraviolet (UV) laser pump and a phase-controlled few-cycle femtosecond infrared (IR) laser probe, which are temporally closely correlated because of the high harmonic generation process they rely on [31–33]. There exist two main different techniques [34]:

- **Streaking.** In attosecond streaking [31, 33, 35–37], a single UV pump pulse photoemits the electrons, that are then accelerated or decelerated by the electric field of the low intensity IR pulse as a function of pump-probe controlled delay. The intensity of the IR pulse is high enough to "streak" the energy of the electron wavepacket in the continuum, but has to be low enough not to affect the bound electrons. In Fig. 1.1(a) the scheme of a streaking experiment is shown, while in Fig. 1.1(b) a typical energy streaked spectrum is displayed. The spectrum is from Ref. [36], which reports attosecond streaking on W(110).

- **RABBITT.** The "reconstruction of attosecond beating by interference of two-photon transitions" (RABBITT) [32, 39–41] is based on a train of UV pulses and an intense ( $3 \times 10^{11}$  W/cm<sup>2</sup>) IR pulse. They induce a two-photon transition that shifts the energy of the electron excited by the UV laser at energies in between two neighbouring harmonics, the so-called side bands. The intensity of these side bands will oscillate with the pump-probe controlled delay because of quantum path interference according to perturbation theory. In Fig. 1.2(a) the scheme of

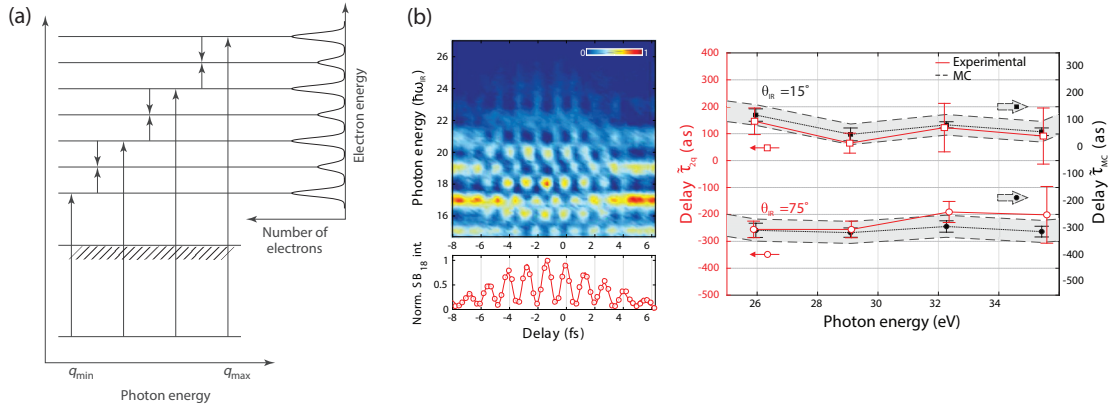


Figure 1.2: (a) Scheme of the RABBITT experiment (from Ref. [43]). (b) RABBITT spectrum for the 3d valence band of Cu(111) and measured relative time delays for two geometries with respect to a atomic Ne gas reference. From Ref. [42].

the RABBITT experiment is shown, while in Fig. 1.2(b) an example of measurement is reported from Ref. [42]. In this experiment, the time delay of the 3d valence band of Cu(111) between different experimental geometries has been investigated.

Several variation of these techniques are possible, with different proposed algorithms for the data analysis. In particular, it is crucial to be able to disentangle the time information of the probed material from additional time delays introduced by the specific measurements, which are of different kind, and not always easy to identify. It is also worth to mention an interesting variant of the (linear) streaking technique, namely the *angular streaking*, also called *attoclock*: in this case the IR polarization is circular instead of linear, and the electrons are thus streaked in a direction in space that depends on the direction of the rotating electric IR field, which therefore acts as the hand of a clock [25, 26, 44, 45].

Many different systems have been studied in the past few years, ranging from atomic targets to solid state materials. Typical values of time delays that are obtained are of the order of decades to hundreds of attoseconds. For example, about  $\approx 10$  as have been measured for the time delay between the  $\text{He}^+ 2s^1/2p^1$  shake-up transition and the direct  $\text{He } 1s^2$  photoionization transition [38]. A time delay of  $\approx 100$  as has been found between the 4f core levels and the conduction band of W(110) [36]. Recently, experiments on  $\text{WSe}_2$  have shown delays of  $\approx 50$  as for the W 4f core level compared to the Se 4s core level [46]. In Cu(111), the time delay from the d bands under two different experimental geometries has been measured to be  $\approx 330$  as [42]. Notably, in this case there is a mismatch of about 50 as with simulations, which has been ascribed to the fact that the absolute time delay of the photoemission process has not been taken into account [42]. It is possible to compare this value with the results presented in Chapter 5, even though there the sp band of Cu(111) has been considered.

Here, for the purposes of this Thesis it is only important to underline the following: because of their pump-probe nature, all the attosecond-resolved spectroscopy experiments can only

probe a *relative* time delay between some electronic state under consideration and some other *reference*. Such reference could be a different electronic state of the system [36], or a different system [47], or the same state under a different experimental condition [42], but no information can be directly extracted about the *absolute* time information, because of the nature of a pump-probe experiment. Only recently, a way to access absolute time delays has been proposed, which however has to rely on theoretical result as an input [38, 48]. The word "absolute" should not generate confusion: a time delay  $\tau$  describes a time duration, as explained in Section 1.1, and therefore still depends on time-zero. In particular, time-zero will be the instant when the considered process begins, and is not necessarily easy to define in the experiment [37]. Still, the point is that attosecond-resolved experiments can directly measure only time delay *differences*  $\Delta\tau$  between different processes.

At this point it is necessary to define an expression for the time delays that are probed in the photoemission process, which will be done in the following Section in analogy with the process of particle scattering.

### 1.3 The Eisenbud-Wigner-Smith (EWS) time delay

In the context of elastic scattering of particles, the concept of time delay as an observable was first heuristically introduced by Leonard Eisenbud in 1948 in his (unpublished) PhD thesis [49] under the supervision of Eugene Wigner. Such time delay is interpreted as the "sticking time" of an incoming particle, because of the formation of a transient quasibound state before the particle leaves the interaction region of the scatterer. As shown by Wigner, in the simple case of single channel scattering, one can construct a time delay operator by considering the incoming and outgoing wave packets and their relative phase shift  $\phi$  [50], and obtain

$$\hat{t} \mapsto 2\hbar \frac{d}{dE} \phi(E). \quad (1.3)$$

As shown in Fig. 1.3(a) from Ref. [19], the phase shift  $\phi$  between a free electron wave function (gray) and the one of a Wentzel–Kramers–Brillouin (WKB) solution to the attractive potential  $V_0$  (black) varies with the kinetic energy of the particle. The time delay can then be evaluated with Eq. (1.3).

The expression above was extended by Felix Smith in order to consider multichannel scattering. For an incoming wavefunction  $\psi_{in}$  and an outgoing wavefunction  $\psi_{out}$ , the scattering matrix  $\mathcal{S}$  is such that  $\psi_{out} = \mathcal{S}\psi_{in}$ . The time delay operator [51] is given by

$$\hat{t} \mapsto -i\mathcal{S}^\dagger(E) \frac{d}{dE} \mathcal{S}(E), \quad (1.4)$$

where the dagger symbol indicates the conjugate transpose of the matrix. Eq. (1.3) can be reobtained by considering that, in spherical symmetry, the single channel scattering matrix is diagonal in the angular momentum  $\ell$  representation, with  $\mathcal{S}_\ell(E) = e^{2i\phi_\ell(E)}$  [22]. The

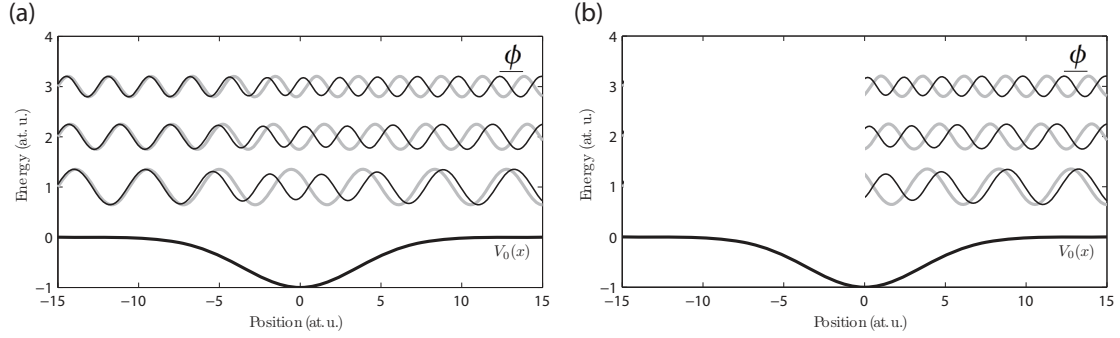


Figure 1.3: (a) EWS model in scattering. (b) EWS model in photoionization. Figures modified from Ref. [19].

expressions in Eqs. (1.3) and (1.4) and related ones historically go under the name of *Eisenbud-Wigner-Smith (EWS) time delay*  $t_{EWS}$ , or *Wigner time delay* for short.

Another way of interpreting the EWS time delay without making use of the  $\mathcal{S}$  matrix is to consider the group velocity  $v_g$  of the crest of the outgoing wavepacket as the classical motion of a particle. Eventually indeed, such particle will asymptotically follow the free particle motion, with a trajectory described by  $r = v_g(t - t_{EWS})$ . Therefore the EWS time delay ideally corresponds to the time difference between the actual scattered particle with respect to a very same particle that would pass by the scatterer region without feeling the interaction potential.

As pointed out in Ref. [52], there is a small discrepancy in the notations used by Eisenbud and Smith respectively, which has often been overlooked in literature. In Eisenbud's work [49], he considered also the case of scattering into multiple final states, and Smith pointed out the equivalence of this with his multichannel scattering description [51]. However, the two results are equivalent only when considering an absolute value: in the simple case of a single-resonance two-channel problem one finds the same and positive time delay for the two channels in the sense of Eisenbud, but same and opposite sign time delays according to Smith. This issue will be again considered in Chapter 7.

The concept of EWS time delay in particle scattering can be extended to describe the photoionization and photoemission processes, which is more suitable for the purposes of this Thesis. The main idea is that the photoemission process can be considered as a "**half-scattering**" **process**, in the sense that there only is the outgoing electron as a scattered wave in the continuum after absorption of a photon, whereas there is no incoming wave packet, as illustrated in Fig. 1.3(b). The physical meaning of time delay in photoemission will be examined in Chapter 7. The fact that the initial state of the particle is a bound state instead of a scattering state is reflected in the expression for the EWS time delay that is obtained from Eq. (1.4) by writing the  $\mathcal{S}$  matrix from perturbation theory applied to the photoemission process of a one-electron system [22]. This leads to the expectation value of the EWS time delay, that is

$$\tau_{EWS} = \hbar \frac{d\phi}{dE} = \hbar \frac{d\Delta}{dE} \{ \langle \psi_f | \hat{H}_{int} | \psi_i \rangle \}, \quad (1.5)$$



### 1.3. The Eisenbud-Wigner-Smith (EWS) time delay

where a factor of 2 is missing with respect to Eq. (1.3). The letter  $\tau$  has been used instead of  $t$  to distinguish the half-scattering from the scattering process. In this case, the phase term  $\phi$  is the phase (i.e. the argument) of the complex matrix element  $M_{fi} = Re^{i\phi}$  describing the transition:  $\phi = \angle \{M_{fi}\} = \angle \{ \langle \psi_f | \hat{H}_{int} | \psi_i \rangle \}$ . The quantity  $M_{fi}$  will be described in Chapter 3. When considering a many-electron system, Eq. (1.5) is generalized to the following:

$$\tau_{EWS} \approx \frac{\sum_q \hbar \frac{d\angle \{M_{fi}^q\}}{dE} |M_{fi}^q|^2}{\sum_q |M_{fi}^q|^2}, \quad (1.6)$$

where the sums are carried out for all the quantum numbers  $q$  of the remaining electrons system in the final state<sup>4</sup>. The approximation consists in neglecting the energy derivative of the radial part  $R$  of the matrix elements [22] (similarly to what it will be done in Section 4.3).

An important difference between the presented formulas for scattering and half-scattering is that, in the initial work of Eisenbud, Wigner and Smith, Eqs. (1.3) and (1.4) were strictly well defined only for a short-range (i.e. Yukawa-like) potential. On the other hand, the half-scattered electron in photoemission will feel a long-range Coulomb-like potential, because of the interaction with the positive charge left in the system. Therefore, it is required to extend the discussion to long-range potentials, which has been done already for the problem of particle scattering [53, 54]. In order to do so, one needs to introduce the Coulomb potential in the scattering matrix  $\mathcal{S}$  and to explicitly express the centrifugal potential<sup>5</sup>  $V_{\text{centr.}} \propto \frac{\ell(\ell+1)}{r^2}$ . This particular dependence on  $\ell$  has been recently observed in WSe<sub>2</sub> [46]. The concept of EWS time delay is thus extended to the so-called *Coulomb time delay*  $t_{EWS} \rightarrow t_C$  [22], where one finds

$$t_C = t_{EWS+C} + \Delta t_{\text{ln}}. \quad (1.7)$$

The term  $t_{EWS+C}$  is the actual time delay due to a phase shift because of the scattering process, in strong analogy with the EWS time delay itself, which does not depend on the position  $\mathbf{r}$  of the electron. The additional term  $\Delta t_{\text{ln}}$  is a logarithmic correction that takes into account an additional phase shift  $\propto \ln(2\mathbf{k}\mathbf{r})$ , which describes the Coulomb "drag" from the positive charge left behind felt by the electron with wavevector  $\mathbf{k}$ . In terms of classical trajectory description, since the particle will feel the Coulomb interaction even at large distances, the term  $\Delta t_{\text{ln}}$  is equivalent to the time delay occurring in a hyperbolic Kepler trajectory of an object with fixed angular momentum [22].

<sup>4</sup> This expression is necessary when more than two channels are available in the interference process described in Chapter 4. In this Thesis, however, only two interfering channels will be considered for simplicity. See also the footnote 1 in Section 4.1.

<sup>5</sup> In order to solve the 3D Schrödinger equation, the solution is separated into radial part  $R$  and angular part  $Y$ . The part  $Y$  is found to be given by the spherical harmonics, while for  $R$  one can define a new function  $u = rR$  so that the radial equation becomes the 1D Schrödinger equation. In this case the potential is rewritten as  $V \rightarrow V + \frac{\hbar^2}{2m} \frac{\ell(\ell+1)}{r^2}$ . The additional term is called "centrifugal term" since it corresponds to a classical case that gives rise to a repulsive centrifugal pseudo-force [55].

The description of time delays in long-range potentials stays the same when moving to the photoemission process. In this case, a measurement of a relative time delay between different  $\tau_C$  coincides with the measurement of  $\Delta\tau_{EWS+C}$ . One should therefore speak of the Coulomb EWS-like time delay, but literature often refers to it as simply EWS time delay. Also, a possible measurement of an absolute time delay implies that the measured time duration is not anymore referred to the actual time zero, but to the time zero corrected by the term  $\Delta\tau_{ln}$ . This last term will be considered again in Section 3.1.2 and in Chapter 7. The main focus of the Thesis, however, will be on the term  $\tau_{EWS+C}$  (simply called  $\tau_{EWS}$  following the literature), as it will be shown in Chapter 4. Another related quantity,  $\tau_{EWS}^s$ , will be also introduced. A discussion of the physical meaning of these time delays can be found in Chapter 7.

### 1.4 An indirect way to time delay

A conventional photoemission spectroscopy technique measures the energy of the emitted electrons from a material after the interaction with electromagnetic radiation. An energy-resolved measurement exploits the Fermi golden rule (see Section 3.1.1), where the photoemission intensity depends on the modulus square of the matrix elements  $M_{fi}$ , thus losing information about the phase term. From this, it looks like that the only way to access phase shifts and therefore time delays is to use pump and probe setups, where one does not look at the eigenstates of a system but at all its possible time-dependent responses. However, if other quantum numbers will depend on the phase of the matrix elements, by measuring the corresponding physical observables it will still be possible to access the phase information without direct time-resolved experiments, and indeed this is the case.

An example is the *momentum* of the photoelectrons: it can be shown [56] that the differential photoemission cross-section, i.e. the angular distribution of the electrons, does actually depend on the phase term, too. Therefore one can, in principle, extract the phase information by measuring the angular distribution of the emitted electrons. This is a difficult experiment, but can be performed for atomic and molecular levels [57–59]. UV photoelectron diffraction (UPD) experiments show that it is possible to retrieve the phase information by circular dichroism in orbitals from non-chiral molecule [60,61]. However it is intrinsically very difficult for dispersive states of a solid, since in this case the angular distribution unavoidably also depends on the energy-momentum dispersion relationship.

Another quantum number that carries the phase information is the *spin* of the photoelectrons. Indeed, also the spin polarization of the beam of electrons emitted at a certain angle is a function of the phase of the matrix elements [56,62]. Therefore it is in principle possible to retrieve the phase information from the spin polarization from non-spin-polarized states. The dependence of the spin polarization as well as of the differential cross-section on the phase can be found by using once again a half-scattering formalism, as it will be presented in Section 3.3. Thus, in order to understand the origin of this spin polarization in photoemission, one needs first to study the role of spin in particle scattering, a topic that will be briefly



reviewed in Chapter 2. The determination of the phase information from the measurement of spin polarization has been extensively performed in atomic photoionization [63, 64]. To some extent also the case of photoemission from solids has been considered [65, 66], but the lack of energy and momentum resolution has been a limitation in the past. With the development of setups with better resolution the focus has been put mainly on the study of materials where the spin polarization is a physical property of the initial state.

The possibility to extract information on time delays from the determination of phases has been proposed only recently in the literature [67]. The **estimate of EWS time delays in photoemission without a direct time-resolution in the experiment from the measurement of the spin polarization of electrons emitted from spin-degenerate dispersive states of a solid** is the main result of this Thesis. A semi-quantitative relationship between spin polarization and time delay will be presented in Chapter 4, whereas experimental results on different materials will be reported in the later Chapters.



## 2 Spin polarized electrons

*“Please add a few words of explanation to your puzzle, such as what’s really going on.”*  
- James Frank, about the Stern-Gerlach experiment

The main results of this Thesis are based on spin-resolved photoemission spectroscopy. However, it is useful to first discuss the role of spin polarization in the physical phenomenon of *electron scattering*, since it plays a dual crucial role throughout the whole Thesis: it is at the basis of the spin detector used in the experiments, as described in Section 3.2.1, and at the same time it is at the origin of the interference effect described in Section 3.3 and Chapter 4. Therefore, in this Chapter the basics of elastic relativistic electron scattering are summarized by using the density matrix formalism and the Dirac equation. Most of the results will not be derived in detail, but simply presented in the lights of their usefulness for later Chapters. The main reference for this Chapter is the textbook *Polarized Electrons, 2<sup>nd</sup> edition*, by Joachim Kessler [62].

### 2.1 The spin quantum number

In their famous experiment in 1922 [68], Otto Stern and Walther Gerlach proved for the first time the phenomenon called *space quantization* [55]. A beam of silver atoms was sent through a region with non-uniform magnetic field along  $z$ , a direction perpendicular to the trajectory. Since the atoms were neutral, the only force experienced was the force acting on a magnetic dipole  $\mu$ :  $F_z = \frac{\partial B_z}{\partial z} \mu_z$ . In classical physics, the  $z$  component of  $\mu$  can have any value from  $-\mu$  to  $+\mu$ , since the orbital angular momentum  $\mathbf{L}$  of a classical atom can have any orientation in space relative to a given axis. The classical prediction was therefore a continuous band of silver atoms collected on a detector plate spread along the  $z$  direction. On the other hand, the quantum mechanics prediction by using the Bohr atomic model was that the  $z$  component of the orbital magnetic dipole  $\mu_\ell$  must assume only discrete values, since the associated  $z$  component of the orbital angular momentum  $\mathbf{L}$  is quantized:  $L_z = m_\ell \hbar$ . In particular, the prediction is  $\mu_{\ell_z} = -g_\ell \mu_b m_\ell$ , where the g-factor is  $g_\ell = 1$ ,  $\mu_b$  is the Bohr magneton, and  $m_\ell$  is the magnetic quantum number associated to the orbital quantum number  $\ell$ :  $m_\ell = -\ell, -\ell + 1, \dots, 0, \dots, \ell - 1, \ell$ .

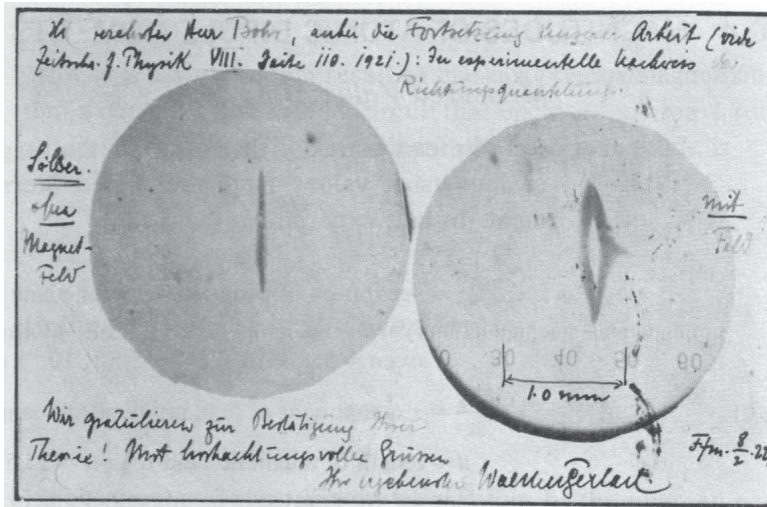


Figure 2.1: Famous postcard by Walther Gerlach to Niels Bohr (8<sup>th</sup> February 1922): "Attached is the experimental proof of directional quantization. We congratulate you on the confirmation of your theory". Left and right images show the collected silver atoms without and with applied magnetic field in their path to the detector, respectively. Image from Ref. [69].

The result of the experiment was the splitting of the silver atoms into two regions, up and down along  $z$  (horizontal direction in Fig. 2.1), which qualitatively proves the quantization of the spatial orientation of the angular momentum, but does not quantitatively agree with the prediction, since the value  $m_\ell = 0$ , which is always allowed, was not observed. In 1925, in order to explain the fine structure of optical spectra in alkali atoms George Eugene Uhlenbeck and Samuel Abraham Goudsmit proposed the existence of an intrinsic magnetic dipole moment in the electron, which has the  $z$  component described by a new quantum number  $m_s = -1/2, +1/2$  [70]. A similar experiment to the Stern-Gerlach was performed by T. E. Phipps and J. B. Taylor in 1927 with a beam of hydrogen atoms [71]. It unambiguously showed that the measured magnetic dipole moment was related to the electrons in the atoms, since at the used temperature  $\ell = 0$  and the measured  $\mu$  was of the order of  $\mu_B$ , which is defined for an electron mass.

The combination of these results lead to postulate an inherent angular momentum  $\mathbf{S}$  for the electron, defined as *spin*. In analogy to the orbital angular momentum  $\mathbf{L}$ , the following relationships hold for the spin:

$$S = \sqrt{s(s+1)}\hbar \quad , \quad \text{with } s = 1/2, \quad (2.1)$$

$$S_z = m_s\hbar \quad , \quad \text{with } m_s = -1/2, +1/2, \quad (2.2)$$

$$\boldsymbol{\mu}_s = -\frac{g_s\mu_B}{\hbar}\mathbf{S} \quad , \quad \text{with } g_s = 2. \quad (2.3)$$

It has to be pointed out that all the particles that together with the electrons make up the ordinary matter, namely protons and neutrons, also have a spin quantum number  $s = 1/2$ . However, in the family of particles in high energy physics, as well as in the zoo of quasiparticles (i.e. collective excitation phenomena described as equivalent particles) in condensed matter physics, the spin quantum number can have other values than  $1/2$ , and is in particular integer or semi-integer, which distinguishes the two families of bosonic and fermionic particles, respectively. Throughout this Chapter, though, only the particular case of  $s = 1/2$  particles will be considered.

### Spin-orbit interaction

Because of the motion of an electron with respect to the nucleus of an atom, in the electron rest frame the electron experiences a magnetic field generated by the motion of the nucleus that is proportional to the electron orbital angular momentum  $\mathbf{L}$ . The interaction of the magnetic dipole  $\boldsymbol{\mu}_s$  with such magnetic field is called *spin-orbit interaction*, and the magnetic dipole energy  $\Delta E_{SO} = -\boldsymbol{\mu}_s \cdot \mathbf{B}$  is called spin-orbit energy, which is  $\Delta E_{SO} \propto \mathbf{S} \cdot \mathbf{L}$  in the case of a central potential experienced by the electron. The torque acting on  $\boldsymbol{\mu}_s$  will make both  $\mathbf{L}$  and  $\mathbf{S}$  undergo a precessional motion with the orientation of one depending on the orientation of the other. The result is that their vectorial sum, called total angular momentum  $\mathbf{J} = \mathbf{L} + \mathbf{S}$ , has a fixed magnitude  $J$  and fixed  $z$  component  $J_z$ .

### On the nature of spin

It is interesting to notice that, in most of the textbooks, spin is introduced as an "intrinsic", or "internal" property of a particle, pretty much at the same ontological level of mass and charge. In particular, the distinction with the "extrinsic" orbital angular momentum  $\mathbf{L}$  is often pointed out: whereas  $\mathbf{L}$  is an angular momentum due to the rotational movement of a particle,  $\mathbf{S}$  is an angular momentum only to the extent that it couples with  $\mathbf{L}$  to form the total angular momentum, but is purely a quantum property without any classical analog. It is indeed true that spin does not arise from the rigid rotation of a body: a simple calculation would show that the rotation of an electron (considered as an extended sphere with a plausible estimated radius instead of a point particle) around its axis would exceed the speed of light by several orders of magnitude in order to obtain an angular momentum equal to  $\hbar/2$ . It thus looks like that since the early years of quantum mechanics there has been no improvement in the understanding of the nature of spin, which is merely introduced *ad hoc* as an intrinsic property. Indeed, even when considering the relativistic Dirac equation (see Section 2.3.1) where spin naturally arises from the mathematics by imposing the conservation law of angular momentum, no direct insight in the physical origin of it is usually given.

Nevertheless, as explained in Ref. [72], there exists since many decades a physical interpretation of the spin which is completely consistent with standard quantum mechanics. However, since it was not emphasized at the time of the discovery and since it requires advanced quan-

## Chapter 2. Spin polarized electrons

---

tum field theory, it is often not even mentioned in textbooks. In the following, a brief sketch of the interpretation is given without rigorousness.

In Maxwell classical electrodynamics, the Poynting vector of a circularly polarized wave with finite transverse extent, as a beam of cylindrical shape propagating along  $z$ , has a component that is perpendicular to the wave vector. The circulation of energy flow around the propagation direction is associated to an angular momentum  $S_z = U/\omega$  where  $U$  is the energy of the wave. By introducing the energy quantization condition  $U = \hbar\omega$ , one thus find the quantized spin angular momentum  $S_z = \hbar$  associated to a circularly polarized photon. If the beam is not centered around  $z$  or has an asymmetric shape, there will be an additional "orbital" angular momentum.

By analogy, F. J. Belinfante showed in 1939 [73] that the so-called momentum density vector of an electron (the equivalent of the Poynting vector, which is defined in Dirac theory as some given functional of the electron wavefunction) has two independent terms associated to the circulating flow of energy density in the rest frame of the electron. This gives rise to two distinguishable angular momenta, the orbital angular momentum and one that is calculated to be as  $\hbar/2$  times the Pauli vector operator  $\sigma$  (see Section 2.1.1), that is the spin angular momentum. For completeness, it has to be mentioned that already in 1928 V. W. Gordon had shown [74] with a similar argument that the magnetic moment of the electron is associated to a circulating flow of charge, and it happens to be proportional to the spin itself.

Therefore, ultimately, the spin of a particle does not have the same ontological status as the mass or the charge, but can be derived from them. Also, spin can be fully interpreted as an angular momentum in the sense of rotational motion: only, as circulation of energy flow instead of rotation of a rigid body.

### 2.1.1 Spin polarization

Because of the commutation relationships for the spin operators  $[\hat{S}_x, \hat{S}_y] = i\hbar\hat{S}_z$  and its cyclic permutations, only one quantization axis can be chosen along which a component of the spin  $\mathbf{S}$  of the electron is determined during a measurement, while the information on the other two components will be lost. According to Eq. (2.2), the result of the measurement will be either  $+\hbar/2$  or  $-\hbar/2$ , which are usually referred to as "up" and "down" respectively. However, three separate measurements over an ensemble of electrons can of course give information about the average distribution of all the three spatial components. In general, free electrons can have their spin with arbitrary orientation in space, so that the measurement over an ensemble will average out. However there is the possibility that a beam of electrons produced in some physical process will have the two possible spin states along a certain direction that are not equally populated. This is called a *spin polarized electron beam*, and the ensemble quantity

spin polarization along the direction  $i = x, y, z$  is introduced as the following:

$$P_i = \frac{N_i^\uparrow - N_i^\downarrow}{N_i^\uparrow + N_i^\downarrow}, \quad (2.4)$$

where  $N_i^\uparrow$  and  $N_i^\downarrow$  is the number of electrons with spin along  $i$  being "up" and "down", respectively. As an average quantity, all three spatial components of the spin polarization vector can be determined by performing three sets of measurements.

## 2.2 The Pauli representation of spin

In order to describe the quantum mechanical properties of the spin vector, it is useful to introduce the two-component term of the wavefunction  $\chi = \begin{pmatrix} a \\ b \end{pmatrix}$ , named *spinor*, together with the so-called Pauli vector  $\hat{\sigma} = \frac{2}{\hbar} \hat{\mathbf{S}}$ , of which the three spatial components are the three Pauli matrices:

$$\sigma_x = \begin{pmatrix} 0 & 1 \\ 1 & 0 \end{pmatrix}, \quad \sigma_y = \begin{pmatrix} 0 & -i \\ i & 0 \end{pmatrix}, \quad \sigma_z = \begin{pmatrix} 1 & 0 \\ 0 & -1 \end{pmatrix}, \quad (2.5)$$

which are chosen in such a way to make  $z$  the quantization axis. In such coordinate system, one finds that the eigenvalues of  $\sigma_z$  are  $+1$  (corresponding to  $+\hbar/2$  in terms of  $\hat{S}_z$ ), associated to the eigenstate  $\chi^+ = \begin{pmatrix} 1 \\ 0 \end{pmatrix}$  (i.e. "up" along the  $z$  direction) and  $-1$ , associated to the other eigenstate  $\chi^- = \begin{pmatrix} 0 \\ 1 \end{pmatrix}$  (i.e. "down" along  $z$ ). A generic spin state can then be written as superposition of this two states:

$$\chi = \begin{pmatrix} a \\ b \end{pmatrix} = a \begin{pmatrix} 1 \\ 0 \end{pmatrix} + b \begin{pmatrix} 0 \\ 1 \end{pmatrix} = a\chi^+ + b\chi^-, \quad (2.6)$$

where the normalization of the wavefunction requires that  $\langle \chi | \chi \rangle = |a|^2 + |b|^2 = 1$ . The parameter  $a$  can be interpreted as the probability of finding the eigenvalue  $+1$  if a measurement of the spin along  $z$  is performed, and similar for  $b$ . If one performs a measurement along  $x$  or  $y$ , the outcome will still be  $\pm\hbar/2$ , as it can be easily calculated that  $\pm 1$  are eigenvalues also for  $\sigma_x$  and  $\sigma_y$ . The two eigenvectors in the new basis will be  $\chi_x^+ = \frac{1}{\sqrt{2}} \begin{pmatrix} 1 \\ 1 \end{pmatrix}$  and  $\chi_x^- = \frac{1}{\sqrt{2}} \begin{pmatrix} 1 \\ -1 \end{pmatrix}$  for the measurement along  $x$ , and  $\chi_y^+ = \frac{1}{\sqrt{2}} \begin{pmatrix} 1 \\ i \end{pmatrix}$  and  $\chi_y^- = \frac{1}{\sqrt{2}} \begin{pmatrix} 1 \\ -i \end{pmatrix}$  for the measurement along  $y$ . In these two new bases, the generic spinor  $\chi$  can be written as a superposition of the two corresponding eigenstates as

$$\chi = \begin{pmatrix} a \\ b \end{pmatrix} = \frac{a+b}{\sqrt{2}} \chi_x^+ + \frac{a-b}{\sqrt{2}} \chi_x^- = \frac{a+ib}{\sqrt{2}} \chi_y^+ + \frac{a-ib}{\sqrt{2}} \chi_y^-. \quad (2.7)$$

In order to understand the direction in space  $\mathbf{e} = (\sin \vartheta \cos \varphi, \sin \vartheta \sin \varphi, \cos \vartheta)$  of a given spinor, where  $\vartheta$  is the polar angle from the  $z$  axis and  $\varphi$  is the azimuthal angle from the  $x$  axis in the

## Chapter 2. Spin polarized electrons

---

$xy$  plane, it is useful to solve the eigenvalue equation  $\hat{\sigma} \cdot \mathbf{e}\chi = \lambda\chi$ . This yields

$$\chi = \begin{pmatrix} a \\ b \end{pmatrix} = \begin{pmatrix} \cos \frac{\vartheta}{2} \\ \sin \frac{\vartheta}{2} e^{i\varphi} \end{pmatrix} \quad (2.8)$$

for the eigenvalue  $+1$ , while the solution for  $-1$  corresponds to the spin pointing towards  $-\mathbf{e}$ .

The spinor representation can be used to determine the spin polarization vector  $\mathbf{P}$  by evaluating the normalized expectation value of the Pauli vector:

$$\mathbf{P} = \frac{\langle \chi | \boldsymbol{\sigma} | \chi \rangle}{\langle \chi | \chi \rangle}. \quad (2.9)$$

By combining this with Eqs. (2.5) and (2.8), the explicit expressions for the three spatial components of  $\mathbf{P}$  can be obtained:

$$P_x = \frac{a^* b + b^* a}{|a|^2 + |b|^2}, \quad (2.10)$$

$$P_y = \frac{i(b^* a - a^* b)}{|a|^2 + |b|^2}, \quad (2.11)$$

$$P_z = \frac{|a|^2 - |b|^2}{|a|^2 + |b|^2}. \quad (2.12)$$

The total amount of spin polarization then becomes  $P = \sqrt{P_x^2 + P_y^2 + P_z^2} = \sqrt{|a|^2 + |b|^2}$ , which is equal to 1 since the pure state  $|\chi\rangle$  that describes the beam has been considered.

### 2.2.1 The density matrix formalism

When it is needed to describe a beam with spin polarization smaller than 1, that is a system which is not in a pure spin state but a *statistical mixture* of them, it is useful to make use of the so-called *density matrix formalism*. Without entering in the mathematical derivation (which can be found in Ref. [62]), the following formulas will be only reported.

For a statistical mixture of spin states  $\chi_n$ , the total spin polarization can be evaluated as

$$\mathbf{P} = \frac{\sum_n \langle \chi_n | \boldsymbol{\sigma} | \chi_n \rangle}{\sum_n \langle \chi_n | \chi_n \rangle} = \frac{\text{tr}\{\rho \boldsymbol{\sigma}\}}{\text{tr}\{\rho\}}, \quad (2.13)$$

where  $\text{tr}\{M\}$  indicates the trace of a matrix  $M$ , and  $\rho$  is the so-called *density matrix*, which is defined as

$$\rho = \sum_n |\chi_n\rangle \langle \chi_n| = \sum_n \begin{pmatrix} |a_n|^2 & a_n b_n^* \\ a_n^* b_n & |b_n|^2 \end{pmatrix} = \frac{1}{2} (\mathbb{1}_2 + \mathbf{P} \cdot \boldsymbol{\sigma}), \quad (2.14)$$



where  $\mathbb{1}_2$  is the  $2 \times 2$  identity matrix. The elements of the matrix  $\rho$  have an important physical meaning. The diagonal elements represent the probability of finding the particle in the corresponding basis state, in fact

$$\text{tr}\{\rho\} \propto (N_i^\dagger + N_i), \quad (2.15)$$

which will become useful in order to express the total intensity of the electron beam in later Chapters. On the other hand, the off-diagonal elements are associated to coherent quantum interference. In particular, the following statement can be made: if  $\rho$  is not diagonal in the  $\{|\chi_n\rangle\}$  representation, the system is said to be a *coherent superposition* of the basis states  $\{|\chi_n\rangle\}$ ; if on the other hand  $\rho$  is diagonal, the system is an *incoherent superposition* [75].

## 2.3 Elastic relativistic electron scattering

In this Section the properties in terms of spin polarization of an electron beam during an elastic scattering process in the relativistic regime<sup>1</sup> will be discussed. In particular, it will be shown how the scattering process has the dual property of analyzing power and polarizing power. In order to describe this, it is necessary to first introduce the Dirac equation.

### 2.3.1 The Dirac equation

The Schrödinger equation  $i\hbar \frac{\partial \psi}{\partial t} = -\frac{\hbar^2}{2m} \nabla^2 \psi$  for the wavefunction  $\psi$  can be obtained by substituting the corresponding operators of momentum and energy  $\hat{\mathbf{p}} : \rightarrow -i\hbar \nabla$  and  $\hat{H} : \rightarrow i\hbar \frac{\partial \psi}{\partial t}$  into the expression of the Hamiltonian function for a free particle  $H = \mathbf{p}^2 / (2m)$ . By repeating this for the relativistic energy  $H^2 = c^2 \sum_{\mu} p_{\mu}^2 + m^2 c^4$  ( $\mu = x, y, z$ ), one obtains a second-order differential equation in  $t$ , which requires the boundary condition not only for  $\psi$  but also for  $\partial \psi / \partial t$ , and it is therefore difficult to solve. However, one can split the obtained equation into the product of two linear expressions and consider them individually. This leads to the *Dirac equation* for a free particle:

$$\left[ i\hbar \frac{\partial}{\partial t} + i\hbar c \left( \alpha_x \frac{\partial}{\partial x} + \alpha_y \frac{\partial}{\partial y} + \alpha_z \frac{\partial}{\partial z} \right) - \beta m c^2 \right] \psi = 0, \quad (2.16)$$

which is correct only if the choice of the parameters  $\alpha_{\mu}$  and  $\beta$  is such that  $\alpha_{\mu} \alpha_{\mu'} + \alpha_{\mu'} \alpha_{\mu} = 2\delta_{\mu\mu'}$ ,  $\alpha_{\mu} \beta + \beta \alpha_{\mu} = 0$  and  $\beta^2 = 1$ , in order to be consistent with the second-order differential equation. These conditions cannot be satisfied with scalar numbers, but it is possible with  $4 \times 4$  matrices:

$$\alpha_{\mu} = \begin{pmatrix} 0 & \sigma_{\mu} \\ \sigma_{\mu} & 0 \end{pmatrix}, \beta = \begin{pmatrix} \mathbb{1}_2 & 0 \\ 0 & -\mathbb{1}_2 \end{pmatrix}. \quad (2.17)$$

<sup>1</sup> In the context of condensed matter, despite the energies at play are usually only of the order of eV or less, the Fermi velocity of an electron is of the order of  $\approx c/100$  given its small mass. Anyway, the term *relativistic* is used in the sense that corrections due to the spin-orbit (SO) coupling are considered (since, as it will be shown in this Section, SO coupling naturally arises from relativistic treatment of quantum mechanics).

## Chapter 2. Spin polarized electrons

Since the matrices are  $4 \times 4$ , the wavefunction in Eq. (2.16) has to have four components. It can be shown that the general form of a plane wave associated to a particle of mass  $m$  with energy  $E = \hbar\omega$  and momentum  $p_z = \hbar k$  is the following:

$$\psi = \begin{pmatrix} \psi_1 \\ \psi_2 \\ \psi_3 \\ \psi_4 \end{pmatrix} = e^{i(kz - \omega t)} \left[ A \begin{pmatrix} 1 \\ 0 \\ \frac{cp_z}{E + mc^2} \\ 0 \end{pmatrix} + B \begin{pmatrix} 0 \\ 1 \\ 0 \\ \frac{-cp_z}{E + mc^2} \end{pmatrix} \right]. \quad (2.18)$$

In order to understand the spin states described by this wavefunction, one needs to find the spin operator  $\hat{\mathbf{S}}$  in the relativistic case, which can be done by exploiting the conservation law of angular momentum. From Eq. (2.16) one can write the Dirac Hamiltonian  $H = c\boldsymbol{\alpha}\mathbf{p} + \beta mc^2 + V$ , where the central potential  $V$  has been included and where  $\boldsymbol{\alpha}$  is the vector with the three spatial components  $\alpha_\mu$ . It can be shown that, contrary to the non-relativistic case,  $[\hat{\mathbf{L}}, \hat{H}] \neq 0$ , which means that  $\hat{\mathbf{L}}$  is not a constant of the motion. It is therefore necessary to introduce another operator  $\hat{\mathbf{S}}$ , defined by  $[\hat{\mathbf{S}}, \hat{H}] = -[\hat{\mathbf{L}}, \hat{H}]$ , in such a way that it is possible to write the conservation of total angular momentum law  $[\hat{\mathbf{L}} + \hat{\mathbf{S}}, \hat{H}] = [\hat{\mathbf{J}}, \hat{H}] = 0$ , which shows how spin-orbit (SO) coupling (see Section 2.1) is intrinsic to the relativistic treatment of quantum mechanics. By doing this, it turns out that  $\hat{\mathbf{S}} = \frac{\hbar}{2}\hat{\boldsymbol{\sigma}}^r$ , where  $\hat{\boldsymbol{\sigma}}^r$  is the relativistic generalization of the Pauli vector with  $4 \times 4$  matrix spatial components:

$$\sigma_\mu^r = \begin{pmatrix} \sigma_\mu & 0 \\ 0 & \sigma_\mu \end{pmatrix}, \text{ with } \mu = x, y, z, \quad (2.19)$$

where  $\sigma_\mu$  are the non-relativistic Pauli matrices from Eq. (2.5). Now, by using the wavefunction from Eq. (2.18) to solve the eigenvalue equation for  $\sigma_z$ , one finds that the two terms of Eq. (2.18) are eigenstates for spin "up" and "down" along  $z$ , respectively. However, their superposition does not allow to obtain an eigenstate of  $\sigma_x$  or  $\sigma_y$ , contrary to the non-relativistic case. Because of the spin-orbit coupling, an appropriate description of the spin polarization will work only in the electron rest frame. Otherwise, in the laboratory frame one can calculate from Eq. (2.9) that for a beam of electrons polarized along  $x$  [ $A = B = 1$  in Eq. (2.18)],  $P_x = \gamma^{-1} = \left(1 + \frac{E_k}{mc^2}\right)^{-1} \neq 1$ , where  $\gamma$  is the relativistic Lorentz factor. For example, for a kinetic energy  $E_k = 40$  keV, one obtains  $P_x = 0.927$ .

### 2.3.2 Mott scattering

In order to describe the relativistic electron scattering in a central potential, a process that goes under the name of *Mott scattering*, it is required to consider the Dirac equation with an incident plane wave along  $z$ , and to look for solutions with the asymptotic form

$$\psi_\lambda \xrightarrow{r \rightarrow \infty} a_\lambda e^{ikz} + a'_\lambda(\theta_M, \phi_M) \frac{e^{ikr}}{r} \quad (2.20)$$

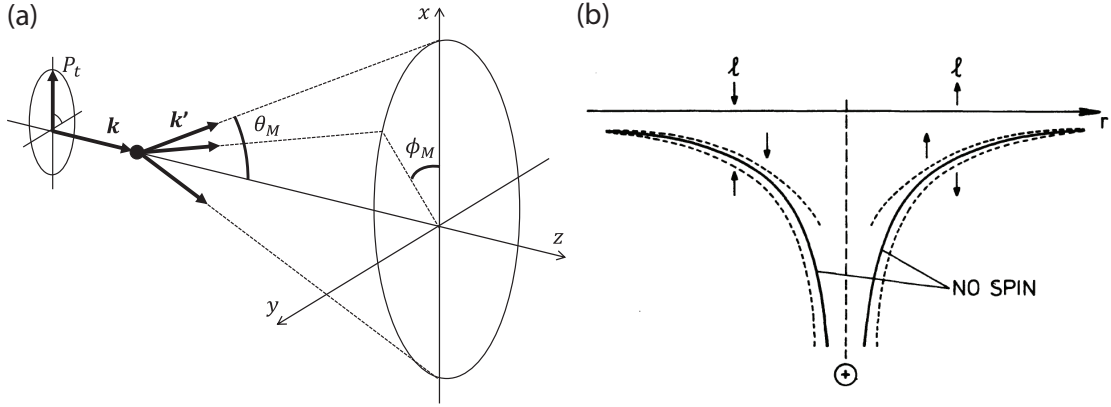


Figure 2.2: (a) Geometry of the Mott scattering. (b) Physical interpretation of the Mott scattering asymmetry in terms of spin-orbit potential correction (from Ref. [62]).

for each of the four components ( $\lambda = 1, 2, 3, 4$ ) of  $\psi$ . The angles  $\theta_M$  and  $\phi_M$  are the polar and azimuthal angles shown in Fig. 2.2(a). The differential elastic scattering cross section is given by the following expression:

$$\frac{d\sigma_{tot}}{d\Omega} \doteq \sigma(\theta_M, \phi_M) = \frac{\sum_{\lambda=1}^4 |a'_\lambda|^2}{\sum_{\lambda=1}^4 |a_\lambda|^2} \approx \frac{|a'_1|^2 + |a'_2|^2}{|a_1|^2 + |a_2|^2}, \quad (2.21)$$

where the approximation is due to the fact that, according to Eq. (2.18),  $|a_{3,4}| \ll |a_{1,2}|$ . Therefore the components  $\psi_3$  and  $\psi_4$  need not to be considered in the scattering problem, and only the reduced Dirac plane wave has to be considered:

$$\begin{pmatrix} \psi_1 \\ \psi_2 \end{pmatrix} \xrightarrow{r \rightarrow \infty} \begin{pmatrix} 1 \\ 0 \end{pmatrix} e^{ikz} + \begin{pmatrix} S_{11} \\ S_{21} \end{pmatrix} \frac{e^{ikr}}{r} \quad (2.22)$$

for an electron with spin along  $z$ , where  $S_{11}$  and  $S_{21}$  are the scattering amplitudes. In particular,  $S_{21}$ , known as "spin-flip amplitude", accounts for the possibility of changing the spin direction upon scattering because of the interaction with the magnetic field of the scatterer in the electron rest frame because of the spin-orbit coupling picture. By repeating the same for an electron with spin along  $-z$ , one can then look for the solution of an incident electron with arbitrary spin direction by coherent superposition of the two cases  $\pm z$ , and obtain  $\psi = \begin{pmatrix} A \\ B \end{pmatrix} e^{ikz}$ .

It is then possible to explicitly calculate the four scattering amplitudes as an infinite sum of partial waves with different  $\ell$ , i.e. as functions of associated Legendre polynomials and scattering phases (see Ref. [62]); for the purposes of this Chapter, however, it is sufficient to describe such four complex quantities as two complex functions of the scattering angle  $\theta_M$ :  $S_{11} = S_{22} = f(\theta_M)$  and  $S_{21} = -S_{12} e^{2i\phi_M} = g(\theta_M) e^{i\phi_M}$ . It is now possible to write Eq. (2.21) in

## Chapter 2. Spin polarized electrons

terms of the scattering amplitudes:

$$\sigma(\theta_M, \phi_M) = I_{tot}(\theta_M) \left[ 1 + S(\theta_M) \frac{-AB^* e^{i\phi_M} + A^* B e^{-i\phi_M}}{i(|A|^2 + |B|^2)} \right], \quad (2.23)$$

where  $I_{tot}(\theta_M) = |f|^2 + |g|^2$  and  $S(\theta_M)$  is the so-called Sherman function [76]:

$$S(\theta_M) = \frac{i(fg^* - f^*g)}{I_{tot}}, \quad (2.24)$$

which is a real function. It has to be pointed out that since the functions  $f$  and  $g$  describe the scattering amplitudes, they are not only function of geometry, but also electron kinetic energy and scattering potential (i.e., substance of the scatterer), and therefore so is the Sherman function. For completeness, the explicit expression of the Sherman function is here reported for the scattering by an atomic nucleus as a function of atomic number  $Z$ , kinetic energy  $E_k$  and scattering angle  $\theta_M$  [77]:

$$S = \frac{2\alpha Z \sin^3 \frac{\theta_M}{2} \ln \left( \sin \frac{\theta_M}{2} \right) \sqrt{1 - \frac{1}{\left(1 + \frac{E_k}{mc^2}\right)^2}}}{\left(1 + \frac{E_k}{mc^2}\right) \sqrt{1 - \sin^2 \frac{\theta_M}{2}} \left[ 1 - \sin^2 \frac{\theta_M}{2} \left(1 - \frac{1}{\left(1 + \frac{E_k}{mc^2}\right)^2}\right) + \pi\alpha Z \sqrt{1 - \frac{1}{\left(1 + \frac{E_k}{mc^2}\right)^2}} \sin \frac{\theta_M}{2} \left(1 - \sin \frac{\theta_M}{2}\right) \right]}, \quad (2.25)$$

where  $\alpha \approx \frac{1}{137}$  is the fine structure constant. For example, with  $Z = 79$  (Au),  $E_k = 40$  keV and  $\theta_M = 118^\circ$ ,  $S = 0.0884$ . However,  $S$  does not always have this analytical dependence on  $Z$ , but for some elements it shows a considerable increase of the scattering asymmetry, so that for example for Au a value of up to  $S = 0.33$  has been computed [78] and  $S = 0.15$  has been measured [79]. At this point it is interesting to point out the reason why the scattered solution depends on the azimuthal angle  $\phi_M$ , contrary to the non-relativistic treatment with the Schrödinger equation: because of spin-orbit coupling, the angular momentum conservation law stands for the quantity  $\mathbf{J}$ , and the spin-flip described by  $S_{21}$  implies a variation of  $S_z$ , that has to be compensated by a variation of  $L_z$ . In spherical coordinates  $\hat{L}_z = \hat{L}_z(\phi_M)$ , and thus also  $\sigma$  will depend on  $\phi_M$ .

As an example, the case of an electron beam fully polarized along  $x$  is considered. In this case Eq. (2.23) becomes:  $\sigma = I_{tot}(\theta_M) [1 - S(\theta_M) \sin \phi_M]$ . It is clear that the scattering is azimuthally asymmetric, and in particular the asymmetry is maximized for  $\phi_M = 90^\circ$  and  $\phi_M = 270^\circ$ . Such asymmetry is at the basis of the measurement of spin polarization of electrons in a *Mott polarimeter*, as it is described in Section 3.2.1. A simple way of interpreting the physical reason for the asymmetry is shown in Fig. 2.2(b). In the presence of spin-orbit coupling, the scattering potential is modified by a term  $\sim \mathbf{L} \cdot \mathbf{S}$ , which is therefore a positive or negative correction depending on whether the spin is parallel or antiparallel to the angular momentum, respectively. This makes less or more probable the scattering event in one particular direction.

It is useful to apply the density matrix formalism introduced in Section 2.2.1 in order to highlight the link between differential cross-section, Sherman function and spin polarization. For this, the spinor  $\chi = \begin{pmatrix} A \\ B \end{pmatrix}$  in the initial state is considered, and upon scattering it is transformed into

$$\chi' = \begin{pmatrix} Af - Bge^{-i\phi_M} \\ Bf + Age^{i\phi_M} \end{pmatrix} = \begin{pmatrix} f & -ge^{-i\phi_M} \\ ge^{i\phi_M} & f \end{pmatrix} \chi \doteq \mathbb{S}\chi, \quad (2.26)$$

where  $\mathbb{S}$  is defined as spin scattering matrix. Now it is possible to evaluate the two density matrix for the unscattered state  $\rho = \chi\chi^\dagger$  and for the scattered state  $\rho' = \mathbb{S}\chi\chi^\dagger\mathbb{S}^\dagger$ , where the dagger symbol indicates the adjoint of the operator. By combining with Eq. (2.14) it follows that

$$\rho' = \mathbb{S}\rho\mathbb{S}^\dagger = \frac{1}{2}\mathbb{S}(\mathbb{1}_2 + \mathbf{P}\boldsymbol{\sigma})\mathbb{S}^\dagger \text{tr}\{\rho\}, \quad (2.27)$$

and therefore one can rewrite the differential cross-section as

$$\sigma = \frac{\text{tr}\{\rho'\}}{\text{tr}\{\rho\}} = \frac{1}{2}\text{tr}\left\{\mathbb{S}(\mathbb{1}_2 + \mathbf{P}\boldsymbol{\sigma})\mathbb{S}^\dagger\right\} = I(\theta_M)[1 + S(\theta_M)\mathbf{P}\cdot\mathbf{n}], \quad (2.28)$$

which follows from geometrical considerations after choosing  $\varphi = 0^\circ$ , and where  $\mathbf{n}$  is the unitary vector perpendicular to the scattering plane defined by the electron momenta before and after scattering,  $\hbar\mathbf{k}$  and  $\hbar\mathbf{k}'$ :  $\mathbf{n} = \frac{\mathbf{k}\times\mathbf{k}'}{|\mathbf{k}\times\mathbf{k}'|} = (-\sin\phi_M, \cos\phi_M, 0)$ . The last expression in Eq. (2.28) is the basic equation of Mott scattering, and it illustrates how the scattering asymmetry is due only to the component of the polarization vector perpendicular to the scattering plane  $P_n = \mathbf{P}\cdot\mathbf{n} = -P_t \sin\phi_M$ . The term  $P_t$  is the transverse component of  $\mathbf{P}$ , as shown in Fig. 2.2(a), and this shows how the longitudinal component  $P_z$  does not play a role in the asymmetry, as it will be described in Section 3.2.1.

It is particularly interesting to consider the case of scattering of a beam of unpolarized electron where  $\mathbf{P} = 0$ . From Eq. (2.27) and Eq. (2.28) one finds  $\sigma = I(\theta_M)$ , whereas by combining Eq. (2.27) with Eq. (2.13) the spin polarization  $\mathbf{P}'$  of the scattered beam can be obtained:

$$\mathbf{P}' = \frac{1}{2}\text{tr}\left\{\mathbb{S}\mathbb{S}^\dagger\boldsymbol{\sigma}\right\} \frac{\text{tr}\{\rho\}}{\text{tr}\{\rho'\}} = \frac{i(fg^* - f^*g)}{|f|^2 + |g|^2} \mathbf{n} = S(\theta_M)\mathbf{n}. \quad (2.29)$$

Therefore, the Sherman function has a dual physical meaning: it describes the asymmetry in the scattering of a polarized beam but also **the amount of polarization of a scattered unpolarized beam**. This last result will become relevant in photoemission from spin-degenerate states as described in Section 3.3. The more general case of a scattered polarized beam and its consequences in photoemission are outlined in Section 4.6.



## 3 Photoemission spectroscopy

*“Solo dopo aver conosciuto la superficie delle cose, ci si può spingere a cercare quel che c'è sotto. Ma la superficie delle cose è inesauribile.”*

*“It is only after you have come to know the surface of things, that you can venture to seek what is underneath. But the surface of things is inexhaustible.”*

- Italo Calvino, *Palomar* (1983)

In this Chapter, the basics of the photoemission process will be discussed. The experimental setup used to perform the experiments presented in later Chapters will be briefly described, with emphasis on the basics of the Mott spin polarimeter. The formalism introduced in Chapter 2 will be employed to describe an interference process that gives rise to a spin polarization when measuring spin-degenerate states.

### 3.1 The photoemission process

Since the discovery of the *photoelectric effect* by Heinrich Rudolf Hertz in 1887 [80], when he observed that UV light could influence the electric sparks produced between two metallic contacts [81], the photoemission process has played a central role in modern physics. As proposed by Albert Einstein in 1905 [82] and demonstrated by Robert Andrews Millikan in 1914 [83] (milestone works that made them win the Nobel prize in 1921 and in 1923 respectively), when a quantum of light, nowadays known as *photon*, hits the surface of a material, an electron can absorb its energy and escape from the surface of the material with a maximum kinetic energy of  $E_k^{max} = h\nu - \Phi$ . The energy of the photon is  $h\nu$ , where  $h$  is the Planck constant and  $\nu$  is the frequency of the light, while  $\Phi$  is a material-dependent quantity called *workfunction* (of the order of  $\sim 5eV$ ), that can be seen as the potential barrier at the surface that prevents electrons to be freely released from a solid. These electrons are commonly called *photoelectrons* and are said to be *photoemitted* from the material under investigation.

The electron inelastic mean free path (IMFP), i.e. the length an electron can travel in a material without being inelastically scattered, is a function of the electron kinetic energy and rather independent on the material considered. The plot of IMFP versus kinetic energy is shown in

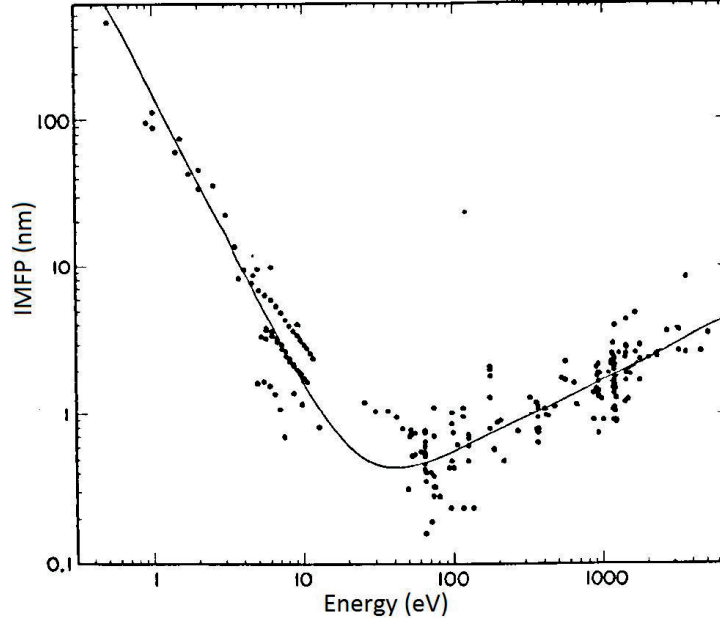


Figure 3.1: The "universal curve": electron mean free path for different elements as a function of electron energy relative to the Fermi level. Adapted from [84], where the elements considered are tabulated.

Fig. 3.1 and is known in literature as the "universal curve". For typical incident photon energies, usually in the UV and soft X-ray range in order to have a reasonably high photoemission cross-section, the mean free path is of the order of only a few nm, which makes any technique based on the photoemission process definitely *surface sensitive*. Thus it is only in the 1960's, after the developments of ultra-high vacuum (UHV,  $p < 10^{-9}$  mbar) technology, that photoemission became a mean to probe the electronic properties of a material, thanks to the work of Kai Siegbahn (Nobel Prize in 1981) and many others.

By measuring the kinetic energy  $E_k$  and the momentum of the photoemitted electrons in UHV one can infer the energy-momentum dispersion relationship of the electrons inside the solid by exploiting energy and momentum conservation laws. This goes under the name of *photoemission spectroscopy* (PES), or photoelectron spectroscopy. By indicating with  $\mathbf{k}$  the wave-vector of the electron inside the material and with  $\mathbf{K}$  the one outside in vacuum, one has the following well-known equations:

$$h\nu = E_k + |E_b| + \Phi_s, \quad (3.1)$$

$$K_x = \frac{\sqrt{2mE_k}}{\hbar} \sin\theta \cos\alpha = k_x, \quad (3.2)$$

$$K_y = \frac{\sqrt{2mE_k}}{\hbar} \sin\theta \sin\alpha = k_y, \quad (3.3)$$

$$K_z = \frac{\sqrt{2mE_k}}{\hbar} \cos\theta \neq k_z = \frac{1}{\hbar} \sqrt{2m(E_k \cos^2\theta + V_0)}. \quad (3.4)$$



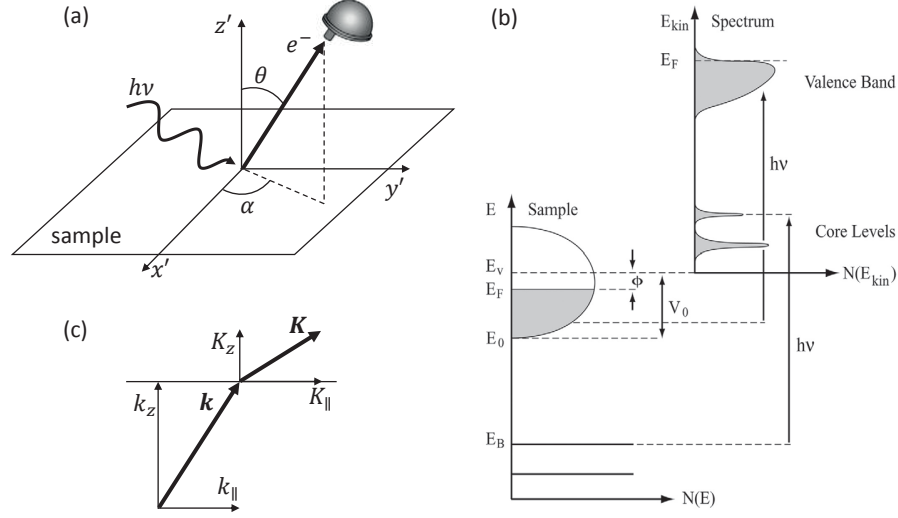


Figure 3.2: (a) Geometry of photoemission [the prime in the coordinate system is used to distinguish it from the sample spin frame of Fig. 3.6(e)]. (b) Energetics of the photoemission process, from Ref. [85]. (c) Photoelectron momentum inside ( $\mathbf{k}$ ) and outside ( $\mathbf{K}$ ) the crystal.

A detailed discussion of these formulas can be found on many reviews about photoemission (see for example Refs. [85–87]). The angles  $\theta$  and  $\alpha$  are defined in Fig. 3.2(a). Since the setup used for this Thesis has the analyzer in a fixed position [see Fig. 3.6(e)], the angles are varied by rotating the sample. Also, the sample coordinate frame in Fig. 3.6(e) is rigid with the sample surface independently from  $\alpha$ . Therefore in this Thesis the angle  $\alpha$  is used to determine the orientation of the Brillouin zone (BZ) of the crystal in reciprocal space, without entering the definition of  $k_x$  and  $k_y$ . Simply, the polar angle  $\theta$  that allows to access the different points of the BZ will be different for  $k_x$  and  $k_y$ , and namely it will be  $\theta_p$  (polar) if it scans along  $k_x$ , and  $\theta_t$  (tilt) if it scans along  $k_y$  [see Fig. 3.6(e)].

Eq. (3.1) is the *Einstein's formula* for energy conservation, where  $E_b$  is the binding energy of the electron inside the material, as shown in Fig. 3.2(b). The workfunction  $\Phi_s$  that enters in Eq. (3.1) is not the  $\Phi$  of the sample, but the one of the spectrometer. In fact in the experiment both sample and spectrometer are grounded, thus their Fermi level has to coincide. Therefore the vacuum level which the measured kinetic energy is referred to is the one of the spectrometer, which will be at  $\Phi_s$  above the Fermi level. Eqs. (3.2)-(3.4) can be obtained by considering that the photoelectron outside the material is a free particle of momentum  $\mathbf{p} = \hbar\mathbf{k}$  with kinetic energy  $\frac{p^2}{2m}$ , and by noticing that because of the translational symmetry conserved along  $x$  and  $y$  at the interface between the material and the vacuum,  $K_x^2 + K_y^2 = K_{\parallel}^2 = k_x^2 + k_y^2 = k_{\parallel}^2$ . Also, the momentum of the photon  $h\nu/c$  is neglected, since for energies in the UV range it is very small if compared with typical Brillouin zone sizes, but it can be easily incorporated for soft X-ray photoemission. On the other hand, as shown in Fig. 3.2(c), the momentum component perpendicular to the surface is not conserved, and needs to be evaluated. Under the *free-electron final state approximation*, the electron in the final state inside the material is taken as a free electron so that  $E_f = E_k + \Phi_s = \frac{\hbar^2}{2m}(\mathbf{k}_{\parallel}^2 + \mathbf{k}_z^2) - |E_0|$ , where  $|E_0|$  determines

where in energy the bottom of the final state parabolic dispersion is placed with respect to the Fermi level. By combining this with Eqs. (3.2) and (3.3) one finds the result in (3.4), where  $V_0 = |E_0| + \Phi_s$  is called *inner potential*. Several approaches are possible to determine  $V_0$ . For example, in literature [85, 86] this is often done by setting  $|E_0|$  as the bottom of the valence band, as it is shown in Fig. 3.2(b), since it corresponds to the bottom of the potential well set by the crystal. However this simplification is often too rough, and the most common way to experimentally determine  $V_0$  is to match the crystal periodicity in reciprocal space along  $k_z$  with the periodicity of the photoemission intensity as a function of  $h\nu$ . Another more accurate experimental approach consists in combining several measurement on different sample surfaces by using a triangulation method, which however cannot be applied when different facets of the sample are not easily accessible [88].

### Surface vs. bulk

At this point it is useful to point out that being a surface sensitive technique, PES can probe only electronic state that are strong enough at the surface of a material. This includes 2D surface states as well as 3D bulk states. The last ones, however, are not necessarily the same as they are in the bulk of the crystal, since the presence of the surface modifies the local potential to which these states are solutions. Thus any time "bulk states" are mentioned in the PES context, they should be intended as "bulk-derived states at the crystal surface". In extreme cases where the intensity is highly amplified because of the surface, they are often called bulk-surface resonances. Also atomic core levels bring information about the chemical composition at the surface, which is not necessarily the same as in the bulk. Finally, one should always consider that while 2D states can be studied more naturally by PES because of their intrinsic lack of  $k_z$  dispersion, for the study of bulk states the  $k_z$  dispersion and the issue of not knowing the parameter  $V_0$  have to be taken into account.

#### 3.1.1 The 3-step and the 1-step models of photoemission

A simple description of the photoemission process is the so-called *3-step model* [89, 90]. It consists in dividing the process into three separate steps: excitation of an initial Bloch state into a final Bloch state by absorption of a photon, then traveling of the excited electron towards the crystal surface, and finally transmission through the surface barrier to the vacuum to become a free particle. The first step, when the dispersion of the final Bloch state is not known from calculations, can be simplified by making the free-electron final state approximation previously discussed. The last two steps are simply described by a probability of transport and transmission, respectively, while only the first step contains all the information about the material band structure. Whereas it can be often employed with good results to describe many qualitative features, the 3-step model is an artificial separation of one single process as a whole, and cannot highlight subtle quantitative variations of the photoemission intensity and possible interference phenomena that can take place during the process. For this, one needs to consider the *1-step model*, where the photoemission is rigorously treated as a single

quantum mechanical coherent process. In this case, the final state reached by the electron upon absorption of a photon is an excited state of the system that matches the boundary condition of becoming a free-particle wavefunction at the interface with vacuum.

The photoemission intensity is described by the transition probability of optical excitation  $W_{fi}$  given by the Fermi golden-rule:

$$W_{fi} = \frac{2\pi}{\hbar} |\langle \psi_f | \hat{H}_{int} | \psi_i \rangle|^2 \delta(E_f(\mathbf{k}) - E_i(\mathbf{k}) - h\nu), \quad (3.5)$$

where the  $\delta$  function assures energy conservation,  $\psi_i$  and  $\psi_f$  are the initial and final states of energy  $E_i$  and  $E_f$  respectively, and  $\hat{H}_{int}$  is the transition operator describing the interaction with the photon. The matrix element in Eq. (3.5) can be rewritten as the integral  $\iiint_{-\infty}^{+\infty} \psi_f^* \hat{H}_{int} \psi_i d\mathbf{r}$  and its result is a complex number, which is useful for the following Chapters to write as a radial term  $R$  and phase term  $\phi$ :

$$M_{fi} = \langle \psi_f | \hat{H}_{int} | \psi_i \rangle = R e^{i\phi}. \quad (3.6)$$

The operator  $\hat{H}_{int}$  can be expressed in perturbation theory by introducing the transformation  $\hat{\mathbf{p}} \mapsto \hat{\mathbf{p}} - e\hat{\mathbf{A}}$  into the unperturbed Hamiltonian operator  $H_0 = \frac{\hat{\mathbf{p}}^2}{2m} + V$ , where  $\hat{\mathbf{p}}$  is the generalized momentum operator  $\hat{\mathbf{p}} := -i\hbar\nabla$ , thus obtaining  $\hat{H} = \hat{H}_0 + \hat{H}_{int}$ . The charge of the electron is  $-e$ , the operator  $\hat{\mathbf{A}}$  is the electromagnetic vector potential, and the gauge with scalar electric potential equals zero has been chosen. In this gauge,  $\mathbf{A} = A_0 \boldsymbol{\epsilon} e^{i\mathbf{k}_{hv}\mathbf{r}}$ , where  $\boldsymbol{\epsilon}$  is the unitary vector in the direction of the electric field of the light, and  $\mathbf{k}_{hv}$  is the photon momentum. By neglecting the quadratic term in  $A^2$ , and considering the so-called *dipole approximation*, i.e. the photon wavelength is larger than the characteristic interatomic distances (so that  $e^{i\mathbf{k}_{hv}\mathbf{r}} \approx 1$ ), one finds

$$\hat{H}_{int} := \frac{-e}{m} \hat{\mathbf{A}} \cdot \hat{\mathbf{p}} = \frac{-eA_0}{m} \boldsymbol{\epsilon} \cdot \hat{\mathbf{p}}. \quad (3.7)$$

The matrix element of  $\hat{H}_{int}$  written in this form is known as the *velocity form* of the optical transition matrix element  $M_{fi}$ .

Another way of expressing  $\hat{H}_{int}$  makes use of the equivalency  $\langle \psi_f | \hat{\mathbf{p}} | \psi_i \rangle = \frac{-m(E_f - E_i)}{i\hbar} \langle \psi_f | \hat{\mathbf{r}} | \psi_i \rangle$ , where  $\hat{\mathbf{r}}$  is the electron position operator, which follows from the commutation relationship  $[\hat{H}, \hat{\mathbf{r}}] = -\frac{i\hbar}{m} \hat{\mathbf{p}}$ . In this way one obtains

$$\hat{H}_{int} = \frac{eA_0(E_f - E_i)}{i\hbar} \boldsymbol{\epsilon} \cdot \hat{\mathbf{r}} = -\frac{A_0(E_f - E_i)}{i\hbar} \boldsymbol{\epsilon} \cdot \hat{\mathbf{d}}, \quad (3.8)$$

where  $\hat{\mathbf{d}} = -e\hat{\mathbf{r}}$  is the *electric dipole operator*. The matrix element of such expression for  $\hat{H}_{int}$  is known as *length form* of  $M_{fi}$ .

At this point, instead of proceeding with the analytical expressions of the wavefunctions [91], in order to consider the crystal as a whole N-electron system it is more insightful to consider

another approach, developed by John Pendry [92], that relies on the second quantization formalism and the use of Green functions. Several publications can be found on the topic, both introductory [85, 87, 93] and advanced [92, 94–97]. In the following, only what is useful for the purpose of this Thesis will be presented.

In a multiple scattering theory, reminiscent of the Extended X-ray Absorption Fine Structure (EXAFS) formalism, the crystal is decomposed into a semi-infinite stack of layers made of muffin-tin potentials, and the photoemission current is described by the combined contribution of four scattering events: scattering by the single atom, within a layer, in between the layers and at the surface. This is a density functional theory (DFT) method, known as fully relativistic self-consistent Korringa-Kohn-Rostoker (KKR) Green function method [95, 97], and it allows to evaluate in one-step the matrix elements  $M_{fi}$ . Then by making use of the density matrix formalism introduced in Chapter 2, it is also possible to introduce the information about the spin polarization [98]. Some results of this kind of calculations will be presented in Chapter 5.

In second quantization notation, the Hamiltonian that describes the photon-electron interaction becomes

$$\hat{H}_{int} = \sum_{\mathbf{k}, \mathbf{K}} \left\langle \psi_f^1 \left| \frac{-eA_0}{m} \boldsymbol{\epsilon} \cdot \hat{\mathbf{p}} \right| \psi_i^1 \right\rangle \hat{c}_{\mathbf{K}}^\dagger \hat{c}_{\mathbf{k}} = \sum_{\mathbf{k}, \mathbf{K}} m_{fi}^1 \hat{c}_{\mathbf{K}}^\dagger \hat{c}_{\mathbf{k}}, \quad (3.9)$$

where the  $\hat{c}_{\mathbf{K}}^\dagger$  and  $\hat{c}_{\mathbf{k}}$  are the creation operator of an electron with momentum  $\mathbf{K}$  and annihilation operator of an electron with momentum  $\mathbf{k}$ , respectively. The complex number  $m_{fi}^1$  is the *one-electron matrix element* [99], not to be confused with  $M_{fi}$ . The state  $|\psi_i^1\rangle$  is the one-electron initial state wavefunction, which can be considered for simplicity as a Bloch wave  $\Phi_{\mathbf{k}}$ , even if one should take into account a linear combination of Bloch waves of the crystal that are weighted to meet the boundary condition of the crystal surface. Whereas in the three-step model the one electron final state  $|\psi_f^1\rangle$  is also described by Bloch waves, in the one-step model it has to have the following asymptotic behaviour [91, 93]:

$$\lim_{z \rightarrow +\infty} \psi_f^1 = e^{ik_{\parallel} r_{\parallel}} \left( e^{iK_z z} + \mathcal{R}^* e^{-iK_z z} \right), \quad (3.10)$$

$$\lim_{z \rightarrow -\infty} \psi_f^1 = \mathcal{T} e^{(ik_{\parallel} r_{\parallel} + ik_z z)} \Phi_{\mathbf{k}}(z), \quad (3.11)$$

and the two solutions have to match at the crystal surface. The direction  $z$  is along the surface normal and points away from the surface. The resulting wavefunction can be recognized as the complex conjugate of a state describing a low-energy electron diffraction (LEED) process, and it is therefore known in literature as *time-reversed LEED state*. The coefficients  $\mathcal{R}$  and  $\mathcal{T}$  are the reflection and transmission coefficients, respectively, in LEED formalism.

Now, given the interaction Hamiltonian in Eq. (3.9), one has to evaluate the photoemission intensity from the Fermi golden rule of Eq. (3.5). The initial state of the  $N$  particle system is  $|\psi_i\rangle = |\psi_i^N\rangle = \hat{\mathcal{A}}(\Phi_{\mathbf{k}} \otimes \psi_i^{N-1})$ , where  $\hat{\mathcal{A}}$  is an operator that antisymmetrizes the wavefunc-

tions product in order to satisfy the Pauli principle. In this way, one electron  $\Phi_{\mathbf{k}}$  is explicitly considered with respect to the rest of the system  $\psi_i^{N-1}$ , and it has to be pointed out that  $\psi_i^{N-1}$  is not an eigenstate of the  $(N-1)$  Hamiltonian. A similar separation is done for the final state  $|\psi_f\rangle = |\psi_f^N\rangle \approx \hat{\mathcal{A}}(\psi_f^1 \otimes \psi_f^{N-1})$ , or  $|\psi_f^N\rangle \approx \hat{c}_{\mathbf{k}}^\dagger |\psi_f^{N-1}\rangle$  in second quantization, where the so-called "sudden" approximation has been made, which will be discussed in the following Section. For the moment, it is possible to explicitly write the photoemission transition probability as

$$W_{fi} \propto \left| \sum_{\mathbf{k}} m_{fi}^1 \langle \psi_f^{N-1} | \hat{c}_{\mathbf{k}} | \psi_i^N \rangle \right|^2 \delta_E = \sum_{\mathbf{k}} |m_{fi}^1|^2 \cdot \left| \langle \psi_f^{N-1} | \hat{c}_{\mathbf{k}} | \psi_i^N \rangle \right|^2 \delta_E, \quad (3.12)$$

where the  $\delta_E$  is the delta function that assures energy conservation as usual. Summing the second term of the last expression over all the possible eigenstates  $|\psi_f^{N-1}\rangle$  in order to obtain an expression proportional to the photoemission total intensity gives what is called the *spectral density function*  $A(\mathbf{k}, E)$ , which contains all the information of the many-body effects in the photoemission process. This is the key quantity of DFT calculations, since it is possible to evaluate it with Green function formalism without solving an N-particle problem but using a single functional that describes the electron density. On the other hand, the one-electron matrix element  $m_{fi}^1$  depends on extrinsic factors such as light polarization and experimental geometry. Noticeably, the experimental intensity modulation that results from the term  $|m_{fi}^1|^2$  is what is typically referred to as "matrix element effects" in common experimental photoemission language; this however can be a bit confusing in the context of this Thesis, since the relationship between spin polarization and time delay in photoemission relies on interfering channels in the matrix element  $M_{fi}$ , as it was introduced in Chapter 1 and it will be discussed in Chapter 4. Also, it has to be noticed that the last passage in Eq. (3.12) is not true if there were more than one possible channel  $\hat{c}_{\mathbf{k}}$ , since there would be an interference effect from the evaluation of the modulus square, which would require a more sophisticated definition of spectral function. It is therefore more useful, for the purposes of this Thesis, to just consider the full matrix element  $M_{fi} = Re^{i\phi}$ , without further decompositions.

At this point it is also important to mention the well-known *dipole transition selection rules*. A somehow lengthy calculations where the quantum numbers  $n$ ,  $\ell$  and  $m_\ell$  are explicitly taken into account in the initial and final state of the one-electron matrix element shows [9] that this matrix element is non-zero if and only if  $\Delta\ell = \pm 1$ . When taking the SO coupling into account, one can also show that  $\Delta m_j = 0$  if linearly polarized light is used and  $\Delta m_j = \pm 1$  if circularly polarized light  $\zeta^\pm$  is used.

#### 3.1.2 The "sudden" approximation

In the previous Section, the so-called "sudden" approximation has been used. Mathematically, its meaning is clear: it requires the entangled final state of the system, made of  $(N-1)$  particles left in the solid and a photoemitted electron, to be written as an antisymmetric product of

two separate wavefunctions for the photoelectron and the  $(N - 1)$  system. That is, as already shown,

$$\left| \psi_f^N \right\rangle \approx \hat{\mathcal{A}} \left( \psi_f^1 \otimes \psi_f^{N-1} \right) = \hat{c}_{\mathbf{K}}^\dagger \left| \psi_f^{N-1} \right\rangle, \quad (3.13)$$

which is necessary in order to separate the one-electron matrix element from the spectral function. The main argument in favor of such an approximation is that, *a posteriori*, the agreement between measured photoemission intensities and calculated spectral functions is very often remarkably good. The word "sudden" has been used in literature as a physical justification because of the following: if the electron is *fast enough*, its interaction with the charged  $(N - 1)$  system will be negligible, and thus one can consider the whole system as two separate objects [85–87, 94, 95]. In other words, the removal of the electron is considered *instantaneous*, therefore the word "sudden", so that there is no time to interact with the system left behind. However, there are some limitations to this interpretation of Eq. (3.13):

- First, it does not fit well the picture of the one-step model. In fact, whereas in the three-step model one applies the sudden approximation in the first step and then can introduce a loss function to account for possible scattering events in the second and third step, in the one-step model it is somehow arbitrary to assume no interaction of the photoelectron with the system, since the whole idea of the one-step model is to consider the full quantum mechanical process.
- Second, it is not clear what "fast enough" means. In fact, the photoelectron will always feel the long-range Coulomb interaction with the photohole left in the system, at least until the hole is filled (hole lifetimes are of the order of a few fs, up to several hundreds of fs [100]). This indeed corresponds to the Coulomb logarithmic correction to the photoemission time delay mentioned in Section 1.3, and it is not necessarily negligible, as shown in the following simple example. The photoionization of an electron from a Hydrogen atom can be simplified as an electron (mass  $m$ , charge  $-|q|$ ) moving in 1D along  $x$  with initial velocity  $v_0 = \sqrt{2E_k/m}$ , where  $E_k$  is the kinetic energy from Eq. (3.1), starting at position  $x_0$  from a fixed proton, which provides a deceleration to the electron because of the Coulomb force. Thus from kinematics one can calculate the time lag  $\Delta t = t^{\text{Coul.}} - t^{\text{free}}$  between the electron that feels the Coulomb force and the case of free motion without Coulomb interaction<sup>1</sup>. This time delay has already been introduced in Section 1.3 as  $\Delta \tau_{\text{ln}}$ . In Fig. 3.3 the plot of  $\Delta t(x)$  and  $\Delta t(E_k)$  are shown for  $x_0 = 1 \text{ \AA}$ . For  $E_k = 45 \text{ eV}$ , for example, there is a lag of  $\approx 1$  as between the two cases after a travel of  $1 \text{ \AA}$ , a lag of  $\approx 40$  as after  $1 \text{ nm}$ , and  $\approx 240$  as after  $5 \text{ nm}$ .

---

<sup>1</sup> The explicit expression is given by:

$$\Delta t = \left( \int_{x_0}^x \frac{dx'}{\sqrt{\frac{2kq^2}{m} \left( \frac{1}{x'} - \frac{1}{x_0} \right) + \frac{2E_k}{m}}} \right) - \left( \frac{x - x_0}{\sqrt{\frac{2E_k}{m}}} \right).$$

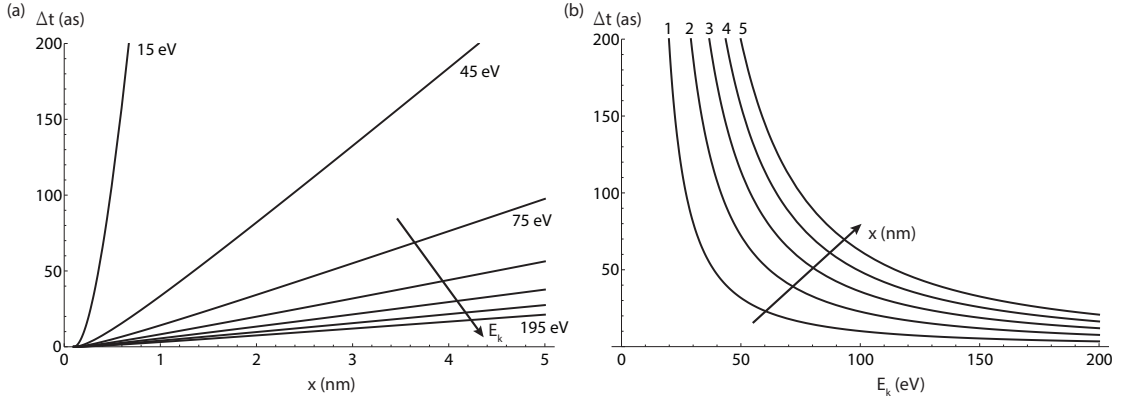


Figure 3.3: Simulation of time lag  $\Delta t$  between an electron moving with initial velocity  $v_0$  that feels a deceleration because of Coulomb interaction with a proton and an electron in free motion, as a function of (a) position  $x$  for different kinetic energies (from 15 eV to 195 eV, step of 30 eV) and (b) kinetic energy  $E_k$  for different positions (from 1 nm to 5 nm, step of 1 nm).

- Third, as nicely argued by Lars Hedin *et al.* in Ref. [101], whereas the interaction between photoelectron and rest of the system can be neglected in photoionization of atoms or molecules once Coulomb correction is considered, it is actually never a good approximation for solids, unless reaching extremely high kinetic energies of several keV. In fact, whereas on one side the scattering probability decreases with kinetic energy, the probing depth increases, so that the two effects are more or less balanced. Therefore in a solid one always has the combination of quasiparticle satellite structures that originates both from *intrinsic* losses (i.e. from the spectral function itself), and from *extrinsic* losses (i.e. from interaction of the photoelectron with the solid), and the extrinsic losses are not at all negligible, as the sudden approximation requires. In fact, it can be shown that the two kinds of losses coherently sum (i.e. they sum in amplitudes, and not in intensities), resulting in a quantum interference that suppresses many features in the photoemission satellite structure [101]. This interesting effect helps understanding why DFT calculations are often much richer in features than the experimental data, even when the experimental resolution is very good. Indeed, because of the sudden approximation, the extrinsic losses are not accounted for in DFT, and thus also their interference with intrinsic losses is not considered. To take this interference into account, it is in principle possible (but very difficult to apply in real systems) to not consider the sudden approximation, but to use the so-called *adiabatic limit* instead, where the calculation of the spectral function relies on time-dependent potentials where the system adiabatically adapts to the moving photoelectron.

Despite these considerations, the sudden approximation still works sufficiently well in many different cases. The word "sudden" however should not lead to misunderstandings, in particular in the context of this Thesis. In fact, as will be presented in Chapter 4, the extraction of time delay information from the measurement of spin polarization depends on the phase term of



the matrix element  $M_{fi}$ . This translates, when applying the sudden approximation, in the assumption that  $\langle \psi_f^N | \approx \langle \psi_f^{N-1} |$ , i.e. the phase of the  $(N - 1)$  system is substantially the same as the one of the  $N$  system in the final state, which is once again reasonable but justifiable only *a posteriori*. Therefore one can still consider the time delay of the photoemission process, where the sudden approximation intervenes only once the photoelectron wavefunction is formed. It only requires that the photoelectron will not further interact with the system left behind. As will be shown in Chapter 5, indeed, spin-resolved DFT calculations do lead to results that are similar to the experiment, within the limit of this "phase approximation", in addition to the sudden approximation itself.

### 3.1.3 Angle-resolved photoemission spectroscopy (ARPES)

As can be seen in Eqs. (3.1)-(3.4), in order to obtain the dispersion relationship  $E_b(\mathbf{k})$  one has to measure the kinetic energy  $E_k$  of the photoemitted electrons and their emission angles  $\theta_p$  and  $\theta_t$ . The most common energy analyzer used in photoemission is the so-called hemispherical electron analyzer (HEA). It is made of two concentric hemispherical electrodes, held at different voltages, in such a way to allow only the electrons arriving normal to the entrance slit with a certain energy, known as pass energy, to perform a circular trajectory until the end of the analyzer, where they can be detected.

Modern analyzer have the possibility of measuring different kinetic energies in parallel along the vertical direction of the exit slit, combined with an angular acceptance that directly images in the horizontal direction the different angles  $\theta_p$ . However, it is more pedagogical to consider the older version of HEAs, where each angle and energy have to be measured in series. This is the case of the COPHEE endstation presented below.

In Fig. 3.4 an example of a bandmap being measured at COPHEE is shown. The sample manipulator is rotated at angles  $\alpha$ ,  $\theta_t$  and  $\theta_p$ , where photoemission intensities are measured for different kinetic energies of the photoelectrons, corresponding to different binding energies. Then the angle  $\theta_p$  is moved, and the set of  $E_k$  is measured again, thus allowing to determine the relationship  $E_b(k_x)$ . This sequential way of measurement is particularly relevant when considering also the spin, as described in Section 3.2.1: for each ensemble of electrons of given  $E_b$  and  $\mathbf{k}$ , all the three components of spin polarization can be obtained.

Throughout the Thesis, the following names will be used for the different kind of measurements that can be performed while recording the photoemission intensity (and spin polarization if spin-resolved): "momentum distribution curve" (MDC) and "energy distribution curve" (EDC) when the intensity is measured as a function of momentum  $k_x$  or  $k_y$  at fixed kinetic energy  $E_k$  and as a function of  $E_k$  at fixed momentum, respectively; "bandmap" when the energy-momentum dispersion relationship is measured; "constant energy map" (CEM) when the two directions of reciprocal space  $(k_x, k_y)$  are mapped at a fixed kinetic energy (the "Fermi surface" corresponds to the CEM measured at  $E_k$  corresponding to the Fermi level).



### 3.2. Spin- and angle-resolved photoemission spectroscopy (SARPES)

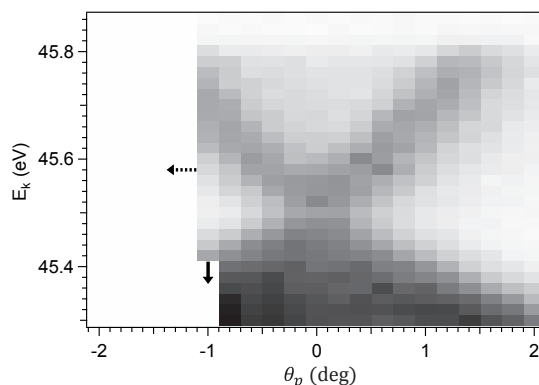


Figure 3.4: An example of a bandmap measured at COPHEE on  $\text{Bi}_2\text{Se}_3$ . At a given  $h\nu$  and angles  $\alpha$  and  $\theta_t$  ( $h\nu = 50$  eV,  $\alpha$  and  $\theta_t$  such that  $\theta_p$  scans along the  $\bar{\Gamma}\bar{K}$  direction), different  $E_k$  are measured for various  $\theta_p$ .

#### The SIS beamline at the Swiss Light Source and the COPHEE endstation

The experiments discussed in Chapters 5-6 were performed at the Complete PHotoemission Experiment (COPHEE) endstation [102], which is installed at the Surface and Interface Spectroscopy (SIS) beamline of the Swiss Light Source (SLS), at the Paul Scherrer Institut (PSI). A typical operation mode of the SLS ring has  $\approx 2$  ns pulse rate, with  $\approx 50$  ps pulse length, which can be considered as a continuous wave in the attosecond regime. The electromagnetic elliptical undulator UE212/424 installed at SIS provides circularly polarized light ( $\zeta^+$  and  $\zeta^-$ ) and linearly polarized light ( $\pi$  and  $\sigma$ , also called horizontal and vertical, respectively) in the range of 20 eV to 800 eV.

At the COPHEE endstation, the angle between the incident light and the outgoing photoelectrons is fixed at  $45^\circ$ , as shown in Fig. 3.6(e). The HEA is an Omicron EA125 with three channeltron detectors. The detection of the spin will be described in Section 3.2.1. At the sample position, the spot size of the synchrotron radiation beam is  $\approx 150$   $\mu\text{m}$ . As for the sample environment, a base pressure  $< 10^{-10}$  mbar guarantees UHV conditions, in a temperature range between 20 K and room temperature. A six axes manipulator allows for full sample alignment, providing three translational and three angular degrees of freedom. In particular, the rotation of the angles  $\theta_p$ ,  $\theta_t$  and  $\alpha$  shown in Fig. 3.6(e) allows to access different points  $(k_x, k_y)$  in the reciprocal space. Sample preparation techniques include cleaving with a top post glued onto the surface, sputtering and annealing, evaporation, or *in situ* pulsed laser deposition (PLD). The surface quality and orientation can be checked by Low Energy Electron Diffraction (LEED).

### 3.2 Spin- and angle-resolved photoemission spectroscopy (SARPES)

In photoemission spectroscopy, once the momentum and the energy of a photoelectron beam have been selected, it is possible to measure its spin polarization vector [Eq. (2.4)], in order

to access all the electron's quantum numbers (momentum, energy, spin). Such technique is known as spin- and angle-resolved photoemission spectroscopy (SARPES) [103]. The filtering of spin is often said not to be achievable with a classical Stern-Gerlach setup [68] because of the combination of Heisenberg uncertainty and Lorentz force [62]. Recently though, it has been shown that by making a fully quantum description of the experiment it should actually be possible to separate an electron beam into spin-up and spin-down components, even if such proposal is experimentally very challenging [104]. Still there are other ways of measuring the polarization of an electron beam, which all rely on electron scattering processes (see Ref. [105] for a recent review). For example, ferromagnetic exchange or spin-orbit interaction can provide the spin filtering capabilities by using magnetic [106–108] or non-magnetic [109–112] targets, respectively. The first approach is known as very low-energy electron diffraction (VLEED), the second one as spin-polarized low-energy electron diffraction (SPLEED), or in a modern way as spin-polarizing mirror.

Another spin-filtering technique relying on spin-orbit interaction is the *Mott polarimeter*, which is based on Mott scattering of high energy electrons (see Section 2.3.2). Despite its great drawback of having an intrinsically low figure of merit and therefore being extremely time consuming, it is still a reliable choice for quantitative spin analysis, since it does not rely on sequential measurements (where some parameter is changed, such as magnetization of the magnetic target, or target orientation, or incident energy) in order to probe the different spin channels of a certain spin quantization axis. Whereas a new proposal of parallel detection of electrons with different momenta and energies in a Mott polarimeter exists [113], the single channel classical Mott polarimeter, which has been used for the experiments presented in this Thesis, will be described in the following.

#### 3.2.1 3D Mott polarimeter at the COPHEE endstation

In Section 2.3.2, it has been shown how only the transverse component  $P_t$  of the spin polarization  $\mathbf{P}$  plays a role in (2.28) for the differential cross-section  $\sigma$  of the electron scattering process. It is now more useful to rewrite it as

$$\sigma(\theta_M, \phi_M) = (|f|^2 + |g|^2) [1 - P_t S(\theta_M) \sin \phi_M], \quad (3.14)$$

so that the asymmetry of the number of electrons  $N$  scattered towards two different azimuthal positions  $a$  and  $b$  identified by the angles  $\phi_{M_a}$  and  $\phi_{M_b}$  is given by

$$A^i = \frac{N_b - N_a}{N_b + N_a} = \frac{\sigma_b - \sigma_a}{\sigma_b + \sigma_a} = P_t^i S \sin \phi_{M_a}, \quad (3.15)$$

where it has been chosen  $\phi_{M_b} = 2\pi - \phi_{M_a}$ . The spatial direction  $i$  depends on the particular choice of  $a$  and  $b$ . From Eq. (3.15) it follows that by measuring  $A^i$  it is possible to obtain  $P_t^i$ .

A Mott polarimeter consists of a heavy element target (usually a gold foil) onto which a high energy (several decades of keV) electron beam is sent perpendicularly. Two detectors placed

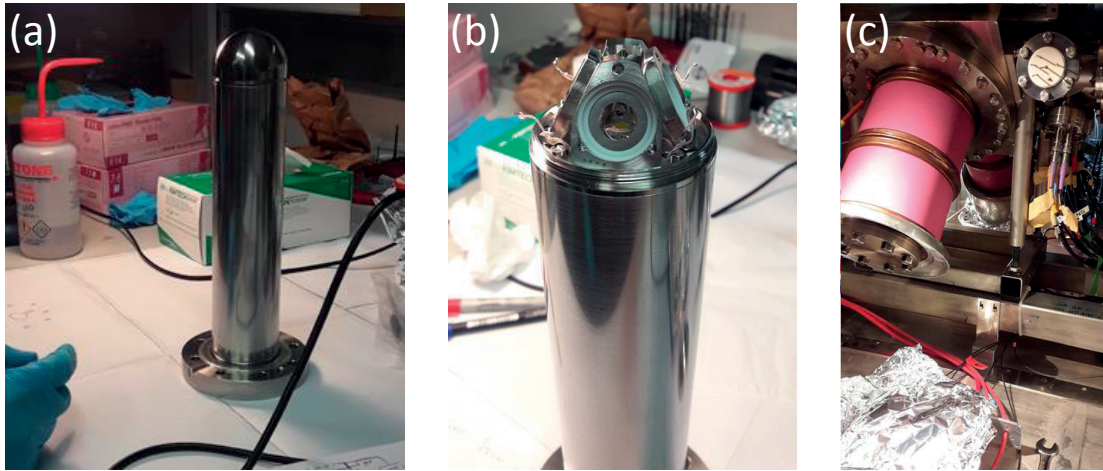


Figure 3.5: Pictures of one of the classical Mott polarimeter installed at the COPHEE endstation (see text for description).

around the target at azimuthal directions  $a$  and  $b$  will count the electrons that are scattered in the two directions, and by combining more detectors one can obtain the spin polarization components in the target plane of the electron beam [79, 114, 115]. Whereas in the so-called classical Mott polarimeter the elastically scattered electrons freely travel towards the detectors at high energy, in the commercially available retarding Mott polarimeter (Mini-Mott) the scattered electrons are decelerated at low energy before they reach the detectors. In Fig. 3.5(a) a picture of one of the classical Mott polarimeters installed at the COPHEE endstation is shown. The whole cylinder goes in UHV, but of its inside only the top part is in UHV. A small aperture in the top allows the electron beam to enter the polarimeter. In Fig. 3.5(b) the top shield is removed, and the gold foil target can be seen, whereas four detectors will be mounted in the four holes around the target.

#### COPHEE

The Complete PHotoemission Experiment (COPHEE) at the Swiss Light Source allows to measure all the quantum numbers of the photoelectrons [102]. It is equipped with two classical Mott polarimeters that operate at  $E_k = 40$  keV and  $\theta_M = 118^\circ$  (back scattering) [79, 114, 115]. The electrons are alternatively sent (with switching frequency of 1 Hz) into the two polarimeters [called  $L$  and  $R$ , one is shown in Fig. 3.5], which are mounted at  $90^\circ$  as shown in Fig. 3.6(a). This allows to measure together all the three spatial components of  $\mathbf{P}$  of the electron beam ensemble of known energy and momentum. In fact, since one Mott polarimeter can give information only about the spin polarization in the plane of the scattering target, the use of a second polarimeter allows to access also the third spatial component. The pink ceramics in Fig. 3.5(c) encases one of the polarimeters and provides electrical isolation. In the back of the picture, the second ceramics for the other polarimeter mounted at  $90^\circ$  can be seen.



### 3.2. Spin- and angle-resolved photoemission spectroscopy (SARPES)

Even if the 8 diodes scheme is the most straightforward and most commonly used, it is not the only choice. First of all, the asymmetry for the  $z_M$  component is clearly redundant, as shown in Eq. (3.20), since it is measured in both  $L$  and  $R$  polarimeters. Whereas in practice  $A_z$  is recorded as the average of the two separate measurements, in principle it is possible to consider only the **6 diodes scheme** as the standard of three-dimensional spin polarization measurements. However, there is one more redundancy which is much less obvious and which is not explicitly described in the literature. This leads to the **5 diodes scheme** described in the following, where as an example the detector  $L_4$  is considered to be the redundant one. By taking  $\phi_{M_a} = 45^\circ$ , it is possible to keep the fixed positions of the diodes  $L_1, L_2, L_3$  and define two new axis  $y'_M$  and  $z'_M$  as shown in Fig. 3.6(c). Now the asymmetry equations are the following:

$$A_{y'_M}^L = \frac{L_3 - L_2}{L_3 + L_2} = P_{y'_M} S \frac{1}{\sqrt{2}}, \quad (3.21)$$

$$A_{z'_M}^L = \frac{L_2 - L_1}{L_2 + L_1} = P_{z'_M} S \frac{1}{\sqrt{2}}, \quad (3.22)$$

where the last term is obtained from Eq. (3.15). By combining Eq. (3.15),(3.17),(3.21),(3.22) and by considering that  $\hat{y}_M = \frac{1}{\sqrt{2}}(\hat{y}'_M - \hat{z}'_M)$  one can write

$$P_{y_M} = \frac{1}{S} A_{y_M} = \frac{1}{S} \frac{L_4 - L_2}{L_4 + L_2} = \frac{1}{\sqrt{2}} (P_{y'_M} - P_{z'_M}) = \frac{1}{\sqrt{2}} \frac{\sqrt{2}}{S} \left( \frac{L_3 - L_2}{L_3 + L_2} - \frac{L_2 - L_1}{L_2 + L_1} \right) \quad (3.23)$$

$$\implies \frac{L_4 - L_2}{L_4 + L_2} = \frac{L_3 - L_2}{L_3 + L_2} - \frac{L_2 - L_1}{L_2 + L_1}. \quad (3.24)$$

By solving Eq. (3.24) with respect to  $L_4$  one thus obtains

$$L_4 = L_2 \frac{L_1 L_2 - L_2 L_2 + 3 L_1 L_3 + L_2 L_3}{L_1 L_2 + 3 L_2 L_2 - L_1 L_3 + L_2 L_3}. \quad (3.25)$$

Therefore Eqs. (3.16)-(3.19) can be used, where  $L_4$  is not the measured one but is obtained from Eq. (3.25).

A similar calculation can be done for all the other diodes, depending on which one is chosen to be the redundant one. This trick can be very useful in practice in the case of one of the diodes being damaged. Also, this allows for different designs: for example, only three diodes placed at  $120^\circ$  from each other in each polarimeter. One could think of reducing one more diode, by using 3 diodes in the  $L$  polarimeter and only 1 in the  $R$  polarimeter, considering the fact that  $A_{z_M}^R = A_{z_M}^L$ . This however does not work, since the corresponding equation to Eq. (3.25) for  $R_4$  would require the knowledge of  $R_1$  and  $R_3$  independently, and not only of  $A_{z_M}^R$ . It is also very interesting to point out that the redundancy described by Eq. (3.25) can be exploited, in principle, to better cancel possible instrumental asymmetries and to reduce the noise of the spin signal in the classical 8 diodes scheme. In fact, each asymmetry can be measured not only from a couple of opposite detectors, but also from four sets of three detectors considered separately, all averaged together.

Finally, in order to understand the experimental results, the Mott coordinate frame is not very helpful. This one is shown in Fig. 3.6(d) with respect to the sample surface normal  $\mathbf{s}$ . It is more useful to rotate the vector  $\mathbf{P}$  in the sample coordinate frame  $(x, y, z)$  shown in Fig. 3.6(e) (to be noticed that they are both left-handed), thanks to a rotation matrix that takes into account the angles  $\theta_p$  and  $\theta_t$ . The transformation is given by

$$\begin{pmatrix} x \\ y \\ z \end{pmatrix} = \frac{1}{\sqrt{2}} \begin{pmatrix} +\cos\theta_p & -\cos\theta_p & -\sqrt{2}\sin\theta_p \\ +\cos\theta_t - \sin\theta_p \sin\theta_t & +\cos\theta_t + \sin\theta_p \sin\theta_t & -\sqrt{2}\cos\theta_p \sin\theta_t \\ +\sin\theta_p \cos\theta_t + \sin\theta_t & -\sin\theta_p \cos\theta_t + \sin\theta_t & +\sqrt{2}\cos\theta_p \cos\theta_t \end{pmatrix} \begin{pmatrix} x_M \\ y_M \\ z_M \end{pmatrix}. \quad (3.26)$$

### 3.3 Spin polarization in photoemission

Certain classes of materials have some electronic states where the electrons have a preferential spin orientation. These states are said to be spin-polarized in the sense of Eq. (2.4). A typical example are the classical ferromagnets such as Fe, Co and Ni, where the magnetism is due to their  $3d$  electrons. The exchange interaction causes an energy shift of these electrons with a sign that depends on their spin, whether it is up or down along the magnetization direction. In an angle-integrated picture, since both sub-bands are populated up to the Fermi level, the imbalance of the electronic occupation will cause the electrons when being photoemitted to have a spin polarization that will depend on the incident photon energy [116, 117]. Another example are materials where spin-orbit interaction plays a role in the definition of the electronic structure. In Rashba materials, the breaking of the inversion symmetry at the crystal surface causes the lifting of Kramers degeneracy, thus resulting in the splitting of spin-polarized surface states [103, 118, 119]. In topological insulators, the topological inequivalence of their bulk band structure with the surroundings guarantees the existence of metallic surface states in the insulating band gap that is opened because of spin-orbit coupling. These so-called topological surface states are spin-polarized because Kramers degeneracy is lifted by the spin-orbit coupling term [120, 121].

In order to probe the spin polarization of photoelectrons emitted from materials with spin-polarized initial states, it is natural to employ the SARPES technique described in the previous Section. It is however very important to keep in mind that photoemission probes the spectral function, as seen in Eq. (3.12), where the dipole transition from the initial to the final state takes place. It is therefore not correct to assume that the measured spin polarization is the one of the initial state, but modification of it can occur during the photoemission process. For example, matrix element effects can change or even reverse the direction of  $\mathbf{P}$  as a function of photon energy or light polarization [122–124]; the diffraction through the surface can be spin-dependent, thus modifying  $\mathbf{P}$  [125]; the coherent excitation of different spin states can result in spin interference effects [126]. All these possibilities make SARPES results difficult to interpret not only on a quantitative level, because of the requirement of sequential measurements with faster detectors or because of the required sample stability with the time consuming Mott



polarimeter, but also on a qualitative level. Nevertheless, the information that can be extracted is highly valuable once such effects are properly considered.

On top of this, there is another subtle effect that becomes an additional correction to  $\mathbf{P}$ , and which has recently not been taken into account very often, despite being known since three decades [56, 62–64, 127–129]: the fact that photoemission can be described as a spin-dependent "**half-scattering**" process. In Eq. (2.29) it has been shown that the scattering of an unpolarized electron beam leads to a polarized beam depending on the scattering direction. Analogously, a spin polarized photoelectron beam is obtained even in the case when a *spin-degenerate initial state* is being probed in photoemission [67]. This case will be described in the following, while in Section 4.6 it will be outlined how to extend this to the case of spin-polarized initial states.

#### 3.3.1 Spin-degenerate initial states: atomic photoionization

In 1969 Ugo Fano recognized that the photoionization of alkali atoms by means of circularly polarized light leads to the emission of electrons that are spin polarized, even when integrated in angle [130]. This is known as the *Fano effect*, and relies on the spin-orbit splitting of the atomic levels and on the selection rule  $\Delta m_j = +1$  ( $\Delta m_j = -1$ ) for  $\zeta^+$  ( $\zeta^-$ ) light polarization. The calculations are rather long, and can be found explicitly in Ref. [62]. In the following they will only be summarized. The initial state  $|m_s, m_\ell\rangle = |\frac{1}{2}, 0\rangle$  of the alkali atom will be excited into  $|\frac{1}{2}, 1\rangle$ , whereas  $|\frac{1}{2}, 0\rangle$  will be excited into a superposition of  $|\frac{1}{2}, 0\rangle$  and  $|\frac{1}{2}, 1\rangle$  weighted by the Clebsch-Gordan coefficients. Thus one can calculate the matrix elements of the transitions: they will depend on the angular parts of the wavefunction, which are spherical harmonics, and on the radial parts. In particular it is useful in this context to define the quantities  $R_{1/2}$  and  $R_{3/2}$ , which are the dipole matrix elements between the radial part of the ground state and the two radial parts of the  $j = 1/2$  and  $j = 3/2$  final states, respectively. One can then construct the density matrix  $\rho$  described in Section 2.2.1. Therefore an expression for the total intensity of photoionization  $I_{tot}$  can be found by using Eq. (2.15), and for the spin polarization  $\bar{\mathbf{P}}$  averaged over all the angles by using Eq. (2.13). One finds  $\bar{P}_x = \bar{P}_y = 0$  and

$$I_{tot} \propto \left[ 1 - \frac{\beta}{2} \mathcal{L}_2(\cos\gamma) \right], \quad (3.27)$$

$$\bar{P}_z = \bar{P}_z(R_{1/2}, R_{3/2}) \neq 0, \quad (3.28)$$

where  $\mathcal{L}_n$  are Legendre polynomials resulting from the integration of spherical harmonics,  $\gamma$  is the angle between photon momentum and electron momentum, and  $\bar{P}_z$  is a rational function of  $R_{1/2}$  and  $R_{3/2}$ . The parameter  $\beta$  is also a function of  $R_{1/2}$  and  $R_{3/2}$ , and is called *dynamical angular asymmetry parameter*. It is interesting to observe that, analogously to the electron scattering process described in Chapter 2, the polarization depends on the cross-section for the production of electrons in the two spin channels.

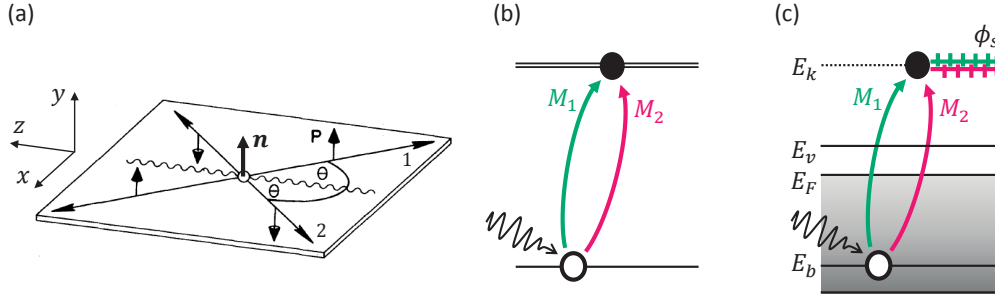


Figure 3.7: (a) Symmetry requirement for the direction of  $\mathbf{P}$  in atomic photoionization (from Ref. [131]). (b) Interference of matrix elements in atomic photoionization for the transition  $\ell \rightarrow \ell \pm 1$ . (c) Two interfering transitions build up the photoemission final state wavefunction, and their phase shift will determine an angular resolved spin polarization.

As shown by Nikolai Cherepkov [127], it is possible to extend these results to the case of unpolarized light or linearly polarized light. By repeating the same kind of calculation for  $\zeta^-$  light polarization and incoherently summing the density matrices for the two cases, one obtains the result for unpolarized light. The interesting result is that, without integrating over all the angles, one does find a spin polarization also in this case, even if there is not a net angular momentum transfer by the incident photon. The result is the following [56, 62, 63]:

$$\mathbf{P} = \frac{2\xi \sin \gamma \cos \gamma}{1 - \frac{\beta}{2} \mathcal{L}_2(\cos \gamma)} \mathbf{n}. \quad (3.29)$$

The denominator is proportional to  $I_{tot}$  [see Eq. (3.27)]. The direction  $\mathbf{n}$  is the perpendicular to the scattering plane defined by the momenta of the incoming photon  $\mathbf{k}_{h\nu}$  and the outgoing electron  $\mathbf{k}$ . It can be understood by the following symmetry argument, in full analogy with a scattering process, similarly to what was discussed with regard to Eq. (2.28) [62]. Given the parity conservation in all the electromagnetic-driven interactions, a system must be equal to itself upon parity inversion  $(x, y, z) \mapsto (-x, -y, -z)$ . Since rotations do not change the chirality, in this case parity inversion can be considered as a mirror inversion  $(x, y, z) \mapsto (x, -y, z)$  followed by a rotation of  $\pi$  around  $y$ . If  $\mathbf{P} \cdot \mathbf{k}$  is positive, then upon reflection it becomes negative. Since one expects a final state not dependent on the experiment coordinate system,  $\mathbf{P} \cdot \mathbf{k}$  must be zero, thus  $\mathbf{P} \perp \mathbf{k}$ . Also, as shown in Fig. 3.7(a), electrons going towards 1 or 2 must have opposite polarization because of axial symmetry. Now, since the magnitude of  $\mathbf{k}_{h\nu}$  is typically negligible, the result has to be the same when rotated by  $\pi$  around  $y$ . Thus  $\mathbf{P} \perp \mathbf{k}_{h\nu}$ .

The term  $\xi$  in Eq. (3.29) is the so-called *spin dynamical parameter* [56]. For completeness, if one would calculate  $\mathbf{P}$  with angular resolution for circularly polarized light, two other parameters will be found (sometimes called  $A$  and  $\gamma$  in the literature [127]), whereas they cancel out for unpolarized light and only  $\xi$  remains. Noticeably, there exist an equation linking  $\beta, \xi, A, \gamma$ , which are therefore not independent [132]. Together with  $\sigma$ , all these values form a set of five



parameters that describe the electron properties in a *complete photoionization experiment* (other two parameters are then required to describe also the residual ion [133, 134]).

In the simpler case of unpolarized light considered here there is only  $\xi$ , and according to Refs. [56, 62, 67, 135] one finds the following result:

$$\xi \propto \text{Im} [M_1 M_2^*] \propto \frac{R_1 R_2 \sin(\phi_2 - \phi_1)}{R_1^2 + R_2^2} = \frac{r \sin \phi_s}{1 + r^2}, \quad (3.30)$$

where  $r$  and  $\phi_s$  are defined as the ratio of the radial part of the two matrix elements  $r = R_2/R_1$  and the difference between the two phase terms  $\phi_s = \phi_2 - \phi_1$ , respectively. The phase shift has the subscript  $s$  since it is at the origin of the spin polarization, not to be confused with the phase term  $\phi$  of Eq. (1.5) (see discussion in Section 4.1). The full explicit expression of  $\xi$  and  $\beta$  can be found in Appendix A. Here  $M_{1,2}$  are the matrix elements describing the transitions to two different degenerate final states, and it is clear how *the spin polarization is a result of the interference between two possible transitions*. This is pictured in Fig. 3.7(b). Following the example of alkali atoms, these two matrix elements are related to transitions towards different  $m_j$  values. However it turns out that in this case the phase difference is very small, thus no appreciable polarization can be measured [62]. On the other hand, one can have different degenerate final states when  $\ell > 0$ , that are the  $\ell + 1$  and  $\ell - 1$  levels. This has been experimentally proved for the first time in Xe atoms [131].

Finally, in a similar way, it is also possible to consider the photoionization by linearly polarized light by coherently summing the two results for  $\zeta^+$  and  $\zeta^-$ . The result is the following [62, 63, 135]:

$$\mathbf{P} = \frac{-4\xi \sin \gamma \cos \gamma}{1 + \beta \mathcal{L}_2(\cos \gamma)} \mathbf{n}. \quad (3.31)$$

In this case, the angle  $\gamma$  is defined between the light polarization vector  $\mathbf{E}$  and the electron momentum  $\mathbf{k}$ , and  $\mathbf{n}$  is the direction perpendicular to the plane defined by these two vectors.

#### 3.3.2 Spin-degenerate initial states: solid state photoemission

The effects seen in atomic photoionization are found also in photoemission from crystals. Angular integrated photoemission by using circularly polarized light, for instance, yields spin polarized electrons when the electronic states involved are influenced by SO coupling, equivalently to the atomic Fano effect. This is, for example, the famous case of the GaAs crystal [136]. Also the use of linearly polarized or unpolarized light can yield spin polarized electrons from spin-degenerate states. As in photoionization, two interfering transitions are required. They can be due to SO coupling in a high symmetry setup [137, 138], or even due to a symmetry breaking in the experiment [65, 128, 139]. In this case in particular, as long as the light impinges on the sample surface with off-normal incidence, the photoelectrons are spin polarized both in the case of normal emission and off-normal emission. An intrinsic

complication is the fact that with off-normal emission further effects such as diffraction through the surface might play a role; but on the other hand it is necessary to probe off-normal emission electrons if dispersive states are being measured, in order to fulfill the energy-momentum dispersion relationship. An interesting complementary approach to the study of spin polarization is the use of spin-resolved *inverse photoemission*, which is the time-reversal process of photoemission where spin polarized electrons are sent on a crystal and UV light is emitted upon deexcitation [140, 141]. The initial state of the inverse photoemission process corresponds to the final state of the photoemission process, and the unoccupied part of the electronic structure of a crystal can be probed. In this case the similarity with a half-scattering process are even clearer, and similar effects to the ones described in this Section have been observed in the unoccupied states [142].

Analogous to the atomic case, one finds that the spin polarization in photoemission from solids is given by the following expression [128, 139, 143]:

$$\mathbf{P} = I_{tot}^{-1}(\Omega) f(\Omega) \text{Im}[M_1 \cdot M_2^*] \mathbf{n} = P(r, \phi_s) \mathbf{n}. \quad (3.32)$$

The term  $\Omega$  is a set that contains all the relevant angles describing the actual photoemission geometry. As usual, the definition of polarization requires the normalization term  $I_{tot}^{-1}$ , which will depend on  $\Omega$ . Also in photoemission from solids, the spin polarization of photoelectrons from spin-degenerate states is given by the interference between (at least) two photoemission channels, described by the matrix elements  $M_1$  and  $M_2$ . In particular, the modulus of the polarization  $P$  depends on the quantities  $r$  and  $\phi_s$ , i.e. the ratio of the radial part of the two matrix elements  $r = R_2/R_1$  and the difference between the two phase terms  $\phi_s = \phi_2 - \phi_1$ . As for the direction  $\mathbf{n}$ , it will not be due only to the direction of  $\mathbf{E}$  and  $\mathbf{k}$ , but it will also depend on the symmetry of the particular crystal and state under consideration. This occurs also for photoionization of molecules, where the direction  $\mathbf{n}$  is influenced by the symmetry of the molecule [144]. Some specific equations have been derived for certain cases in solids [143], but it is more useful here to consider the generic direction  $\mathbf{n}$ , not necessarily known a priori but in principle accessible in an experiment by measuring the three spatial components  $P_{x,y,z}$  [145]. The proportionality constant  $f$  will also depend on the actual crystal and geometry, and it can be seen as a *geometrical correction term* that depends on  $\Omega$  [145] (see Section 4.2).

This interference effect was theoretically demonstrated by Eiiti Tamura and Roland Feder, who showed that a necessary ingredient is the use of a one-step photoemission model [128, 137, 139]. In fact without the translational symmetry breaking at the crystal surface, the three-step model cannot take into account the interference since both initial and final states are Bloch states. If compared to atomic photoionization, however, the matrix elements are not related to different partial waves in the final state, but to the projection of the linear light polarization electric field vector onto the crystal surface, which will have a parallel and a perpendicular component. The reason is that the two components will allow a transition from or to different spatial parts of the double group symmetry representation of the electronic states, which is necessary to introduce when considering the SO coupling [65, 128, 146, 147]. A different point of view is to consider

the different orbital projections that are probed by the different  $E$  field components. At the end, in a more general sense, the expression in Eq. (3.32) can be considered as the result for any situation where two degenerate channels are possible in the experiment, either because of different final states, initial states, or dipole transition channels. For instance, in nonmagnetic crystals with inversion symmetry every state is twofold degenerate [148, 149]. The situation is pictured in Fig. 3.7(c), where the wavefunction of the measured free photoelectron is build up by the interference of two different transitions and has a phase term that is the phase difference between the two matrix elements. In a multiple scattering picture as in KKR calculations, without further developments of the theory, one can still consider as a simplification that the spin polarization comes out of all the possible interference paths as if dependent on a "net" phase shift  $\phi$ <sup>2</sup>. This effect has been studied in the past from the experimental point of view with circular polarized light [147, 150, 151], unpolarized light [152] as well as linearly polarized light [65, 138, 146, 147] on localized states, despite the difficulty of the measurement. It is interesting however to consider the possibility of looking at *dispersive states* in a solid [145], without integrating in energy or angle but maintaining the angular and energy resolution that are typical in ARPES. This will allow to access the phase information via the spin polarization, and to eventually make a link to the time delay in the photoemission process. In Chapter 4 the explicit expression for  $\mathbf{P}$  in the COPHEE setup can be found, and it will be linked to the time information. The following Chapters will report experimental results along these lines.

---

<sup>2</sup> See also the footnote 1 in Section 4.1.



## 4 From spin to time

*“Physics is becoming so unbelievably complex that it is taking longer and longer to train a physicist. It is taking so long, in fact, to train a physicist to the place where he understands the nature of physical problems that he is already too old to solve them.”*

- Eugene Paul Wigner

In this Chapter a semi-quantitative model linking spin polarization and time delay in photoemission from a spin-degenerate dispersive state of a solid will be presented. An outlook at the end will show how to extend this for spin-polarized initial states. The main concept of this Chapter has been introduced in Ref. [145], and many of the details will be submitted for a future publication.

### 4.1 Phase shift as a common term

In Chapter 1 it was shown how a simple description of the Eisenbud-Wigner-Smith (EWS) *scattering time delay* of photoemission is given by  $\tau_{EWS} = \hbar \frac{d\phi}{dE_k}$ , where  $\phi$  is the phase term of the matrix element:  $\phi = \angle \{M_{fi}\}$  [see Eq. (1.5)]. In Chapter 3, on the other hand, it has been discussed how the spin polarization in photoemission from spin-degenerate states arises from an interference process between two different channels<sup>1</sup> of the matrix elements,  $P \propto \text{Im} [M_1 M_2^*](r, \phi_s)$  [see Eq. (3.32)], which depends on the ratio of the radial terms  $r = R_2/R_1$  and the phase shift  $\phi_s = \phi_2 - \phi_1$ .

The two phases  $\phi$  and  $\phi_s$  are closely related. In fact, given the two interfering channels 1 and 2, one has  $M_{fi} = R e^{i\phi} = \langle \psi_f | \hat{H}_{int} | \psi_i \rangle = \langle \psi_f | \hat{H}_{int}^1 + \hat{H}_{int}^2 | \psi_i \rangle = M_1 + M_2 = R_1 e^{i\phi_1} + R_2 e^{i\phi_2}$ , and

---

<sup>1</sup> It is possible that more than two channels are available in the interfering process. It is in principle possible to analytically expand the expression for the spin polarization and the model presented in this Chapter to this more general case, however the expressions would become very heavy. In this Thesis only two channels are considered, and the results can still be applied to a more general case with the simplification of considering two virtual channels that will mimic the actual more complex process.

by making the sum of complex numbers in polar form one obtains <sup>2</sup> :

$$\phi = \phi_1 + \arctan\left(\frac{R_2 \sin(\phi_2 - \phi_1)}{R_1 + R_2 \cos(\phi_2 - \phi_1)}\right) = \arctan\left(\frac{r \sin \phi_s}{1 + r \cos \phi_s}\right), \quad (4.1)$$

where in the last step it has been chosen  $\phi_1 = 0$ , since it is necessary to set a reference given that the two phases  $\phi_{1,2}$  are not absolutely determined (see discussion in Chapter 7). For later, it is useful to notice that  $r > 0$  since the radial terms are positive, and  $\phi$  and  $\phi_s$  are defined within  $[-\frac{\pi}{2}, +\frac{\pi}{2}]$ .

At this point it is interesting to investigate the possibility of accessing the time information by the measurement of the spin polarization. In fact, Eq. (4.1) shows how the measurement of  $\mathbf{P}$  in photoemission can in principle lead, via  $\phi_s$ , to an estimate of  $\phi$ , and therefore of  $\tau_{EWS}$  by varying the kinetic energy of the photoelectron  $E_k$ . In particular:

$$\tau_{EWS} = \hbar \frac{d\phi(r(E_k), \phi_s(E_k))}{dE_k} \approx \hbar \frac{d\phi_s}{dE_k} \cdot \frac{r(r + \cos \phi_s)}{1 + 2r \cos \phi_s + r^2} \doteq \tau_{EWS}^s \cdot w(r, \phi_s), \quad (4.2)$$

where the approximation consists in considering  $\frac{dr}{dE_k} \approx 0$  (see Section 4.4). The EWS *time delay of the interfering channels*  $\tau_{EWS}^s = \hbar \frac{d\phi_s}{dE_k}$  has been introduced, and the rational function  $w = w(r, \phi_s)$  has been defined. The physical meaning of  $\tau_{EWS}^s$  and  $\tau_{EWS}$  will be clearer from the model presented in this Chapter and will be discussed in Chapter 7. Before proceeding with the evaluation of the two EWS time delays from the measured spin polarization, it is useful to write the explicit dependence on  $r$  and  $\phi_s$  of  $P$  in Eq. (3.32), which is done in the following Section.

## 4.2 Spin polarization in solids: geometrical correction

In Eq. (3.32), the geometrical correction term  $f(\Omega)$  depends on the set  $\Omega$  of relevant angles describing the symmetry of the system. As shown in Section 3.3.1, in the case of atomic photoionization the direction  $\mathbf{n}$  of the spin polarization is perpendicular to the *reaction plane* defined by the incident light momentum  $\mathbf{k}_{h\nu}$  and outgoing electron momentum  $\mathbf{k}$  for unpolarized light, and by the light electric field vector  $\mathbf{E}$  and  $\mathbf{k}$  for linearly polarized light. The only relevant angle that determines the spin polarization magnitude in atomic photoionization is the angle  $\gamma$  between the two vectors that define the reaction plane, i.e. the angle between  $\mathbf{E}$  and  $\mathbf{k}$  for linearly polarized light. In the following, only the case of linearly polarized light will be considered. It can be shown [62] that the proportionality coefficient in this case is  $f = 4 \sin \gamma \cos \gamma$ . In the experimental setup of Fig. 3.6(e), for  $\pi$  polarized light the reaction plane is the  $xz$  plane and therefore the direction of  $\mathbf{n}$  corresponds to the  $y$  direction.

---

<sup>2</sup> To be precise, Eq. (4.1) should be written as  $\phi = \phi_1 + \arctan 2 \{R_2 \sin(\phi_2 - \phi_1), R_1 + R_2 \cos(\phi_2 - \phi_1)\}$ , but in this context there will be no difference.

## 4.2. Spin polarization in solids: geometrical correction

As mentioned in Section 3.3.2, in photoemission from solids the reaction plane can vary, depending on the symmetry of the crystal under consideration [128, 139]. For localized states, one would expect a similar behaviour as for atomic levels, but for dispersive states the situation is different because of an intrinsic symmetry reduction. Whereas it should be in principle possible to determine such direction for specific crystals by symmetry arguments, it is however very difficult in practice. A different approach consists in determining the reaction plane *a posteriori*, by considering it as the one perpendicular to the *measured* spin polarization vector. The geometrical correction term becomes  $f = 4 \sin \gamma' \cos \gamma'$ , where  $\gamma'$  is the angle between the projections of  $\mathbf{E}$  and  $\mathbf{k}$  in the reaction plane, and thus depends on the set of relevant angles  $\Omega = (\gamma, \theta, \psi, \delta)$  defined in Fig. 4.1. In the following, the expression for  $f$  will be derived as a function of these angles. The experimental setup of COPHEE shown in Fig. 3.6(e) will be considered (but choosing a right-handed coordinate system, by inverting  $y$ ), in the particular case of  $\pi$  polarized light and MDC measured by varying the angle  $\theta_p$  (the subscript  $p$  will be dropped in this Chapter). Similar equations for  $\theta_t$  as well as for different light polarization directions can be derived along the same lines (as shortly outlined in the discussion of the experimental results presented in Chapter 6).

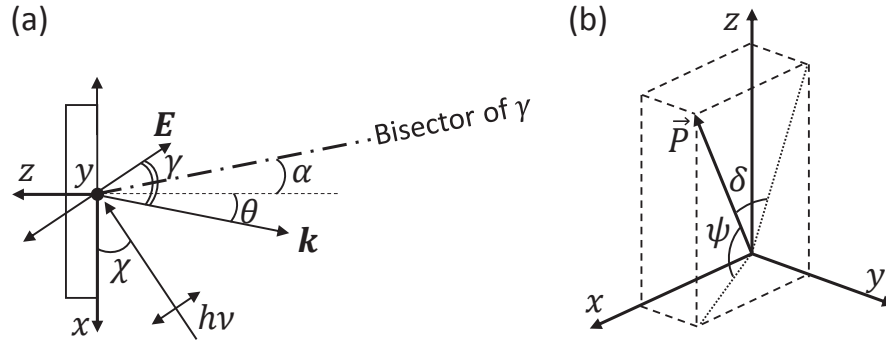


Figure 4.1: Definition of the relevant symmetry angles: (a)  $\gamma, \theta, \alpha, \chi$  and (b)  $\psi, \delta$ . See the text for details.

In Fig. 4.1(a) the angles  $\gamma, \theta, \chi = (\gamma - \theta)$  and  $\alpha = (\gamma/2 - \theta)$  are shown. Since the angle between incident light and outgoing photoelectron is fixed at COPHEE (at  $45^\circ$ ), also  $\gamma$  is fixed ( $\gamma = 45^\circ$ ). Thus, in order to access different points of reciprocal space, the angle  $\theta$  is varied by rotating the sample normal (dotted line). The angles  $\chi$  and  $\theta$  can be used to evaluate the ratios  $E_x/E_z = \tan \chi$  and  $k_x/k_z = \tan \theta$ . In Fig. 4.1(b) the angles  $\psi$  and  $\delta$  are shown. They are the elevation angles of the measured  $\mathbf{P}$  from the  $xy$  and  $yz$  planes, respectively, and thus are always between  $0^\circ$  and  $90^\circ$ . Accordingly, the three components of the spin polarization vector can be written as:  $(P_x, P_y, P_z) = (P \sin \delta, P \sqrt{\cos^2 \delta - \sin^2 \psi}, P \sin \psi)$ . It is important to underline that the deviation of  $\psi$  and  $\delta$  from the atomic case ( $\delta = \psi = 0^\circ$ ) intrinsically depends on the orientation of the crystal planes and the orbital symmetry of the state under consideration, but here they are only considered as the outcome of a measurement.

## Chapter 4. From spin to time

---

It is useful to rewrite the correction term  $f$  in terms of the parameter  $t$  defined as  $t \doteq \tan(\gamma'/2)$ , which is commonly known in trigonometry as parametric Weierstrass substitution. This gives:

$$f(\gamma') = 4 \sin \gamma' \cos \gamma' = 8t \frac{1-t^2}{(1+t^2)^2}. \quad (4.3)$$

Now it is necessary to evaluate the parameter  $t = \tan[\gamma'(\gamma, \alpha, \psi, \delta)/2]$  by trigonometric construction. One obtains

$$t \doteq \tan\left(\frac{\gamma'}{2}\right) = \tan\left(\frac{\gamma}{2}\right) \left( \frac{\cos \psi}{\cos \delta} \cos^2 \alpha + \frac{\cos \delta}{\cos \psi} \sin^2 \alpha \right), \quad (4.4)$$

which can be checked by considering separately the cases where  $\psi$  and  $\delta$  are zero, first with  $\alpha = 0^\circ$  and then varying  $\alpha$ . Now for a given experiment the coefficient  $f$  can be calculated. It has to be pointed out that apart from exceptional cases, the variation of  $f$  with  $\theta$ , which is varied in a measurement, is negligibly small if the  $\theta$  range is small (i.e. a few degrees, as it is for an MDC through a band).

In order to explicitly write  $P = P(r, \phi_s)$ , two more ingredients are needed: the interfering term  $\text{Im}[M_1 M_2^*]$  and an expression for  $I_{tot}$ . The interfering term can be expressed as

$$\text{Im}[M_1 M_2^*] = \text{Im}\left[R_1 R_2 e^{i(\phi_1 - \phi_2)}\right] = R_1 R_2 \sin(\phi_1 - \phi_2) = -R_1 R_2 \sin \phi_s. \quad (4.5)$$

The expression for  $I_{tot}$  as a function of matrix elements can be found in Refs. [128, 139] as

$$I_{tot} = 2R_1^2 \sin^2 \gamma' + 2R_2^2 \cos^2 \gamma', \quad (4.6)$$

which has been modified here with the angle  $\gamma'$  instead of  $\gamma$ , and where the channels 1 and 2 are specified as the two cases of light polarization vector components perpendicular and parallel to the sample surface, respectively. These two components will select different spatial terms of the double group symmetry representation of the state under consideration. Combining Eqs. (4.3)-(4.6), finally Eq. (3.32) can be written as

$$P = \frac{-2 \sin \gamma' \cos \gamma' R_1 R_2 \sin \phi_s}{R_1^2 \sin^2 \gamma' + R_2^2 \cos^2 \gamma'} = \frac{-2 \tan \gamma' r \sin \phi_s}{\tan^2 \gamma' + r^2} = \frac{-4t(1-t^2)r}{4t^2 + r^2(1-t^2)^2} \sin \phi_s \doteq c(r, t) \sin \phi_s, \quad (4.7)$$

where the parametrization  $t = \tan(\gamma'/2)$  and the trigonometric duplication formula  $\tan(\gamma') = \frac{2 \tan(\gamma'/2)}{1 - \tan^2(\gamma'/2)}$  have been used in the second to last step, and the rational function  $c = c(r, t)$  has been defined.

For a fixed value of  $r$  one has  $\max(c) = 1$  for a certain value  $t = t'$ , and  $\min(c) = -1$  for a certain value  $t = t''$ . The measured value of  $t$  depends on the direction  $\mathbf{n}$ , which is described by the angles  $\psi$  and  $\delta$ , dictated by symmetry requirements, and by the angles  $\gamma$  and  $\alpha$ , given by the experimental geometry. At fixed  $\gamma$  and  $\alpha$ , there are several possible combinations of



$\psi$  and  $\delta$  for which  $t = t'$  or  $t = t''$ . The experimental values of  $\psi$  and  $\delta$  for the measurements on Cu(111) presented in Chapter 5, which are the only available precise measurement for the determination of  $t$ , are one of these combinations for which  $t$  and  $r$  (the estimate of  $r$  is presented in the next Section) give  $\max|c| = 1$ . Such coincidence might suggest that the symmetry requirements of the crystal are such that the function  $|c(r, t)|$  [and thus  $P(r, t)$ ] is maximized.

### 4.3 Estimate of time delays

In this Section it will be shown how to estimate the interfering EWS time delay  $\tau_{EWS}^s$  and the scattering time delay  $\tau_{EWS}$  in photoemission from a dispersive state by measuring the spin polarization as a function of binding energy. At the end of the Section, a scheme that summarizes the model can be found.

From Eqs. (4.2) and (4.7), it is clear that knowledge of the parameter  $r$  is required in order to directly estimate  $\tau_{EWS}^s$  and  $\tau_{EWS}$ , even if it has already been considered to be constant with kinetic energy. In fact, since  $P$  depends on both  $r$  and  $\phi_s$ , an independent measurement of  $r$  would be required in order to evaluate  $\phi_s$ . In principle, this should be accessible by UV photoelectron diffraction (UPD), where the angular distribution of photoelectrons is mapped and thus the angular asymmetry parameter  $\beta$  is accessed. Indeed, as mentioned in Section 3.3.1 and shown in Appendix A for atomic photoionization, also  $\beta$  depends on both  $r$  and  $\phi_s$ . This approach however is experimentally very difficult to perform on dispersive states, and for the moment it works sufficiently well only on molecular orbitals [60, 61]. Furthermore, it would be required to combine spin resolution with UPD. Another way to obtain  $r$  would be a careful quantitative analysis of linear dichroism, which however is not often feasible because of difficult control of light intensity for different light polarizations. Therefore one needs to estimate the value of  $r = R_2/R_1$ , and a possibility is  $r = E_{\parallel}/E_z$ , where it is assumed that the weights of the two interfering terms in the state under investigation are the same. Else, if they are known for example from calculations, they could be taken into account to modify the estimate of  $r$ .

Once  $r$  is estimated, it is possible to proceed to calculate the EWS time delays in the following way. The measurement of  $\mathbf{P}$  gives information on both  $P$  and  $\mathbf{n}$ , which determines  $t$ . Now  $c(r, t)$  is given, and from Eq. (4.7) one can calculate  $\phi_s = \arcsin(P/c)$ . In order to vary  $E_k$ , one could think of varying the incident photon energy  $h\nu$ , as it has been routinely done for atomic photoionization [63, 64]. For a dispersive band of a solid, however, this leads to the complication of accessing a different point of the Brillouin zone, since it corresponds to varying the probed  $k_z$ , and it can be an issue when looking at dispersive bands along  $k_z$ . In general, matrix element effects related to cross-section can even lead to strong variations of photoemission intensity with photon energy, thus making it more difficult to draw any *quantitative* conclusion on the spin polarization. Luckily, there is another way of changing the kinetic energy  $E_k$  of the photoelectrons from a dispersive state: by looking at different

## Chapter 4. From spin to time

---

binding energies  $E_b$ . Henceforth a dot will represent the derivative with binding energy:  $\dot{\square} \mapsto \frac{d}{dE_b} = -\frac{d}{dE_k}$ . Under the assumption that  $r$  is a constant with  $E_k$ , any change of  $P(E_b)$  directly corresponds to a change of  $\phi_s(E_k)$ .

At this point one can thus evaluate  $\phi_s$  for various  $E_b$ , and then compute the interfering EWS time delay as  $\tau_{EWS}^s = -\hbar\dot{\phi}_s$ . Now, by using Eq. (4.2), it is possible to compute  $w(r, \phi_s(E_b))$  and finally obtain the scattering EWS time delay  $\tau_{EWS}$ . Noticeably, since  $w$  depends on  $E_b$ , also  $\tau_{EWS}$  will. However, given that the value of  $P$  and its variation with  $E_b$  is expected to be relatively small, such dependence will not be large.

It is insightful to now consider a different approach, where an estimate for a finite lower limit of  $\tau_{EWS}^s$  can be found without relying on the knowledge of the value of  $r$ . Starting from the expression of  $P = P(r, \phi_s)$ , multiplying by  $\hbar$  and applying the chain rule in order to evaluate the derivative with binding energy gives

$$\hbar\dot{P} = \hbar\frac{dP}{dr}\dot{r} + \hbar\frac{dP}{d\phi_s}\dot{\phi}_s, \quad (4.8)$$

where the derivative with respect to the relevant angles  $\Omega$  has been neglected (since the variation of  $f(\theta)$  is negligible in a small  $\theta$  range, as already discussed). Since  $\tau_{EWS}^s = -\hbar\dot{\phi}_s$ , this leads to

$$\tau_{EWS}^s = \frac{-\hbar}{dP/d\phi_s} (\dot{P} - \dot{r}dP/dr) \approx \frac{-\hbar}{dP/d\phi_s} \dot{P}, \quad (4.9)$$

where in the last step the usual approximation  $\dot{r} \approx 0$  has been used (see Section 4.4). The explicit expressions of  $dP/dr$  and  $dP/d\phi_s$  evaluated from Eq. (4.7) can be found in Appendix A. The result of Eq. (4.9) will yield to a similar value of  $\tau_{EWS}^s$  as with the direct method discussed before, by estimating  $r = E_{\parallel}/E_z$  and evaluating  $dP/d\phi_s(r, \phi_s, t)$ . However, in order to only evaluate a lower limit for  $\tau_{EWS}^s$ , one can proceed in the following way. First, the absolute value of both sides of Eq. (4.9) is taken. The signs of  $P$  and  $dP/d\phi_s$  determine the sign of  $\tau_{EWS}^s$ , which in general can be positive or negative, simply meaning a positive or negative delay of the interfering channel 2 with respect to 1. This distinction is however not very interesting, and it is very difficult to make sure that all the possible contributions to signs are properly taken into account, in the formalism as well as in the experiment. It is therefore more useful to look only at absolute values. Then, it is possible to write

$$|\tau_{EWS}^s| = \frac{\hbar}{|dP/d\phi_s|} |\dot{P}| \geq \frac{\hbar}{\max|dP/d\phi_s|} |\dot{P}| = \hbar|\dot{P}| \quad (4.10)$$

since  $|dP/d\phi_s| \leq \max|dP/d\phi_s| = 1$ , where, in particular, the maximum  $|dP/d\phi_s| = 1$  occurs for  $\phi_s = n\pi$  with  $n$  integer and  $|c(r, t)| = \max|c| = 1$  (see the discussion of Eq. (4.7) and the expression of  $dP/d\phi_s$  in Appendix A).

This procedure can be extended to the estimate of a finite lower limit for the scattering EWS time delay  $|\tau_{EWS}|$  from Eq. (4.2) in the following way:

$$|\tau_{EWS}| = |\tau_{EWS}^s| |w(r, \phi_s)| = \frac{\hbar}{|m(r, \phi_s, t)|} |\dot{P}| \geq \frac{\hbar}{\max |m|} |\dot{P}|, \quad (4.11)$$

where  $m \doteq (dP/d\phi_s)/w$ . The explicit expression of  $m(r, \phi_s, t)$  can be found in Appendix A. In this case, though, this function cannot be maximized for every possible value of  $r$  and  $t$ , since  $|m| \rightarrow +\infty$  for  $(r, t) \rightarrow (0, 0)$ , and therefore it is not possible to directly set a *finite* lower limit for  $|\tau_{EWS}|$  from the measurement of  $\dot{P}$ . However, for given values of  $r$  and  $t$  which will be different from 0 ( $r = 0$  in fact means that there is no interfering transitions, and  $t = 0$  is geometrically pathological), it is possible to evaluate  $\max |m(\phi_s)|$  and thus find a finite lower limit for  $|\tau_{EWS}|$ . Also, by estimating  $\phi_s(E_b) = \arcsin [P(E_b)/c]$  from Eq. (4.7) as previously discussed, one can find the actual value of  $|m(E_b)|$ , and therefore estimate  $|\tau_{EWS}(E_b)|$  itself.

It can be useful to consider a way to find also an *upper* limit to the estimates. This is possible by rewriting Eq. (4.7) as

$$\left| \frac{P}{c(r, t)} \right| = |\sin \phi_s| \leq 1. \quad (4.12)$$

This inequality can be used to find the range of allowed possible values of  $r$  for given  $P$  and  $t$  from the measurements, without being limited to the assumption  $r = E_{\parallel}/E_z$ . Therefore one can use these different values of  $r$  in Eqs. (4.10) and (4.11) to find the largest possible values of  $|\tau_{EWS}^s|$  and  $|\tau_{EWS}|$ . These values are the upper limits to the estimate of EWS time delays from the measured values of  $P$  and  $t$  without any assumption on  $r$ .

Noticeably, from Eq. (4.2) it can be seen that the function  $|w|$  is always limited between 0 and 1 for  $\phi_s \in [-\frac{\pi}{2}, +\frac{\pi}{2}]$ , with the curious consequence that  $|\tau_{EWS}| < |\tau_{EWS}^s|$ . This might be counter-intuitive at first; however, as discussed in Chapter 7, the physical interpretation of the two EWS time delays in this Thesis is the following:  $\tau_{EWS}$  is a purely (half-)scattering time delay, whereas  $\tau_{EWS}^s$  accounts for the time delay of the photoemission process. This is because the two interfering partial channels do not correspond to two separate events, but they *together* form the final photoelectron. In addition to this interpretation, it is worth to consider more carefully the allowed range for  $\phi_s$ , as discussed in the following.

### Note on the domain of definition of the phase shifts

Previously, it has been mentioned that  $\phi$  and  $\phi_s$  are defined within  $[-\frac{\pi}{2}, +\frac{\pi}{2}]$ . Whereas this is true for  $\phi$  from Eq. (4.1), there is no univocal choice for  $\phi_s$ , which only has to be in a range of  $\pi$ . If one chooses  $[0, \pi]$ , the function  $|w|$  can have values larger than 1, and therefore it can occur that  $|\tau_{EWS}| > |\tau_{EWS}^s|$ . Also, the estimate of  $\max |m(\phi_s)|$  is not straightforward anymore, since for a given  $r$  and  $t$  there is now a certain  $\phi_s$  for which  $|m|$  still diverges. A further complication involves the estimate of  $\phi_s$  itself from Eq. (4.7), which is not anymore univocal either, since

also the solution  $\phi_s = \pi - \arcsin(P/c)$  becomes possible. It has to be noted, however, that since  $M_{fi} = R_1 + R_2 e^{i\phi_s}$  from Eq. (4.1) the choice of the range  $[-\frac{\pi}{2}, +\frac{\pi}{2}]$  seems more natural, since it allows the two interfering channels to be combined in a way that  $\text{Im}[M_{fi}]$  can be both positive and negative. Whereas this issue deserves further theoretical investigation, it will not be considered anymore in the following for simplicity (apart from the footnote 5 in Section 5.2), and only the range  $[-\frac{\pi}{2}, +\frac{\pi}{2}]$  will be considered.

### Summary of the model for the estimate of time delays

In Fig. 4.2 a summary of the model presented so far can be found. In particular it shows that by measuring the spin polarization modulus (b) and direction (a) as a function of binding energy for a certain dispersive state and with the assumption  $\dot{r} \approx 0$  (k) one can estimate the lower and upper limit of the interfering EWS time delay  $|\tau_{EWS}^s|$ . With the further assumption  $r = E_{\parallel}/E_z$  (l), or knowing  $r$  from calculations or other experiments such as UV photoelectron diffraction, one can then evaluate  $|\tau_{EWS}^s|$  itself. Using Eq. (4.2) also the scattering EWS time delay  $|\tau_{EWS}|$  can be obtained.

## 4.4 Influence of the radial terms on the estimate

In order to find a good estimate of the time delays, in the previous Section it has been discussed how a reasonable choice for the value of  $r$  would be  $r = E_{\parallel}/E_z$ , but other estimates of  $r$  are possible. In Fig. 4.3 the dependence of  $|\tau_{EWS}^s|$  and  $|\tau_{EWS}|$  on  $r$  is shown for a given value of  $\dot{P}$  and for different values of  $t$  and  $\phi_s$ , whereas in Fig. 4.4(a) the values of  $\dot{P}$ ,  $t$  and  $\phi_s$  are the ones found in the experiment on Cu(111) presented in Chapter 5. Since  $\phi_s$  varies with  $E_b$ , the different plots of Fig. 4.3 for different  $\phi_s$  should be considered when the values of  $|\tau_{EWS}^s|$  and  $|\tau_{EWS}|$  are evaluated for different  $E_b$ .

Furthermore, in the previous Section the assumption that the parameter  $r = R_2/R_1$  does not vary with binding energy ( $\dot{r} \approx 0$ ) has been made. In the following, this assumption will be discussed. The ratio  $r = R_2/R_1$  depends both on the geometry, i.e. on the projection of the  $E$  field vector onto the crystal surface, and on the electronic state composition in terms of double group symmetry representation. In order to measure spin-resolved MDCs through a dispersive band at different binding energies, the angle  $\theta$  will be different by only a few degrees within the whole band. Thus, since  $E_{\parallel}/E_z = \tan \chi = \tan(45^\circ - \theta)$ , a small change of  $\theta$  will not sensibly affect  $r$  for different  $E_b$ . As for the state composition, in principle one could have a strong variation of matrix elements within the band under special circumstances, for instance along very low symmetry directions or where states are hybridized with neighbouring bands. However, for a well defined band within a small  $E_b$  range, it is reasonable to assume that its double group symmetry representation does not sensibly vary when the state is considered along a certain high symmetry direction. Experimentally, a good hint to make the assumption  $\dot{r} \approx 0$  is to observe  $\dot{I}_{tot} \approx 0$  [see Eq. (4.6)].

#### 4.4. Influence of the radial terms on the estimate

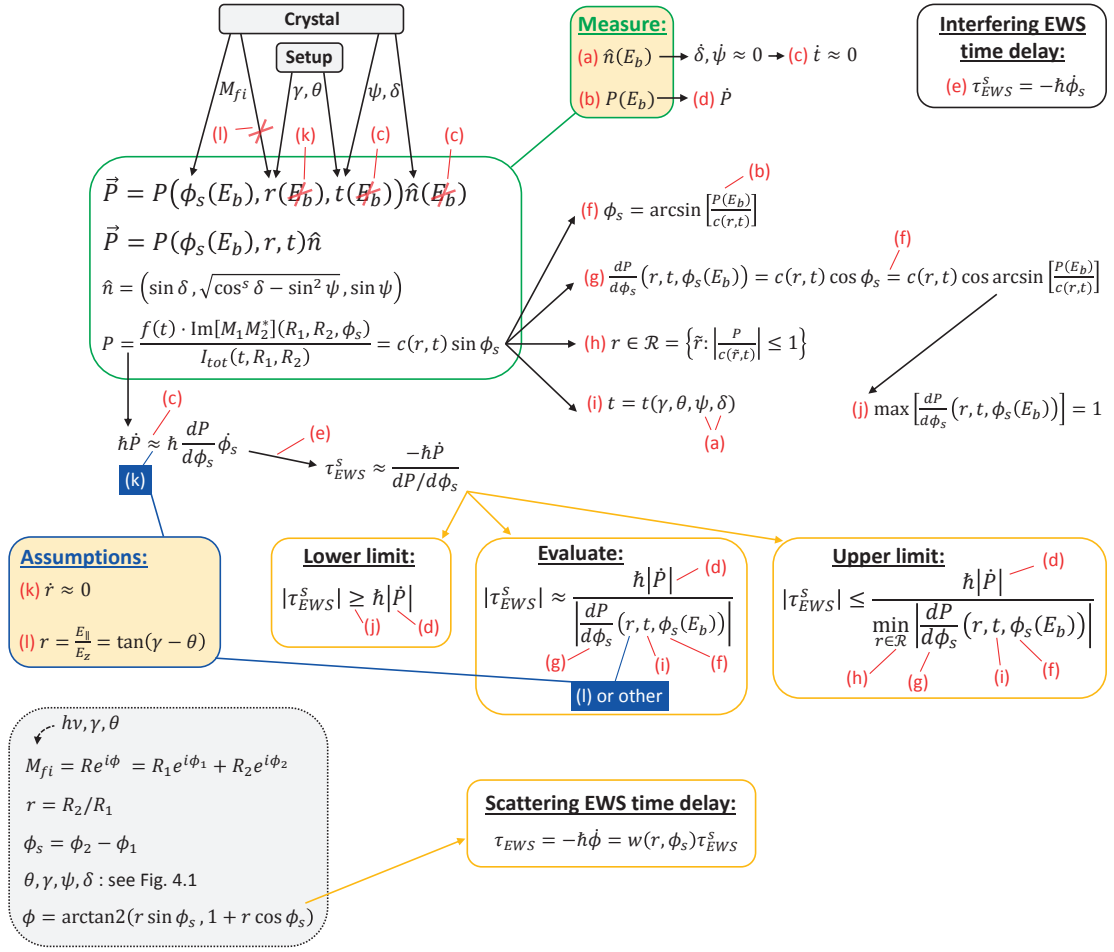


Figure 4.2: Summary scheme of the model used to evaluate EWS time delays in photoemission from the measurement of spin polarization.

On the other hand, it is still possible to consider the more general case where  $\dot{r} \neq 0$ . In such a case, a variation of  $P$  with  $E_b$  is due to a time delay ( $\dot{\phi}_s$ ), but also to a change of matrix elements ratio within the band ( $\dot{r}$ ), as shown by Eq. (4.8). Also, Eq. (4.2) is modified as in the following:

$$\tau_{EWS} = \tau_{EWS}^s \cdot w(r, \phi_s) - \hbar \dot{r} \cdot w'(r, \phi_s) = \frac{-\hbar \dot{P}}{m} + \frac{\hbar \dot{r} (dP/dr - w' m)}{m}, \quad (4.13)$$

where the last step is obtained by inserting the full form of Eq. (4.9). The explicit expression of the function  $w'(r, \phi_s)$  is reported in Appendix A, together with all the other functions presented in this Chapter. In Fig. 4.4(b) the effect of  $\dot{r}$  on the estimate of time delays is shown, where  $|\tau_{EWS}^s|$  and  $|\tau_{EWS}|$  are plotted as a function of  $\dot{r}$  for given values of  $r, \dot{P}, t$  and  $\phi_s$ . Noticeably, in this case there are values for which the time delays are zero, which means that the variation of  $P$  with  $E_b$  is entirely due to variation of the radial part of the matrix elements. The most

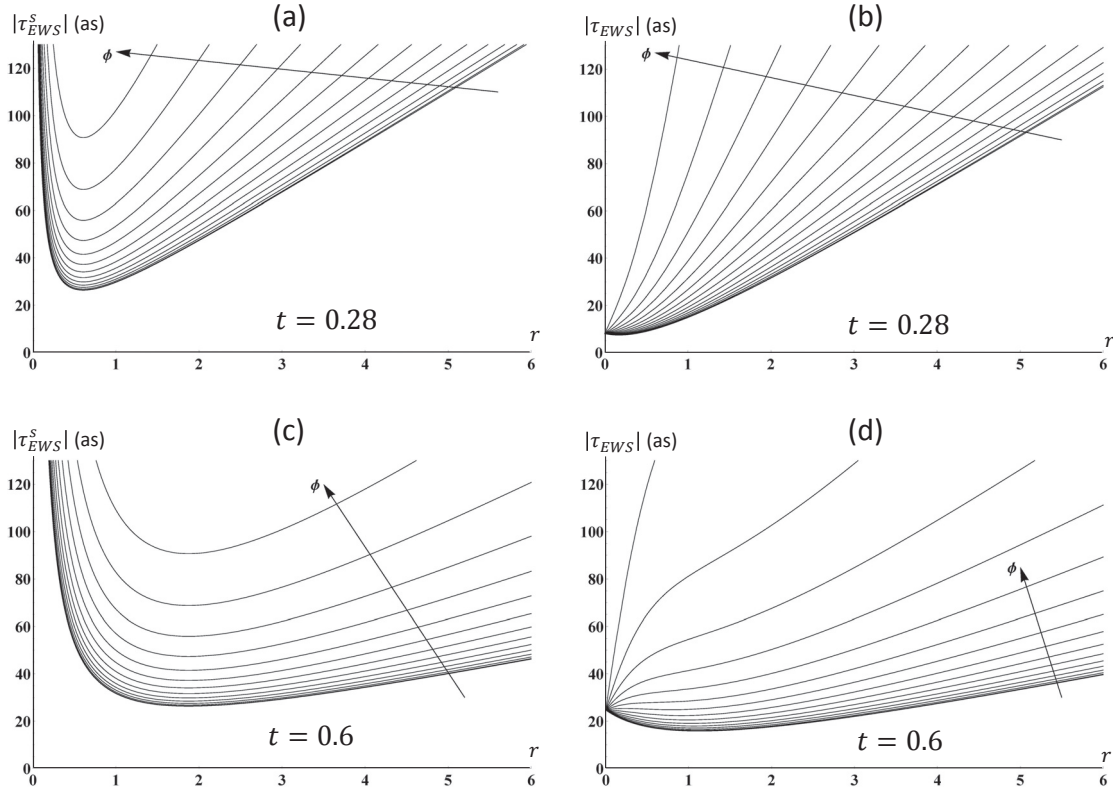


Figure 4.3: Time delays  $|\tau_{EWS}^s|$  [(a), (c)] and  $|\tau_{EWS}|$  [(b), (d)] plotted as a function of  $r$  for two values of  $t$ :  $t = 0.28$  [(a), (b)] and  $t = 0.6$  [(c), (d)]. Every figure shows several plots for different values of  $\phi_s$  ranging from 0 to  $\pi/2$  (same trend for  $\phi_s$  ranging from 0 to  $-\pi/2$ ). The value of  $\dot{P}$  is  $\dot{P} = 0.04 \text{ eV}^{-1}$ .

general situation will correspond to variations in both phase shifts (i.e. time delays) and radial parts. Also, it is important to point out that there exist values of  $\dot{r}$  for which  $|\tau_{EWS}| > |\tau_{EWS}^s|$ .

## 4.5 Spurious effects

In the case of photoemission from solids there might be additional effects other than the interference described in this Chapter that will modify the spin polarization vector. These spurious effects can be due to diffraction through the surface, or to scattering with defects of the crystal during the transport to the surface. The formalism described in this Chapter will be modified in the following way. The spurious effects are modeled by a spin polarization term  $\boldsymbol{\eta}$ , such that the measured spin polarization vector  $\mathbf{P}_m$  is given by  $\mathbf{P}_m = \mathbf{P} + \boldsymbol{\eta}$ , where  $\mathbf{P} = P\mathbf{n}$  is the actual spin polarization given by the interference effects under consideration. The vectorial sum could lead to a rotation of the direction of  $\mathbf{P}_m$  with respect to  $\mathbf{n}$ , thus making it difficult to determine both the relevant quantity  $P$  and the direction  $\mathbf{n}$  itself, which is used to evaluate the parameter  $t$ . In fact, one should now write the two components of  $\mathbf{P}_m$  as  $P_m^n = P + \eta^n$  and  $P_m^p = \eta^p$ , where  $n$  and  $p$  stand for along and perpendicular to  $\mathbf{n}$ , respectively.

## 4.6. The case of a spin polarized initial state

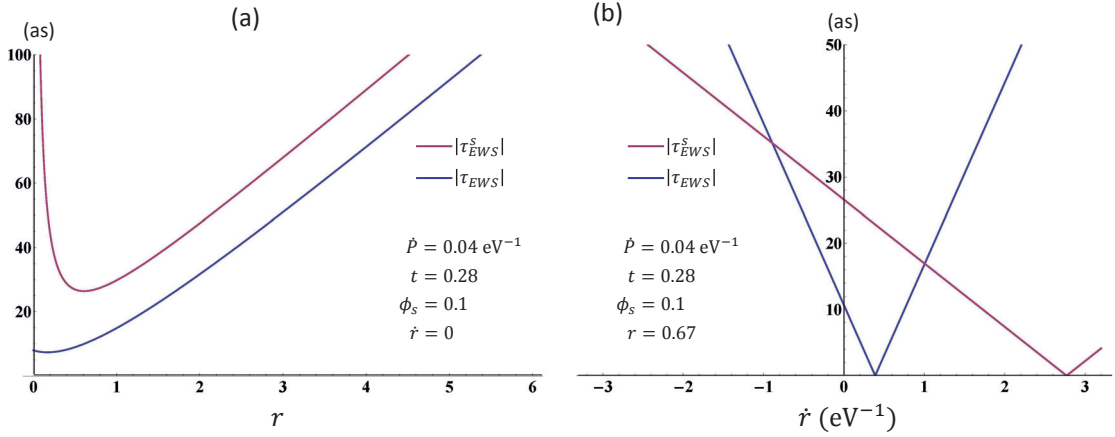


Figure 4.4: (a) Plot of  $|\tau_{EWS}|$  (blue) and  $|\tau_{EWS}^s|$  (red) as a function of  $r$ , for  $\dot{P} = 0.04 \text{ eV}^{-1}$ ,  $t = 0.28$  and  $\phi_s = 0.1$ , where in this case  $\dot{r} = 0$ . (b) Plot of  $|\tau_{EWS}|$  (blue) and  $|\tau_{EWS}^s|$  (red) as a function of  $\dot{r}$ , for  $r = 0.67$  and same values as in (a) for the other parameters [from Eqs. (A.7) and (A.8)].

Clearly, in general the results presented in this Chapter are not valid anymore; however, it is possible to make the following two considerations.

- First, one can at least use Eq. (4.10), where only the derivative of  $P$  with binding energy appears, and consider the fact that spurious effects related to scattering will not strongly depend on kinetic energy. Thus it will be possible to proceed with an estimate of the lower limit of  $|\tau_{EWS}^s|$ .
- Second, diffraction effects will strongly depend on experimental geometry. It is possible to exclude an influence of these effects by measuring the spin polarization from a state of the crystal which is expected not to be dependent on experimental geometry, and showing that there is no variation. This is the case of core levels of the crystal, which will behave as in the case of photoionization of atomic levels [66] so that the spin polarization will not depend on the actual orientation of the crystal with respect to the incoming light. Therefore if this spin polarization does not change when measured with different orientations, it is possible to conclude that the surface does not affect the spin polarization signal with diffraction effects. This situation will be shown for the experiment presented in Chapter 5.

## 4.6 The case of a spin polarized initial state

The results presented in this Chapter until this point concern the spin polarization arising from interfering channels in the matrix elements in the case of a spin-degenerate initial state. The situation is in close analogy with what has been presented in Chapter 2 for electron scattering, where an unpolarized beam of electrons acquires spin polarization because of the interference of the different partial wave components. However, as introduced in Section 3.3,



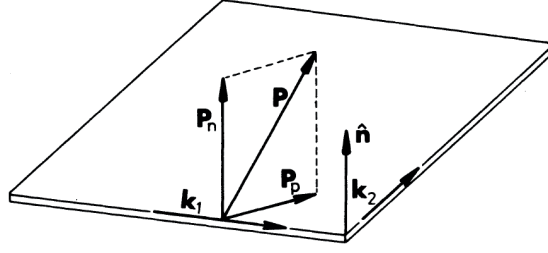


Figure 4.5: Scattering of an electron beam with momentum  $\mathbf{k}_1$  and polarization  $\mathbf{P}$  into a beam with momentum  $\mathbf{k}_2$ . The two momenta define the scattering plane indicated by its normal  $\mathbf{n}$ .

there exist certain classes of materials with an initial state that is already spin-polarized, so that there is a preferential direction in space where the spin of the electrons will point. The question is, how will this spin behave during the photoemission process. There is a number of cases where it has been shown that, indeed, the spin polarization that is measured does not directly reflect the one in the initial state, but it is affected by the particular experimental conditions [124, 153]. This topic is rather complex and not fully covered by a single model, and its review goes beyond the aim of this Thesis. However it is natural to ask how the interference effect previously presented will affect a spin-polarized state, a question which has not been much investigated in the literature.

A proposal to address the issue of spin polarized initial states is the following. Along the lines of the electron scattering picture, one should consider the case of the scattering of a spin-polarized electron beam. It is reasonable to assume that the spin polarization of photoelectrons will be modified in a similar fashion as in the case of scattering. The behaviour of spin-polarized electrons in elastic scattering is well known in literature [62], and a summary without demonstrations is presented in the following.

In Fig. 4.5 the scattering plane defined by the incident and outgoing electron momenta is indicated by the normal vector  $\mathbf{n}$ , and the spin polarization of the incident beam  $\mathbf{P}$  is shown with its two components  $\mathbf{P}_n = P_n \mathbf{n}$  perpendicular to the plane and  $\mathbf{P}_p$  parallel to it. In Eq. 2.29 the spin polarization  $\mathbf{P}'$  of the scattered beam when  $\mathbf{P} = 0$  has been calculated. In the more general case where  $\mathbf{P} \neq 0$ ,  $\mathbf{P}'$  can be calculated in the same way as

$$\mathbf{P}' = \frac{[P_n + S(\theta_M)]\mathbf{n} + T(\theta_M)\mathbf{P}_p + U(\theta_M)(\mathbf{n} \times \mathbf{P}_p)}{1 + P_n S(\theta_M)}, \quad (4.14)$$

where  $S(\theta_M)$  is the Sherman function defined in Eq. (2.24), whereas  $T(\theta_M)$  and  $U(\theta_M)$  are two other functions defined as

$$T(\theta_M) = \frac{|f|^2 - |g|^2}{I_{tot}}, \quad (4.15)$$

$$U(\theta_M) = \frac{fg^* + f^*g}{I_{tot}}. \quad (4.16)$$



#### 4.6. The case of a spin polarized initial state

---

There are several consequences of Eq. (4.14). The component  $P_n$  of the spin polarization vector is modified by a term proportional to  $S$ , while the component  $P_p$  is modified by a term proportional to  $T$ ; also, the spin polarization acquires a new component out of its original plane ( $\mathbf{P}_n, \mathbf{P}_p$ ), and in particular it rotates away from  $\mathbf{P}_p$  by an angle equal to  $\arctan \frac{U}{T}$ . In the particular case of  $\mathbf{P} = 0$ , Eq. (4.14) reduces to  $\mathbf{P}' = S\mathbf{n}$  as already presented in Eq. (2.29).

Therefore, in general, the spin polarization vector rotates and also changes its modulus upon scattering. In two special cases, however, it will only rotate without modifying its modulus: if  $S = 0$ , and if  $P = 1$ . This last case, in particular, is very interesting when considering the analogous case of photoemission as a half-scattering process. It shows that if the photoelectron beam is expected to have a spin polarization  $P = 1$ , as is often the case [154], the interference effect of the different channels in the matrix elements will not modify the modulus of  $\mathbf{P}$ , but it will only rotate its direction from the expected one. Indeed, in a real experiment, the measured spin polarization very rarely points exactly along the direction that is expected from theory, but it is often canted by small angles in different directions depending on the actual experimental geometry. Such observation could be explained by taking into account the interference effect described in this Chapter.



## 5 Results: the model system Cu(111)

*“Not all who wander are lost.”*

*- John Ronald Reuel Tolkien, The Fellowship of the Ring (1954)*

In this Chapter, the model presented in Chapter 4 for the determination of EWS time delays will be applied in a case study, where the spin-degenerate  $sp$  bulk band of Cu(111) has been investigated. The measurement of spin polarization from localized states of Cu(111) will be also shown. The experiment has been performed at the COPHEE endstation (see Section 3.2.1). The main findings have been published in Ref. [145].

### 5.1 Characterization of Cu(111) crystal

Copper (Cu) is a well known material, one of the most used metals both in ancient and modern times. Being an elemental ( $Z = 29$ ) noble metal with  $fcc$  crystal structure, it is a textbook example in the context of photoemission [86, 155], because of its free electron-like dispersion of the bulk band that crosses the Fermi level and thus makes it metallic. Such bulk band originates from the  $4s$  atomic level (Cu electronic configuration:  $[Ar]3d^{10}4s^1$ ), but in the crystal it acquires an  $sp$  character because of hybridization with the fully occupied  $3p$  states. The most common surfaces that have been investigated in photoemission are the (001), (110) and (111) facets [93].

In Fig. 5.1(a) and (b) the 3D Brillouin Zone and the Fermi surface of  $fcc$  copper are shown respectively, and in Fig. 5.1(c) a calculation of the bulk band structure of Cu(111) is reported. The spherical Fermi surface shows the well-known neck distortion at the zone boundaries, and the bulk band structure displays five  $d$  states with small dispersion, together with the parabolic  $sp$  conduction band.

A single crystal of Cu(111) has been measured at COPHEE (see Section 3.2.1). The sample was cleaned by several cycles of Ar sputtering at 1 kV followed by annealing at 400 °C. All the measurements were performed at room temperature. The sample was aligned with the  $\bar{\Gamma}\bar{K}$  direction along  $k_x$  by means of Low Energy Electron Diffraction (LEED) and Fermi surface maps. The quality of the surface is confirmed by the LEED image in Fig. 5.2(a), where the



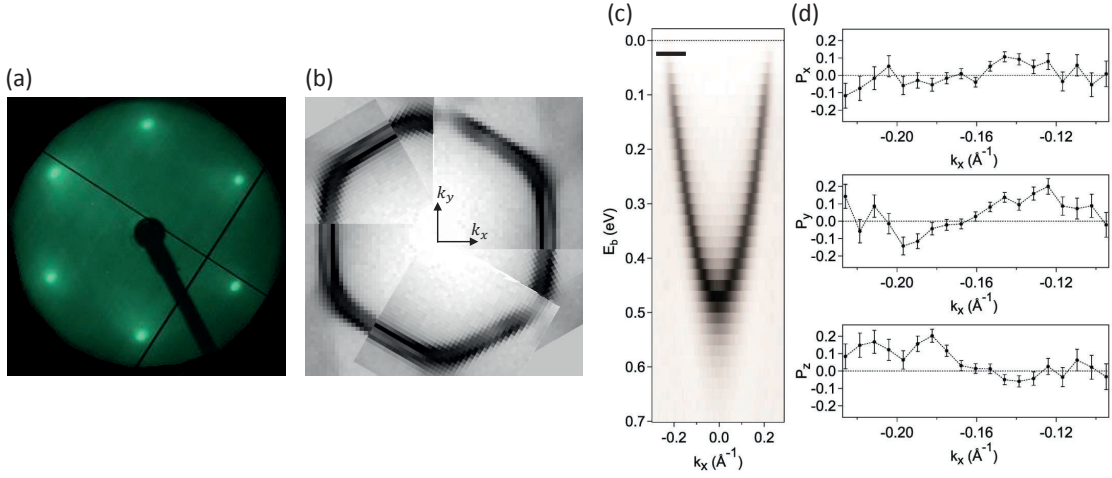


Figure 5.2: (a) LEED image of Cu(111),  $E_k \approx 185$  eV. (b) Fermi surface obtained with  $h\nu = 127$  eV (the measured square portion of Fermi surface has been replicated and rotated several times in order to compose the full image). (c) Bandmap of the surface state of Cu(111) measured with  $h\nu = 21$  eV. (d) 3D spin-resolved MDC of the surface state along the black line in (c), measured with  $\pi$  polarized light of  $h\nu = 21$  eV.

In Fig. 5.3(a) a bandmap measured with  $h\nu = 120$  eV is shown. In this measurement the *d* bulk bands and the *sp* bulk band are visible. In Fig. 5.3(b) a photon energy scan close to the Fermi level is shown. The top and bottom parts of the plot correspond to two different measurements performed for a different photon energy range along the  $k_x$  and  $k_y$  directions, respectively. The surface state, which does not disperse along  $k_z$ , is visible together with the *sp* state. For comparison, in Fig. 5.3(c) a one-step photoemission calculation of the  $h\nu$  scan is shown, where all the features are remarkably well reproduced. The calculations [96] have been performed by Henrieta Volfová and Jan Minár at the Ludwig-Maximilians-Universität of Munich.

## 5.2 EWS time delays from the *sp* bulk band

The *sp* bulk conduction band of Cu(111) has been investigated with spin-resolved ARPES with the purpose to extract the EWS time delays according to the model presented in Chapter 4. In order to maximize the counts of the spin-resolved measurements, optimal photon energies have been chosen from the  $h\nu$  scan in Fig. 5.3(b). Local maxima in intensity were found at 46 eV and 130 eV. A bandmap for  $h\nu = 130$  eV is reported in Fig. 5.4(a), which does not show significant changes of photoemission intensity with binding energy. This observation is a hint that the assumption  $\dot{r} \approx 0$  is reasonable, as discussed in Section 4.4. Solid lines indicate the binding energies where spin-resolved MDCs have been measured by scanning the angle  $\theta_p$  with  $\pi$  linearly polarized light [see Fig. 3.6(e)]. The sequence has been measured in an alternated order, in order to not misinterpret possible sample aging effects. The free-electron-like band under consideration is the only state in a 2 eV range from the Fermi level

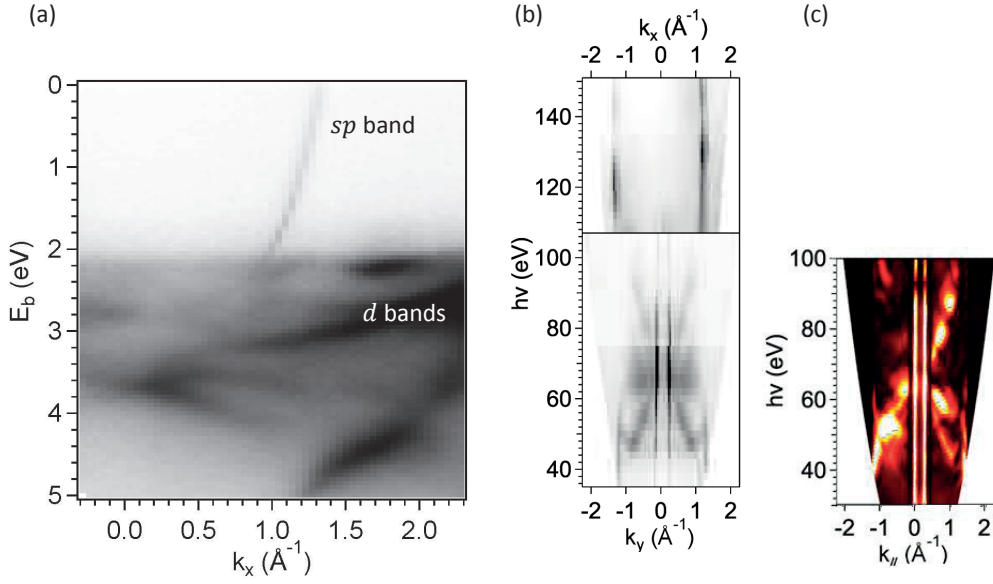


Figure 5.3: (a) Bandmap of Cu(111) measured with  $h\nu = 120$  eV along the  $\overline{\Gamma K}$  direction. (b) Photon energy scan close to the Fermi level, which maps the dispersion along the  $k_z$  direction (the two parts of the plot correspond to two different measurement performed along  $k_x$  and  $k_y$ ). (c) One-step photoemission calculation of the  $h\nu$  scan.

and therefore cannot have any hybridization with other bands. This is important since the presence of other bands would make very difficult to disentangle different contributions to the spin signal. At this photon energy, the angle  $\theta_p$  is varied between  $9.5^\circ$  and  $12.5^\circ$  in order to access the band with angular resolution at the various binding energies. As it has been discussed in Chapter 4, for such a small angular range the variation of the geometrical correction parameter  $f(\theta_p)$  can be neglected. By choosing  $\theta_p = 11^\circ$ , one can then estimate the quantity  $r$  as  $r = E_{\parallel}/E_z = \tan \chi = 0.67$  [see Section 4.3, Fig. 4.1(a) and Fig. 5.6(a)].

In Fig. 5.4(b) the three spatial components  $x$ ,  $y$ ,  $z$  of  $\mathbf{P}$  for the MDC measured 0.2 eV below the Fermi level [i.e. at energy  $E_2$  of Fig. 5.4(a)] are shown, together with the total photoemission intensity. Two main observations can be made:

- First, despite the probed band is a spin-degenerate state, there is a clear spin polarization signal in the  $y$  and  $z$  components, which is generated during the photoemission process. It is possible to exclude possible surface-induced Rashba-like effects<sup>3</sup> in the initial state bulk bands as the main cause for the observed spin polarization from similar measurements on Au(111) ( $Z = 79$ ), shown in Fig. 5.5(a). A spin polarization with similar magnitude and splitting as in Cu(111) (Fig. 5.4(b), reproduced also in Fig. 5.5(b) for

<sup>3</sup> In some materials, where there is no inversion symmetry in the bulk because of their crystal structure, also the bulk states will experience Rashba splitting [158, 159]. This is however not the case of Cu(111), since its  $fcc$  crystal structure is inversion symmetric. Nevertheless, the possibility for a bulk state to be spin split has still been suggested, because of the combined strong influence of the surface on the bulk band structure and the surface sensitivity of photoemission [160].

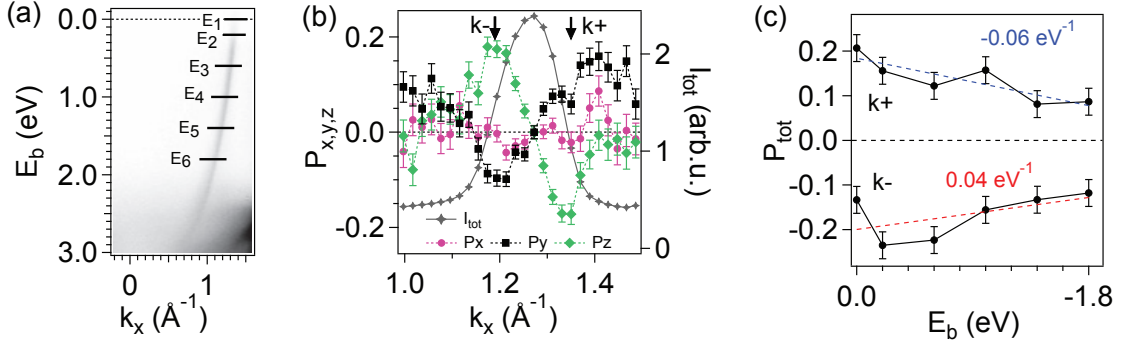


Figure 5.4: (a) Bandmap at  $h\nu = 130$  eV with the *sp* bulk conduction band. Solid lines indicate the  $E_b$  where the spin-resolved MDCs have been measured. The actual set was performed in a random sequence in order to prevent any sample aging artifact. (b) 3D spin-resolved MDC along  $k_x$  measured 0.2 eV below the Fermi level [ $E_2$  in (a)] with  $\pi$  polarized light of  $h\nu = 130$  eV. The total intensity and the three polarization spatial components are shown. (c) Plot of  $P(E_b)$  for the two spin signals  $k^-$  and  $k^+$ .

comparison) is found, whereas for Rashba-like effects one would expect a much larger spin polarization magnitude and splitting in a material with much stronger spin-orbit coupling.

- Second, the spin polarization signal does not correspond to the maximum of the photoemission intensity, as would be expected for atomic levels or localized states [62, 66], but it displays two opposite vectors to the left and to the right of the main peak, indicated as  $k^-$  and  $k^+$  respectively in Fig. 5.4(b). This peculiar feature will be called *double polarization feature* (DPF), and will be analyzed in Section 5.2.1. Here, it can be already mentioned that this is not a measurement artifact for the following reason. In Fig. 5.5(c) a spin-resolved EDC measured with  $h\nu = 203$  eV over the  $3p$  core levels of copper is shown. This measurement has been performed with a photon energy and a geometry such that the kinetic energy and the angle  $\theta_p$  are the same as the measurement of the *sp* band of Fig. 5.5(b). In this case a localized state is probed, and only a single spin polarization vector is observed corresponding to each core level ( $3p_{1/2}$  and  $3p_{3/2}$ ), as expected for atomic-like states [66]. A discussion of the spin-resolved measurement over the  $3p$  core levels can be found in Section 5.3. This argument alone regarding the EDC measurement against possible artifacts is not complete, since one cannot consider the possibility of the DPF occurring only in MDCs, given that the core levels are localized and thus one will not find a peak in an MDC. However, the existence of the DPF is also corroborated by calculations, as presented in Section 5.2.1, and seems to be a general property of dispersive states, since it has also been observed in other systems (see Chapter 6).

As shown in Fig. 5.6(a), the  $E$  field of the light lies in the  $xz$  plane and thus probes both in-plane and out-of-plane orbital components, which in turn are not isotropic in contrast to



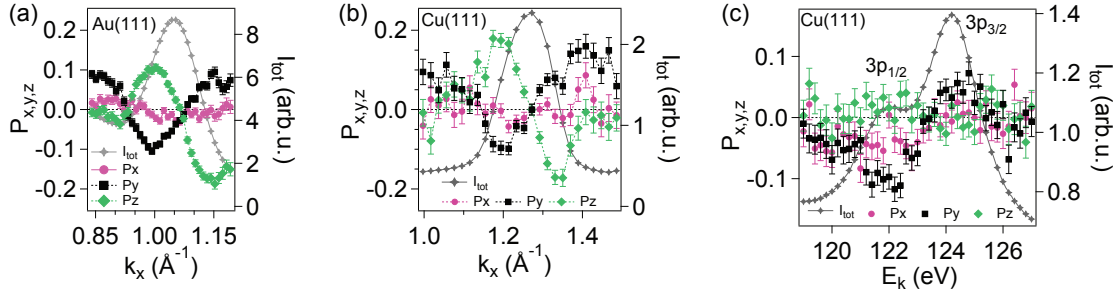


Figure 5.5: (a) Spin-resolved MDC close the Fermi level performed on a Au(111) crystal with  $\pi$  polarized light of  $h\nu = 40$  eV. In this case the direction of  $\mathbf{P}$  is given by  $\delta \approx 0^\circ$  and  $\psi \approx 44^\circ$ . (b) Same figure as in Fig. 5.4(b) reported here for comparison. (c) Spin resolved EDC of the  $3p$  core levels with same  $E_k$  and  $\theta_p$  as the measurement in (b).

the simpler case of atomic targets. Because of these symmetries, combined with the (111) crystal orientation probed with a low-symmetry non-normal incidence setup, the expected direction  $\mathbf{n}$  of the spin polarization will deviate from the purely atomic one, which would correspond to  $y$ . Indeed, the direction of the two spin polarization vectors at  $k^-$  and  $k^+$  is in the  $yz$  plane, as can be extracted from Fig. 5.4(b). In particular, one obtains  $\delta \approx 0^\circ$  and  $\psi \approx 51^\circ$  [angles defined in Fig. 4.1(b)] for the vector corresponding to  $k^-$ , shown in Fig. 5.6(b) together with the corresponding reaction plane, and the opposite direction for the vector at  $k^+$ . A variation of  $\pm 5^\circ$  from these directions is found for the measurements at different  $E_b$ , which is within the experimental accuracy of the COPHEE setup. As discussed in Section 4.2, the reaction plane in the case of photoemission from solids deviates from the case of atomic photoionization (which would be  $xz$  in the given setup) because of the reduced symmetry of a crystal with respect to an isotropic atom. It is difficult to determine this plane *a priori*, but it is interesting to observe that the one found experimentally coincides with the (2,1,0) crystal plane<sup>4</sup>. Further experiments on different facets could shed more light on this point. The measured angles  $\delta$  and  $\psi$  can be used to compute the geometrical correction in the equations from Chapter 4, and in particular one finds  $t = 0.28$  from Eq. (4.4). It has to be noted that this value of  $t$  corresponds to the one for which  $c(r, t) \approx 1$  (and thus  $P$  is maximized) for the previously estimated value of  $r = 0.67$  (see Section 4.2).

From the spin-resolved MDC at the given energy  $E_2$  shown in Fig. 5.4(b) the value of  $P$  at this  $E_b$  is obtained. By repeating other measurements at different  $E_b$ , a plot of  $P(E_b)$  can be constructed, as shown in Fig. 5.4(c) for both peaks  $k^-$  and  $k^+$ . The slope of their linear fit,  $|\dot{P}| \approx 0.04$  eV $^{-1}$  (the smaller value corresponding to  $k^-$  will be considered), is the relevant quantity to determine the EWS time delays. In fact, in Chapter 4 the quantity  $|\dot{P}|$  has been related to both time delays  $\tau_{EWS}^S$  and  $\tau_{EWS}$ , which are associated to the phase shift between the interfering channels and to the phase term of the full matrix element of the transition,

<sup>4</sup> The measured angle between the reaction plane and the (111) facet is  $90^\circ - 51^\circ = 39^\circ$ . The angle between the plane  $(h, k, \ell)$  and the (1, 1, 1) is given by  $\arccos \frac{h+k+\ell}{\sqrt{3}\sqrt{h^2+k^2+\ell^2}}$ . For example, this is equal to  $35.3^\circ$  for the (1, 1, 0) plane and to  $39.2^\circ$  for the (2, 1, 0) plane.



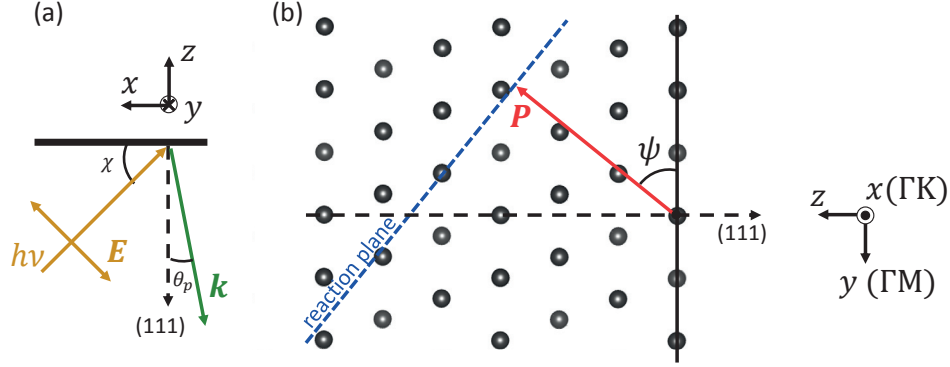


Figure 5.6: (a) Experimental geometry. (b) Orientation in space of the measured  $\mathbf{P}$  at  $k^-$  (the one at  $k^+$  is opposite). The reaction plane is tilted by  $\psi = 51^\circ$  from the atomic reaction plane  $xz$ .

respectively. From Eq. (4.10) one can estimate  $|\tau_{EWS}^s| \geq \hbar |\dot{P}| \approx 26$  as, but also  $|\tau_{EWS}^s| \approx 26$  as from Eq. (4.9) because of the combined optimum of  $r$  and  $t$  yielding  $c \approx 1$ . Similarly, from Eq. (4.11) one obtains  $|\tau_{EWS}| \approx 11$  as.

As shown in Section 4.3, the two Eqs. (4.9) and (4.11) can also be used to find the dependence of the two time delays on binding energy from the dependence of  $\phi_s(P(E_b))$ . However it can be checked that the variation of  $P$  with binding energy leads to a negligible variation with binding energy of both  $|\tau_{EWS}^s|$  and  $|\tau_{EWS}|$ <sup>5</sup>.

If one does not calculate  $r = E_{\parallel}/E_z$  but allows different values for  $r$ , the estimates of the time delays will be different. Then it is possible to set an upper limit as discussed in Section 4.4. From Eq. (4.12) one finds  $r_{max} = 12.1$  by using  $\phi_s = 0.1$  and  $r_{max} = 6$  by using  $\phi_s = 0.2$ . Under the assumption  $\dot{r} \approx 0$  the largest possible value of  $r$  is  $r_{max} = 6$ , which gives  $|\tau_{EWS}^s| \leq 134$  as and  $|\tau_{EWS}^s| \leq 115$  as. It should be mentioned that the estimate of an upper limit for  $|\tau_{EWS}^s|$  as reported in Ref. [145] is not discussed in this Thesis, since the estimate given here is more precise.

The  $P(E_b)$  measurement has been repeated for various photon energies as shown in Fig. 5.7. In addition, the experiment at  $h\nu = 130$  eV has been performed twice in order to test the reproducibility of the measurement. Within the limits of relatively large error bars and a small number of data points, a similar overall slope is observed for all the  $h\nu$ . This suggests that possible additional effects related to the travel time of the electron during the transport to the surface [161, 162] are not of importance, at least within the experimental capabilities (see discussion in Chapter 7).

To conclude this Section, from the measurement of modulus and direction of the spin polarization vector as a function of binding energy for the *sp* bulk band of Cu(111) the two following es-

<sup>5</sup> On the other hand, if one allows  $\phi_s > \pi/2$  (see the discussion on the domain of definition of the phase shifts in Section 4.3) then  $|\tau_{EWS}(E_b)|$  varies between  $\approx 40$  as and  $\approx 50$  as in the probed  $E_b$  range.

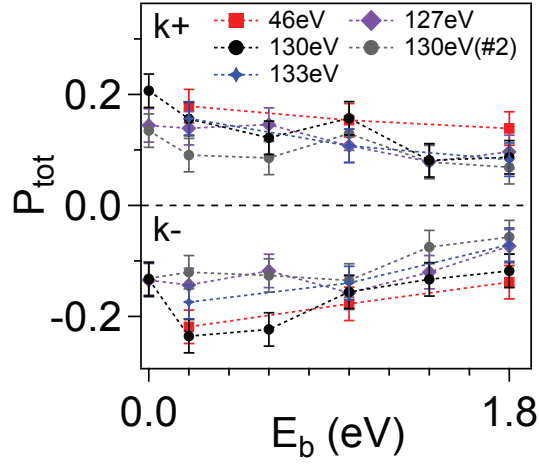


Figure 5.7: Plot of  $P(E_b)$  for the two spin signals  $k^-$  and  $k^+$ , repeated for different  $h\nu$ .

imates of EWS time delays have been found:  $26 \text{ as} \leq |\tau_{EWS}^s| \leq 134 \text{ as}$  and  $11 \text{ as} \leq |\tau_{EWS}| \leq 115 \text{ as}$ . Furthermore, by assuming  $r = E_{\parallel}/E_z$  one finds  $|\tau_{EWS}^s| \approx 26 \text{ as}$  and  $|\tau_{EWS}| \approx 11 \text{ as}$ .

### 5.2.1 DFT calculations and the double polarization feature

In the previous Section, the two EWS time delays  $|\tau_{EWS}^s|$  and  $|\tau_{EWS}|$  have been determined for the  $sp$  bulk band of Cu(111). In particular, they have been obtained from the measurement of the spin polarization  $P$  as a function of binding energy. The experiment has been performed for several photon energies. In Fig. 5.8(a) a summary of  $P$  from all the MDCs performed with  $h\nu = 130 \text{ eV}$  is shown. The red/blue color scale takes into account the sign of  $P$  along the direction  $\mathbf{n}$  obtained from the three spatial components  $P_x, P_y, P_z$ . Crucially, whereas the  $sp$  state displays one single band when probed without spin resolution, as well established in literature [93] and shown in Fig. 5.1(c) and Fig. 5.4(a), when measured with spin resolution it displays an up/down signal called *double polarization feature* (DPF).

In order to understand the DPF, fully relativistic self-consistent multiple-scattering Korringa-Kohn-Rostoker (KKR) density functional theory (DFT) calculations [96] have been performed by Henrieta Volfová and Jan Minár at the Ludwig-Maximilians-Universität of Munich. In Fig. 5.8(b) the evaluated  $P$  from the calculations in the framework of one-step photoemission [95, 97] within its spin-density matrix formulation [98] for a semi-infinite Cu(111) system is shown, and its three spatial components are reported in Fig. 5.8(d). Given the complexity of these spin signals, it is not possible to unambiguously fix a direction along which  $P$  could be projected in order to plot it in a red/blue color scale, and therefore in Fig. 5.8(b) only the modulus of  $P$  is shown. Such complexity could be missing in the experiment due to a lack of resolution, but on the other hand it could also be an overestimate of the DFT calculations, along the lines of the discussion about extrinsic losses and sudden approximation presented in Section 3.1.2. Despite this, still it is clear that the  $sp$  band gives rise to *at least two spin*

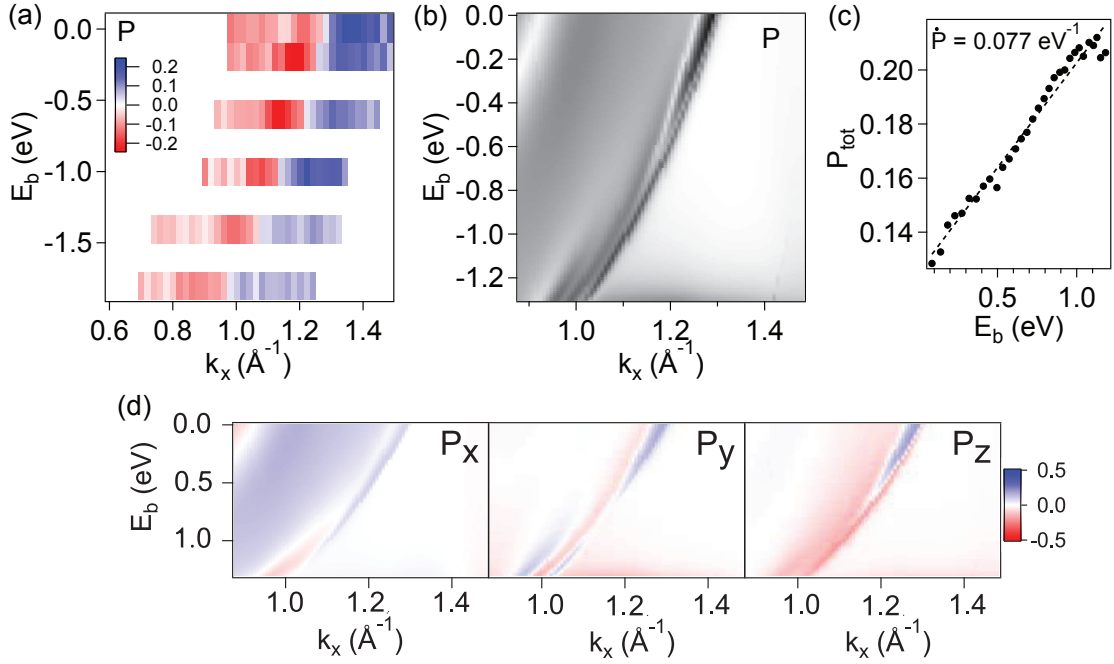


Figure 5.8: (a) Summary of spin polarization  $P$  from MDCs measured along  $k_x$  with  $\pi$  polarized light of  $h\nu = 130 \text{ eV}$  plotted as a bandmap. (b)  $P$  from KKR calculations performed for parameters similar to the experiment. (c) Plot of  $P(E_b)$  for a selected feature of (b). (d) The three calculated spatial components of  $P$ . Their complexity does not permit to unambiguously fix a direction along which  $P$  in (b) could be projected in order to plot it in a red/blue color scale.

*signals*, matching to the experimental results and thus strengthening the interpretation of the DPF as a real feature and not an artifact of the measurement.

The fact that the spin polarization signal is reproduced by the calculations suggests that it is also possible to extract the EWS time delays information from the output of DFT using the same model presented in Chapter 4. In fact, as shown in Fig. 5.8(c), the fit of  $P(E_b)$  for a selected feature has a slope that is relatively close to the value found experimentally. In principle, one could even directly extract the phase terms of the matrix elements from the DFT calculations. Such operation would give valuable information about the system under investigation, but requires important modifications of the available DFT codes [163].

A similar feature to the DPF has already been obtained, but not discussed, in previous calculations from a different group related to the study of self-energy corrections in Cu(111) [164]. In that work, the single feature of the *sp* band calculated without self-energy terms [Fig. 5.9(a)] becomes split into two features when self-energy corrections are included [Fig. 5.9(b)], as indicated by a red circle. This result is remarkably similar to the spin-resolved data of Fig 5.8. However, it is important to note that this calculation is not spin-resolved. Also, this peculiar feature is not even mentioned in Ref. [164], since it does not appear in the (spin-integrated) experimental data reported there. Further investigation of the calculations from Ref. [164]

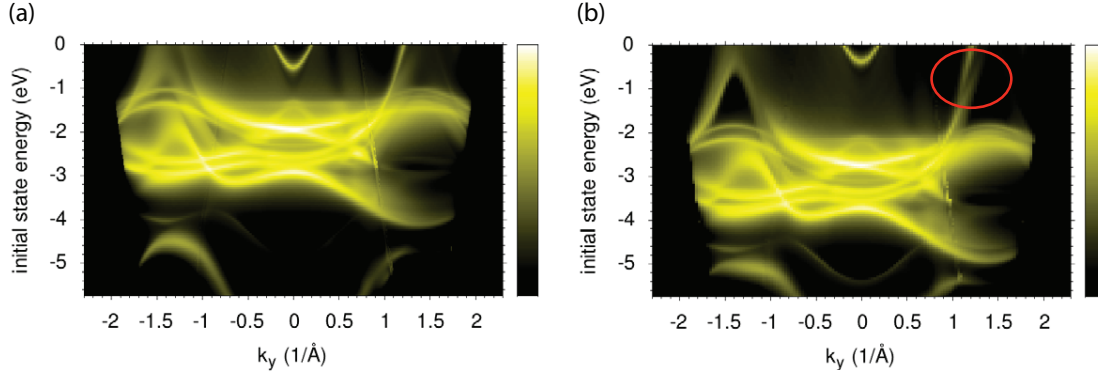


Figure 5.9: Calculated band structure of Cu(111) from Ref. [164] (modified). (a) No self-energy corrections included. (b) Self-energy corrections included, with orbital-dependent shifts of the Local Density Approximation potential  $\Sigma_d = -0.8$  eV and  $\Sigma_{sp} = +0.3$  eV. The red circle indicates the peculiar splitting of the  $sp$  band that is reminiscent of the DPF.

suggests that different contributions to the DPF from the bulk state and the bulk-derived state at the crystal surface might also play a role [165].

As will be presented in Chapter 6, it seems like the DPF is a common feature of dispersive states, since it is found also in a system very different from Cu(111) such as  $\text{Bi}_2\text{Sr}_2\text{CaCu}_2\text{O}_{8+\delta}$ . However it does not appear in localized states (see Section 5.3), in accordance with the atomic photoionization model. It is difficult to investigate the nature of the DPF, because of the lack of a one-step theory of photoemission where these phase-related spin polarization effects are explicitly described and not only a result of the calculation of the matrix elements. In the following, possible ingredients from literature to explain the DPF, in addition to self-energy corrections and surface-related effects, will be highlighted.

In general, the phase term of the final state wavefunction in the one-step model of photoemission goes from 0 to  $\pi$  when passing through an atomic resonance, whereas in solids it becomes a complex quantity with characteristic resonant shape when hole lifetime effects (closely related to self-energy corrections) are included, as explained in Ref. [92]. This suggests that every state inherently provides a phase-shift of  $\pi$  when it is probed in photoemission, and since according to Eq. (4.5)  $P \propto \sin \phi_s$ , it will result in two opposite directions of the spin polarization vector when crossing the state.

As has already been pointed out, it seems that such a  $\pi$  shift occurs only in dispersive states, i.e. when it is possible to look at a state as a function of momentum. The dependence on momentum could be understood by considering the following similar situation from the field of cold atoms. In Ref. [166] it is shown that, thanks to spin-orbit coupling, two cold atoms of different momenta can be coherently combined in a so-called *Feshbach molecule* with the spin of the two atoms antiparallel to each other. In other words, spin-orbit coupling provides a  $\pi$  phase difference to particles with slightly different momenta at the resonant energy of a system. This suggests that, in photoemission, the electrons coming from a dispersive state

that have a finite different momentum because of the intrinsic broadening of the state might experience a phase difference of  $\pi$  in their wavefunction because of the influence of spin-orbit coupling.

The concept of a Feshbach molecule is closely related to the phenomenon of *resonance scattering*, which allows to interpret the DPF from a different perspective, namely as an energy instead of momentum splitting, as explained in the following. This is based on considering once again the similarity of the photoemission process with the one of electron scattering, as in Section 3.3, and is summarized in Ref. [62]. Mott scattering, as it has been presented in Chapter 2, does not take into account the possibility of the incident electron to form a quasi-bound state. However, if the energy of the elastically scattered electron is close enough to one of the energies of the excited states of the atom, it is possible for the electron to be temporarily bound to the atom in an ionic compound. This quasi-bound state significantly increases the cross-section of the scattering process. Then if spin-orbit coupling is present in the excited state, two peaks are present in the cross-section as a function of electron kinetic energy. It can be shown that this corresponds to a spin polarization that switches sign between the two peaks. This effect is known as *Feshbach resonance*. A similar mechanism, known as *shape resonance*, relies on the particular shape of the atomic potential in conjunction with the centrifugal potential of the trapped electron. Whereas Feshbach resonances have energies that are lower than the parent atomic excited state, shape resonances have higher energies. The parallel with photoemission could be done by considering that the electrons that will be photoemitted are naturally at the energy that allows a bound state, i.e. the energy where the photohole is formed. Therefore, during the photoemission process, the entangled photoelectron-photohole system might experience all these fine corrections from electron scattering formalism that lead to a  $\pi$  phase shift, which will experimentally result in a DPF.

### 5.3 Spin-resolved survey of the 3p core levels

In order to study the influence of possible additional effects on the measured spin polarization, a set of spin-resolved EDCs over the 3p core levels of Cu(111) has been measured. The 3p level is spin-orbit split into  $3p_{1/2}$  ( $E_b = 77.3$  eV) and  $3p_{3/2}$  ( $E_b = 75.1$  eV). Because of the strong localization of the core levels, the spin polarization is expected to follow the atomic photoionization model described in Section 3.3.1. This measurement has already been performed in the past [66], but only the component relevant to atomic symmetry was considered (i.e. the one that corresponds to  $P_y$  in the COPHEE setup), and the other two were said to be necessarily zero.

In Fig. 5.10(a) a comparison of EDCs measured with  $h\nu = 130$  eV at three different angles is shown. The three angles  $\theta_{1,2,3}$  correspond to  $\Gamma$  (i.e. normal emission) and to the particular  $k_{\parallel}$  at which the *sp* band crosses the Fermi level for the two photon energies 130 eV and 46 eV respectively. As already mentioned in Section 5.2, the measurements do not show any sign of DPF. In fact, here the up/down feature in the spin signal corresponds to the two core levels,

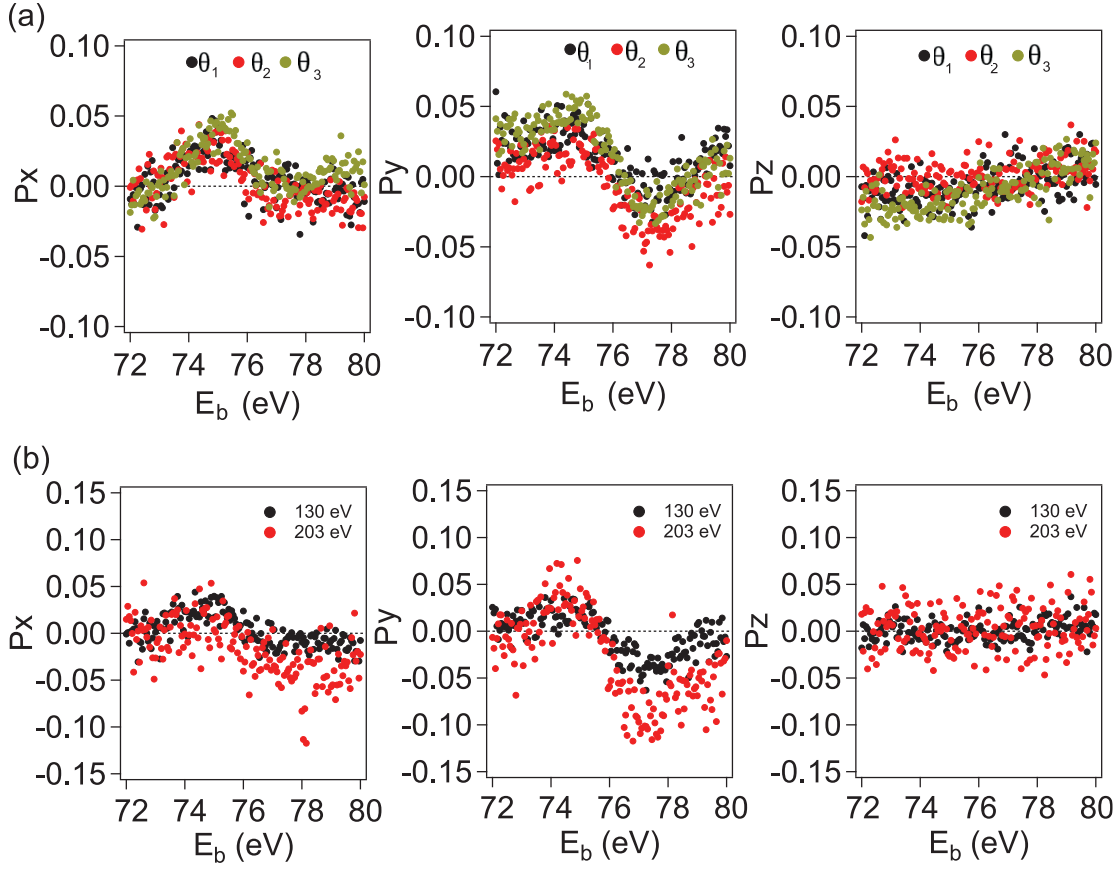


Figure 5.10: Spin-resolved EDCs over the Cu(111)  $3p$  core levels (a) as a function of  $\theta_p$  ( $h\nu = 130$  eV,  $\theta_1 = 0^\circ$ ,  $\theta_2 = 12.5^\circ$ ,  $\theta_3 = 22.5^\circ$ ), and (b) as a function of  $h\nu$  ( $\theta_p = \theta_2$ ).

where an opposite spin polarization is expected because of the different value of  $j$  [66], as shown in Fig. 5.5(c) (which is the same as in Fig. 5.10 with  $h\nu = 130$  eV and  $\theta_p = \theta_2$ ). In addition to  $P_y$ , also  $P_x$  shows a certain degree of polarization, suggesting that the orientation of the spin polarization vector in crystals does not strictly follow the symmetry arguments of completely isotropic atomic targets. An important observation is that the three measurements at different angles are equivalent within the experimental resolution. Therefore one can conclude that the spin polarization discussed in Section 5.2 for the estimate of EWS time delays (measured at  $\theta_{2,3}$  for the two photon energies 130 eV and 46 eV) is *not affected by diffraction* through the surface, since these effects should vanish at normal emission ( $\theta_1$ ), and should be strongly dependent on the particular angular position.

In Fig. 5.10(b) the two photon energies  $h\nu = 130$  eV and  $h\nu = 203$  eV are compared, which places the  $3p$  levels at about the same  $E_k$  of the experiment performed on the  $sp$  band at  $h\nu = 46$  eV and  $h\nu = 130$  eV, respectively. The two measurements differs only in the  $P_y$  component, which changes by about a factor of 2. Given the large difference in kinetic energy, this suggests that effects related to scattering and transport to the surface are not the main cause of the spin polarization, since a change of a factor of 2 is also observed in the much



smaller energy range of the measurement shown in Fig. 5.4. Noticeably, a careful study of the variation of the spin polarization from the core levels with photon energy would be very interesting, in order to access the phase (and therefore time) information for these localized states, along the lines of the atomic photoionization measurements performed in the past [63]. In particular, a comparison with time-resolved experiments would be easier given their limited energy resolution. However, given the relatively low photoemission intensity of the core levels at these photon energies and the present state-of-the-art quantitative 3D spin polarization measurements, such experiments would be highly time-consuming.

### 5.4 Spin polarization from the $d$ bands

The spin polarization from the  $d$  bands has also been investigated. Given their small dispersion and their intricate structure, a binding energy dependent study aimed to extract information on the EWS time delays is not feasible. However, it is interesting to observe that also in this case, where a spin-degenerate state is being probed, a spin polarization is measured.

In Fig. 5.11 all the three spatial components of  $\mathbf{P}$  for four spin-resolved EDCs are shown, together with the corresponding spin up and down channels  $N^{\uparrow,\downarrow}$  obtained from Eq. (2.4). The four EDCs have been performed with photon energies of 28 eV, 34 eV and 46 eV using  $\pi$  light polarization, and  $\sigma$  light polarization for  $h\nu = 46$  eV. The measurements have been performed at normal emission ( $\theta_p = \theta_1 = 0^\circ$ ). In Fig. 5.12 the same data set has been measured off-normal emission with an emission angle  $\theta_p = \theta_4 = 16.4^\circ$ . As shown in Fig. 5.9, a larger binding energy spread of the  $d$  bands is expected for  $\theta_4$  than for  $\theta_1$ . The following observations can be made about the spin signals.

- All the states show a high degree of measured spin polarization up to almost 50%, with non-zero components of  $\mathbf{P}$  in all the three spatial directions. In contrast to the measurement on the  $3p$  core levels of Fig. 5.10, here the  $P_y$  component is not the largest. This is sign that also for the  $d$  bands the crystal symmetry plays a role in determining the direction of  $\mathbf{P}$ , as in the case of the  $sp$  band [Fig. 5.5(b)].
- The general trend is a decrease of spin polarization signal with increasing photon energies, but the different states have different dependencies.
- Some of the states show a high degree of linear dichroism, where the photoemission intensity is strongly suppressed for  $\sigma$  polarization compared to  $\pi$  (see for example the state marked as 2 in the  $N_x^\uparrow$  or  $N_x^\downarrow$  plot at 46 eV in Fig. 5.11), whereas other states do not sensibly change (for example the state marked as 1 in the same plot).
- Also the spin signal shows some dichroic features, since not only the states with dichroism in the intensity but also some of those who do not change in intensity have a variation of spin polarization with light polarization (as in the  $P_z$  component of the previously mentioned state marked as 1). This is a hint of a possible interplay between

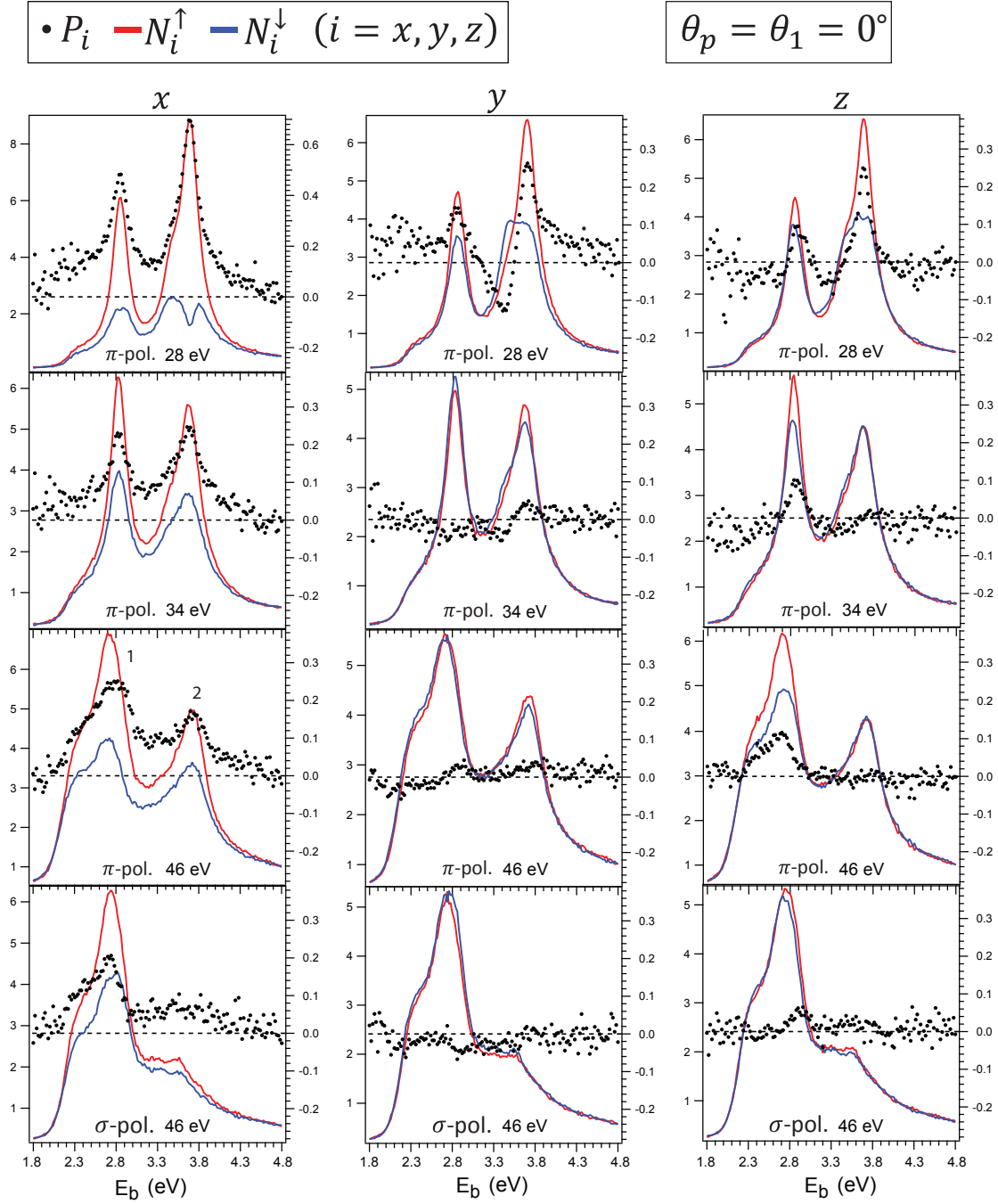
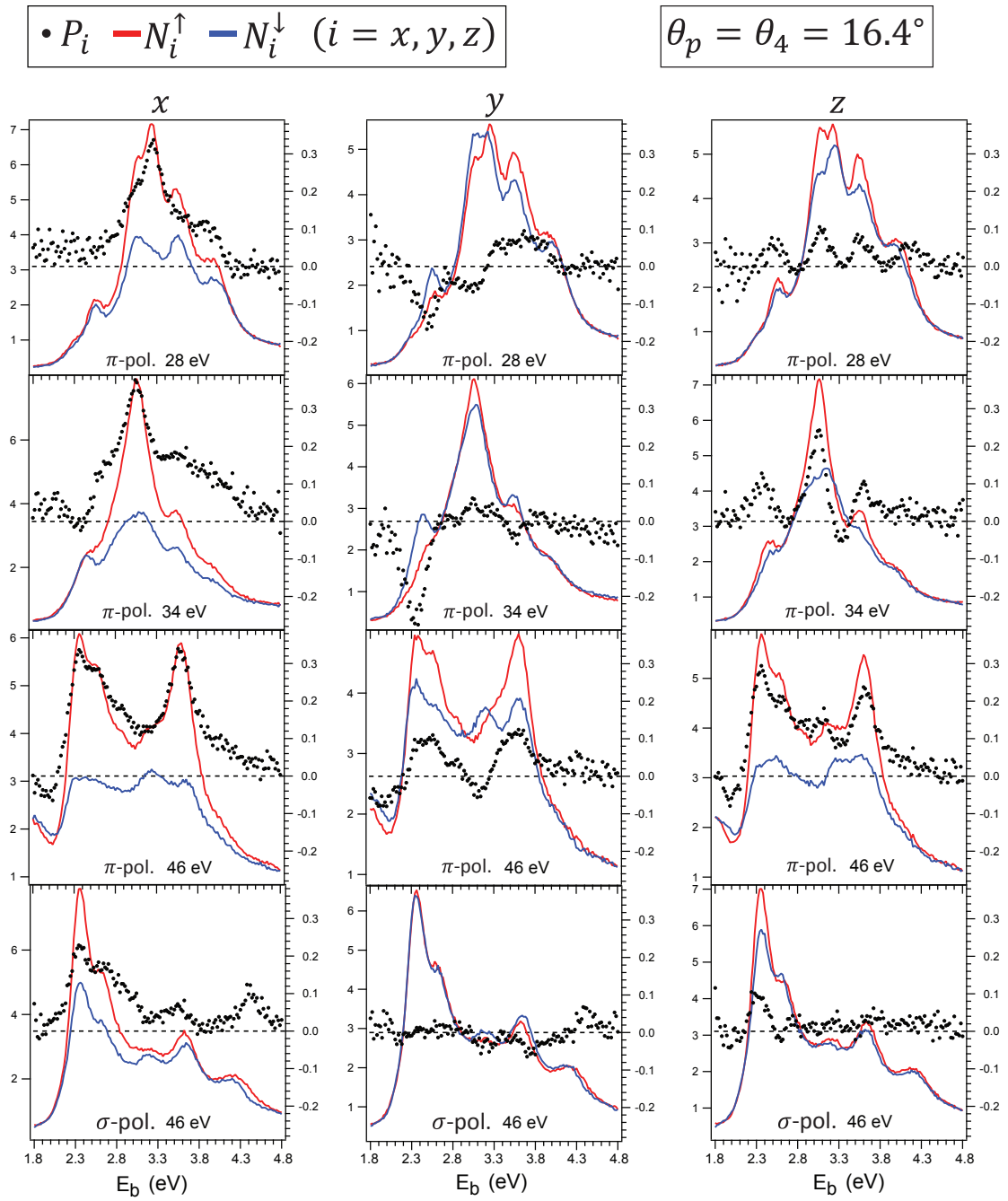


Figure 5.11: Spin-resolved EDCs over the Cu(111)  $d$  bands measured as a function of photon energy and light polarization. Each plot shows the spin up channel (red line) and spin down channel (blue line) along the spatial direction  $i = x, y, z$  in millions of counts (left axis), as well as the spin polarization component  $P_i$  (black dots, right axis). The emission angle is  $\theta_p = \theta_1 = 0^\circ$ , corresponding to the  $\Gamma$  point, i.e. normal emission.




 Figure 5.12: Same as Fig. 5.11, measured off-normal emission with an angle  $\theta_p = \theta_4 = 16.4^\circ$ .

spin polarization and linear dichroism, which is important to study for a better understanding of spin-resolved measurements in general [167].

At least five peaks can be identified in the scans of Fig. 5.11, which correspond to the 5  $d$  states. However it is difficult to carefully analyze this kind of measurements with the present resolution, in order to disentangle the spin information from the different states as well as to find the possible presence of DPFs. Nevertheless, this example shows a further potential application of spin-resolved ARPES on spin-degenerate states: the possibility of accessing the information about the symmetry of the probed states through dichroism analysis of the spin polarization.

## 6 Results: the strongly correlated material BSCCO

*"The more that I see, the less that I know for sure."*  
- John Lennon, *Borrowed time* (1980)

In this Chapter, a study of the spin polarization and the EWS time delays in photoemission from the cuprate superconductor  $\text{Bi}_2\text{Sr}_2\text{CaCu}_2\text{O}_{8+\delta}$  (BSCCO) will be presented. Despite the limitation of the COPHEE endstation for a demanding system such as BSCCO, a comparison of this strongly correlated electron system with the free electron-like system such as Cu(111) will be discussed. The main findings have been published in Ref. [168]. Also, recent laser-SARPES experiments performed on BSCCO at the University of Tokyo will be shown.

### 6.1 Photoemission from BSCCO 2212

Copper oxide-based compounds (*cuprates*) are one of the most studied class of materials among the *unconventional high  $T_C$  superconductors*. These are materials where superconductivity is not accounted for by the well established Bardeen-Cooper-Schrieffer (BCS) model [169], and where the superconducting critical temperature  $T_C$  can be much higher than the one limited by the BCS theory, i.e.  $\approx 30$  K [170]. Cuprates have been discovered by Georg Bednorz and K. Alex Müller [171], for which they received the Nobel Prize in 1987. They have a layered perovskite crystal structure, where  $\text{CuO}_2$  planes are separated by spacer layers as shown in Fig.6.1(a).

Cuprate superconductors are representative systems for the study of strong electron correlations, and as such they have been probed extensively by ARPES [174–179]. A strongly correlated material is characterized by electronic properties that cannot be described by considering any electron to be influenced by the average "sea" of all the other electrons, but the interaction among them become relevant also on a qualitative level. In particular, the spectral function mentioned in Section 3.1.1 is modified from a simple series of delta functions to a more complex, material-dependent function with a main peak and several satellites.

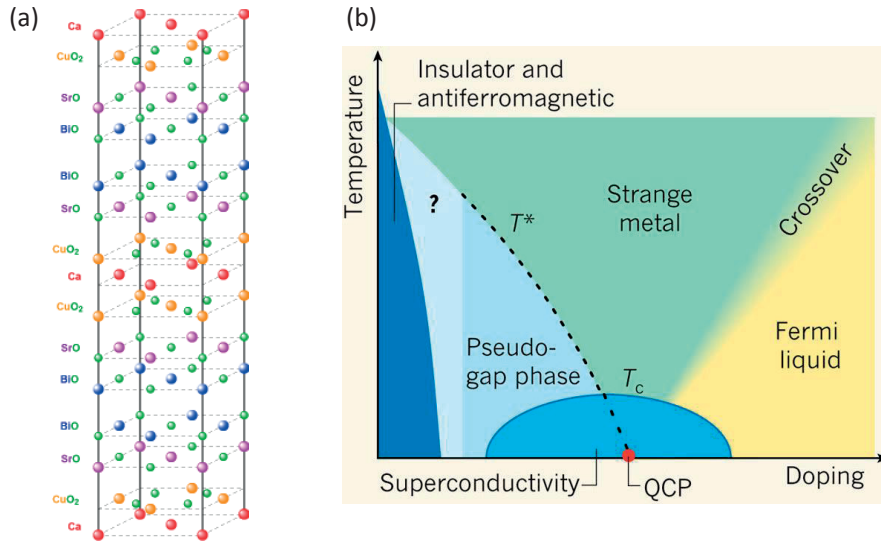


Figure 6.1: (a) Bi<sub>2</sub>Sr<sub>2</sub>CaCu<sub>2</sub>O<sub>8+δ</sub> unit cell (from Ref. [172]). (b) Typical phase diagram of a cuprate (from Ref. [173]).

Among cuprates, the bismuth strontium calcium copper oxide (BSCCO, pronounced "bisko") is a well-known example. Its non-stoichiometric chemical formula is Bi<sub>2</sub>Sr<sub>2</sub>Ca<sub>n-1</sub>Cu<sub>n</sub>O<sub>2n+4+δ</sub>, with  $n$  integer; in particular, the three cases  $n = 1$  (Bi<sub>2</sub>Sr<sub>2</sub>CuO<sub>6+δ</sub>, BSCCO 2201,  $T_C \approx 8$  K),  $n = 2$  (Bi<sub>2</sub>Sr<sub>2</sub>CaCu<sub>2</sub>O<sub>8+δ</sub>, BSCCO 2212,  $T_C \approx 95$  K) and  $n = 3$  (Bi<sub>2</sub>Sr<sub>2</sub>Ca<sub>2</sub>Cu<sub>3</sub>O<sub>10+δ</sub>, BSCCO 2223,  $T_C \approx 108$  K) are the most studied. The crystal unit cell of BSCCO 2212 is shown in Fig. 6.1(a). The phase diagram of cuprates is extremely rich, as it is shown in Fig. 6.1(b). As a function of temperature and hole doping, in particular, they can show antiferromagnetic insulating phase, normal Fermi liquid phase and superconducting phase, among other more exotic phases. The  $T_C$  of the superconducting phase varies with doping, and a cuprate with a doping where  $T_C$  is maximum is referred to as optimally doped.

Spin-resolved photoemission has already been employed to study BSCCO, but only with angle-integrated measurements performed with circularly polarized light of energy  $h\nu = 931.5$  eV, which is resonant to the Cu L<sub>3</sub> absorption edge [180]. In this particular case, the resonant process was exploited in order to determine the Zhang-Rice singlet character of the relevant low energy states in BSCCO, thus improving the description of its electronic structure. The experiments presented in this Chapter are the first characterization of BSCCO by means of spin-resolved photoemission while maintaining the full energy and angular resolution of ARPES. It will be shown that even in the less-specific case of off-resonance photoemission, a sizable spin polarization  $\mathbf{P}$  is measured as a function of energy and momentum. The states under investigation are not spin polarized, thus the measured  $\mathbf{P}$  is a result of the photoemission process according to the model presented in Chapter 4 and similarly to the results on Cu(111) presented in Chapter 5. Therefore, this case study of BSCCO allows to access the phase information in the photoemission process, which leads to qualitatively new insights in the study of strong correlations in high temperature superconductors.

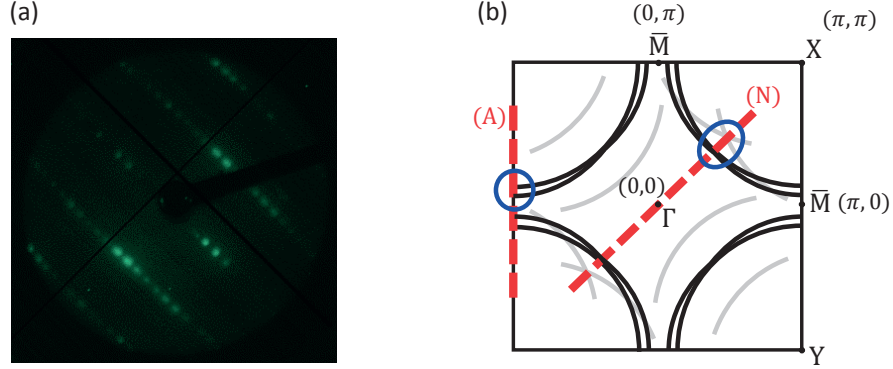


Figure 6.2: (a) LEED image of a freshly cleaved BSCCO 2212 sample ( $E_k \approx 107$  eV). (b) Scheme of the Fermi surface of BSCCO 2212. The red lines indicate the nodal (N) and antinodal (A) directions, which have been probed with the spin-resolved MDCs. The blue circles indicate the error margin of the measurements because of difficulties of the alignment.

A batch of optimally doped BSCCO 2212 samples has been measured at COPHEE (see Section 3.2.1). An optimally doped BSCCO 2201 sample has also been measured as a comparison. All the samples have been provided by Enrico Giannini (University of Geneva) and Fabrizio Carbone (EPFL). The BSCCO 2212 sample growth and characterization is reported in Ref. [181], whereas the characterization of BSCCO 2201 can be found in Ref. [182]. The BSCCO samples were cleaved *in situ* with a glued top post at low temperature ( $T = 20$  K) and at a base pressure lower than  $1 \times 10^{-10}$  mbar in order to obtain a clean surface for the SARPES experiment. The surface quality and orientation were checked by Low Energy Electron Diffraction (LEED), which is reported in Fig. 6.2(a). All the spin-resolved measurements were performed at 20 K, therefore the BSCCO 2212 was in the superconductive phase, whereas BSCCO 2201 was in the normal phase. Because of the low photoemission count rate of the states close to the Fermi level and the need to mitigate effects of deterioration of the sample's surface with time, only one of the two Mott detectors of the COPHEE endstation was used, reducing the acquisition time by a factor of 2. Thus only two spatial components of  $\mathbf{P}$  were measured, namely  $x_M$  and  $z_M$ . Instead of the sample coordinate frame of Fig. 3.6(e), the relevant geometry to be considered for this experiment is the one in the Mott coordinate frame shown in Fig. 3.6(d). The different regions of the Fermi surface were reached by moving the sample's normal  $\mathbf{s}$  by changing the angles  $\phi$  and  $\theta_p$ . All the MDC measurements were performed with  $\pi$  polarized light of energy  $h\nu = 50$  eV by scanning the angle  $\theta_t$ . The choice of this angle instead of  $\theta_p$  as in the measurements on Cu(111) presented in Chapter 5 is due to the difficulties inherent in aligning a system without states around the  $\Gamma$  point with the single channel setup at COPHEE, as well as to a better count rate in this geometry. This choice requires a modification of some details of the model presented in Chapter 4, as discussed in Section 6.3.

A sketch of the BSCCO Fermi surface with its common labeling is shown in Fig. 6.2(b). The band under consideration that encloses the Brillouin zone corners is the  $\text{CuO}_2$ -derived state of BSCCO 2212, which is relevant for the superconductivity. The state is affected by *umklapp*

bands due to diffraction by the Bi atoms at the cleaved surface [183], as it is also visible in the LEED reconstructed pattern of Fig. 6.2(a). In the BSCCO 2212 case, the state presents a splitting into bonding and antibonding states due to the presence of a  $\text{CuO}_2$  bilayer within the unit cell [174]. In particular, the  $\overline{\Gamma X}$  and  $\overline{YM}$  directions in reciprocal space were considered. These are known in literature as nodal (N) and antinodal (A) directions, respectively, since the superconducting gap is closed along N and largest along A, and they are shown by red dashed lines in Fig. 6.2(b). The error margins in the precise orientation of the sample because of the difficult alignment are shown by two blue circles on the N and A directions in Fig. 6.2(b). As a note, another common labeling in the field of cuprates consists in calling the corners and the center of the edges of the Brillouin Zone as  $(\pi, \pi)$  and  $(\pi, 0)$  respectively, where  $\pi$  indicates the position at  $\pi/a$  in  $k$ -space in units of cell size  $a$ .

### 6.2 Spin polarization from the $\text{CuO}_2$ -derived band

In Fig. 6.3(a) and (b), the two  $P_{x_M}$  and  $P_{z_M}$  spatial components of  $\mathbf{P}$  are shown for MDC scans along the nodal and antinodal directions, respectively. The  $P_{z_M}$  component shows no clear dependence on momentum. On the other hand, all the bands at positive and negative momenta for the nodal and antinodal directions present a clear momentum-resolved spin polarization along the  $x_M$  direction, with a value that reaches about 10%. Notably, each photoemission intensity peak in the antinodal direction presents an up-down spin structure reminiscent of the double polarization feature (DPF) observed in Cu(111) (see Section 5.2.1). In the nodal direction, the photoemission intensity peaks are more structured, and there appear to be two partially overlapped DPFs, as it can be better seen in Fig. 6.3(c), which shows a zoom of  $P_{x_M}$  for negative momenta from Fig. 6.3(a). The signal was fitted with four Gaussian peaks, with same width and opposite height for each pair of peaks constituting a DPF. Whereas the bonding and antibonding states of BSCCO 2212 might play a role in the spin signal but are not resolved, the two DPFs corresponding to the photoemission intensity peaks at  $\approx -0.35$  Å and  $\approx -0.55$  Å can be assigned to the main band and to the *umklapp* replica, respectively. As suggested by the structured photoemission intensity peak, the *umklapp* replica is possibly enhanced by the misalignment indicated by a blue circle in Fig. 6.2(b). A similar behavior is also observed at positive momenta, where, however, the total intensity is lower.

For comparison, the same scan along the nodal direction was measured in the non superconducting state of the related compound BSCCO 2201, as shown in Fig. 6.3(d). The presence of a clear spin polarization signal with DPF arising from this system as well, which has no bilayer splitting, excludes any possible interpretation of the spin polarization signal as a direct consequence of the bonding and antibonding splitting, or of the superconducting state itself.

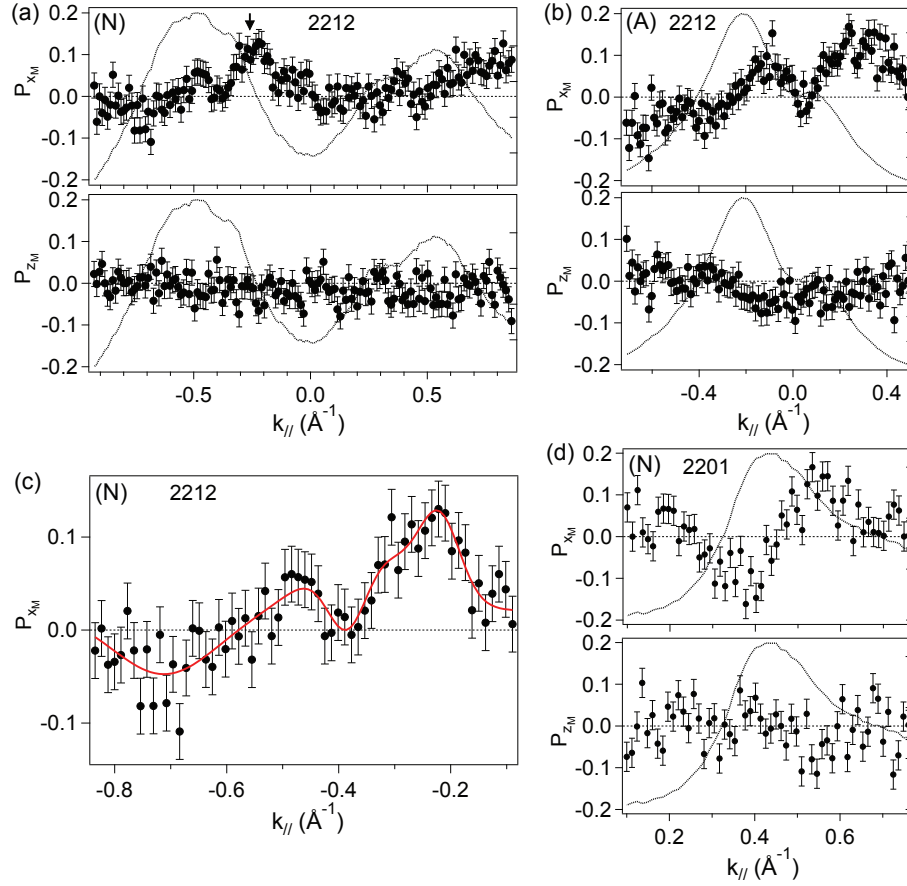


Figure 6.3:  $P_{x_M}$  and  $P_{z_M}$  spatial components of  $\mathbf{P}$  for MDCs along the (a) nodal and (b) antinodal directions at 40 meV below the Fermi level. The arrow in (a) indicates the momentum position of the spin-polarized peak considered to construct the plot of Fig. 6.4(b). (c) A closeup of  $P_{x_M}$  for negative momenta from (a), in which two DPFs appear in the spin signal as highlighted by the fit with four Gaussian peaks (red line). (d) Reference measurement on BSCCO 2201, which is not superconducting at 20 K; same direction as in (a). In (a), (b) and (d) the photoemission total intensity is also shown in arbitrary units as a dotted black line.

### 6.3 Estimate of EWS time delays

In Fig. 6.4(a), the bandmap measured on BSCCO 2212 along the nodal direction is shown. Red solid lines indicate the MDCs that were measured with spin resolution in nonsequential order to avoid possible effects related to sample aging. Since the  $P_{z_M}$  signal from Fig. 6.3(a) is considerably smaller compared to  $P_{x_M}$ , only  $P_{x_M}$  will be considered. According to the model presented in Chapter 4, the relevant quantity for the estimate of the EWS time delays is the slope of the spin polarization versus binding energy. Therefore  $P_x(E_b)$  is constructed by plotting the spin polarization for one peak from each MDC measured at different  $E_b$ . The peak closer to  $\Gamma$  has been chosen because it is the cleanest by virtue of being less influenced by



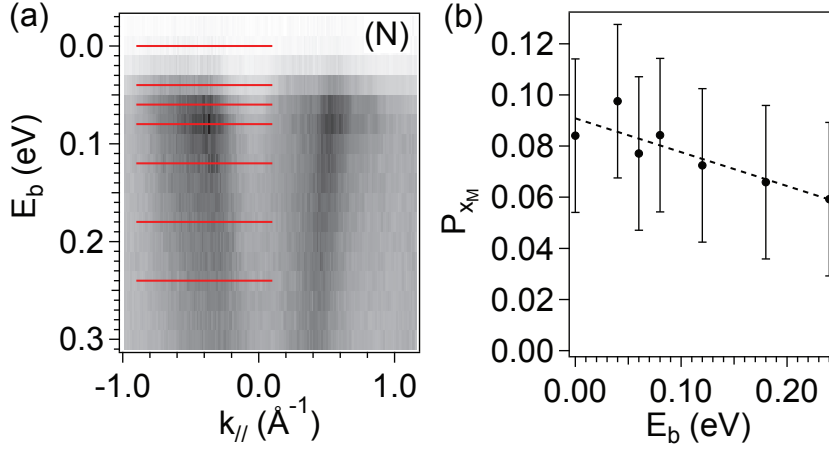


Figure 6.4: (a) Band map along the nodal direction, with red lines indicating the spin-resolved MDCs. (b) Plot of  $P_{x_M}(E_b)$ . The absolute slope of  $0.13 \text{ eV}^{-1}$  is used to estimate  $\dot{P}$  and thus the EWS time delay.

overlaps with other DPFs, as indicated by an arrow in Fig. 6.3(a). The plot of  $P_{x_M}(E_b)$  is shown in Fig. 6.4(b), with an obtained absolute value of the slope of  $|\dot{P}_{x_M}| \approx 0.13 \text{ eV}^{-1}$ .

Since there is no information about the third component  $P_{y_M}$  from the measurement, it is not possible to proceed with a careful estimate of the EWS time delays, in contrast to the case of Cu(111) in Chapter 5. In particular, it is not possible to obtain the quantity  $\dot{P}$ , and neither the angles  $\psi$  and  $\delta$  which determine the parameter  $t$  via Eq. (4.4) (see Chapter 4). In addition, Eq. (4.4) itself would not be correct, since the geometrical correction in Chapter 4 has been developed for a  $\theta_p$  MDC scan, whereas in this case the angle  $\theta_t$  was varied, and therefore it would be necessary to develop a similar equation for the evaluation of  $t$ . However, it is at least possible to give an estimate of the lower limit of  $|\tau_{EWS}^s|$  from Eq. (4.10) in the following way. Under the assumption that  $\mathbf{P}$  does not vary direction but only its modulus in the measured  $E_b$  range, similarly to what was found in Cu(111), one can write  $|\dot{P}| \geq |\dot{P}_{x_M}|$  and therefore still find a finite lower limit for the interfering channels EWS time delay as:  $|\tau_{EWS}^s| \geq \hbar|\dot{P}| \geq \hbar|\dot{P}_{x_M}|$ . If, for example, one assumes  $P_{y_M} \approx 0$ , then  $\dot{P} \approx \dot{P}_{x_M}$  and therefore  $|\tau_{EWS}^s| \geq 85 \text{ as}$ , whereas if  $P_{y_M}(E_b) \approx P_{x_M}(E_b)$  then  $|\tau_{EWS}^s| \geq \hbar|\dot{P}_{x_M}|\sqrt{2} \approx 120 \text{ as}$ . These values are at least 3 times larger than the one found for Cu(111), which was  $\approx 26 \text{ as}$  (see Section 5.2).

For completeness, it is worth to mention that this estimate of  $|\tau_{EWS}^s|$  is the simplest and the one that does not rely on the specific geometry of the experiment, where none of the values of  $r$ ,  $t$ ,  $\delta$ ,  $\psi$  are considered. A measurement with information about  $P_y$  should yield a better estimate of  $|\tau_{EWS}^s|$ , which will be larger than the one given here, according to Eq. (4.10). With regard to  $|\tau_{EWS}|$ , on the other hand, as it was described in Section 5.2 it is at least necessary to first give an estimate of the parameter  $r$ . By construction, for a  $\theta_t$  MDC it can be found that at  $\theta_p = 0^\circ$  one has  $r = 1/\cos\theta_t \approx 1$  for small values of  $\theta_t$  (such as  $\theta_t \approx 7^\circ$  in the measurement under consideration). Therefore, one can calculate  $\max|m|$  in Eq. (4.11) and find  $|\tau_{EWS}| \geq 43 \text{ as}$  as if one assumes  $|\dot{P}| \approx |\dot{P}_{x_M}|$ , and  $|\tau_{EWS}| \geq 60 \text{ as}$  as by assuming  $|\dot{P}| \approx |\sqrt{2}\dot{P}_{x_M}|$ . Since the maximum



of the function  $m(t)$  is considered, this result does not require an estimate of the parameter  $t$ . Also in this case, the estimate of the EWS time delay is sensibly larger compared to the one found for Cu(111), which was  $\approx 11$  as (see Section 5.2). The reason is that apart from the small corrections of the geometrical model the measured spin polarization variation with binding energy is much larger. However, the investigated binding energy range was necessarily much smaller, and is therefore less suited to make precise estimates about the slope of  $P(E_b)$ . A discussion on the different EWS time delays in the correlated system BSCCO 2212 and in the Fermi liquid system Cu(111) can be found in Chapter 7.

## 6.4 Laser SARPES on BSCCO 2212

The main limitations of the results presented in the previous Sections are due to the difficulties of measuring a sample such as BSCCO at the COPHEE endstation, both because of the challenging alignment of a system without states around the  $\Gamma$  point with a single-channel analyzer, and because of the limited energy resolution. In order to overcome these issues, laser-based SARPES experiments have been performed in January 2018 at the Laser and Synchrotron Research Center (LASOR) at the Institute for Solid State Physics of the University of Tokyo, and these recent results will be briefly shown in this Section.

The laser SARPES setup at LASOR is equipped with a SCIENTA-OMICRON DA30L hemispherical analyzer and two highly efficient VLEED spin detectors that allow to measure all the three spatial component of the spin polarization of the photoelectrons [107]. The light source [184] is based on a commercial frequency tripled Nd:YVO<sub>4</sub> quasi-continuous wave laser (repetition rate of 160 MHz), and an energy of  $h\nu = 6.994$  eV corresponding to the 6<sup>th</sup> harmonics is obtained using an optical contact prism coupling technique [185] with a nonlinear KBe<sub>2</sub>BO<sub>3</sub>F<sub>2</sub> crystal [186].

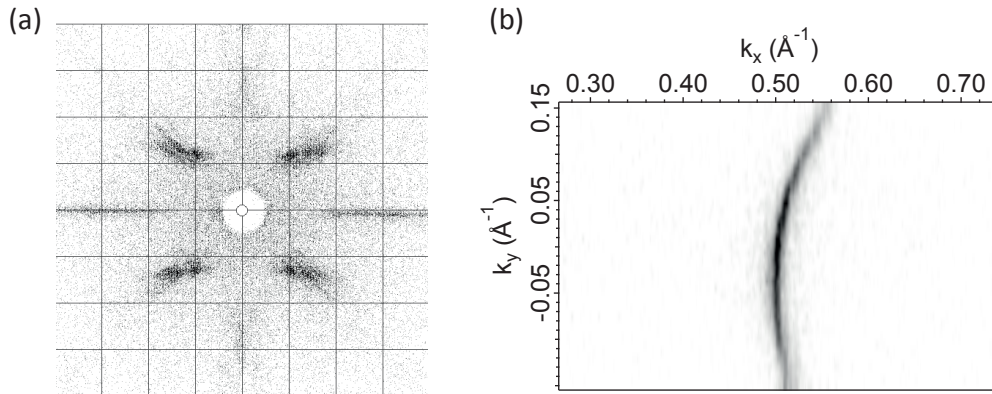


Figure 6.5: (a) Laue diffraction pattern, where the horizontal direction corresponds to the  $a$  axis. (b) Fermi surface of BSCCO 2212 measured at LASOR.

The BSCCO 2212 sample was grown by Edoardo Martino and László Forró at EPFL. The sample was cleaved *in situ* at a temperature of  $T = 35$  K. The azimuthal orientation of the sample was

checked by Laue diffraction at EPFL [Fig. 6.5(a)]. In Fig. 6.5(b) the portion of the constant energy map reachable with  $h\nu = 6.994$  eV is shown, with the nodal direction aligned along  $k_x$ . The state was reached in  $k$ -space by rotating the polar angle, and the angular resolution in the spin-resolved measurement is obtained with the deflector electron lens of the analyzer.

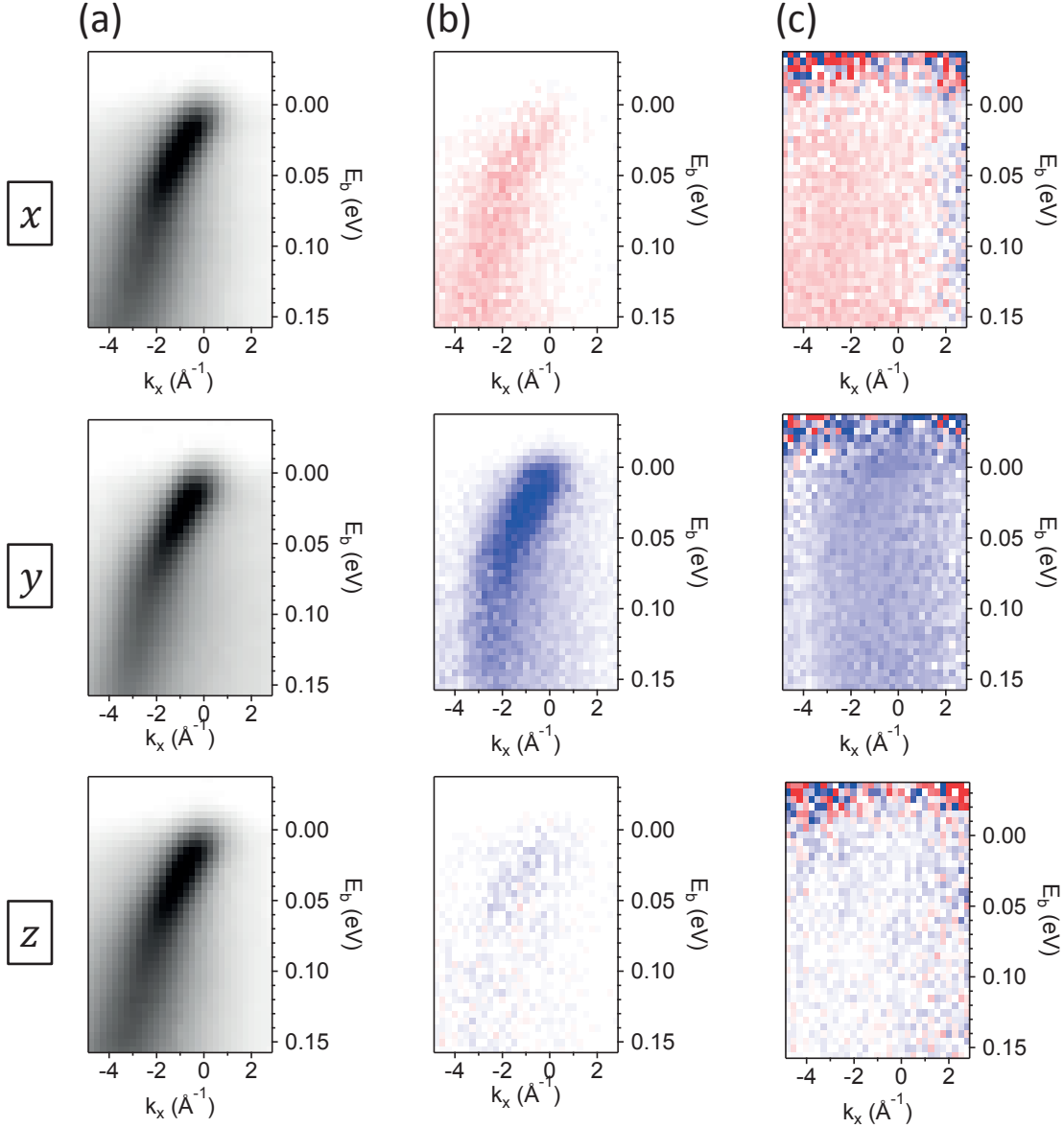


Figure 6.6: Spin resolved measurement of BSCCO 2212 at LASOR for the three spatial components  $x, y, z$  in the detector coordinate frame. The zero of the  $k_x$  axis is set at  $k_F = 0.5 \text{ \AA}^{-1}$ . (a) Total intensity  $I^\uparrow + I^\downarrow$ . (b) Intensity difference  $I^\uparrow - I^\downarrow$ . (c) Spin polarization (color scale from red to blue corresponding to  $-1$  to  $+1$ ).

In Fig. 6.6 the spin resolved measurement of BSCCO 2212 performed with  $\sigma$  polarized light is displayed. In panel (a) the total intensity measured by the spin detector ( $I^\uparrow + I^\downarrow$ ) is shown for the three spatial components (in the spin detectors coordinate frame, see Ref. [107] for

details), whereas in panel (b) the intensity differences ( $I^\uparrow - I^\downarrow$ ) are shown. Panel (c) shows the spin polarization evaluated according to Eq. (3.16) (with Sherman function  $S = 0.29$ ). The main signal in intensity differences is in the  $y$  direction, which corresponds to the direction perpendicular to the mirror plane  $\overline{MTM}$ . Two main differences are found between this measurement and the one performed at COPHEE presented in the previous Sections. First, there is no clear indication of a DPF: the asymmetry peak corresponds to the position of the total intensity peak. Second, not only the spin polarization does not present a DPE, but it does not even show any clear peak, since only an overall constant value is observed. This is better illustrated in Fig. 6.7, where both the bandmap of total spin polarization (a) and a spin-resolved EDC along  $y$  performed close to  $k_F$  show a constant featureless total spin polarization.

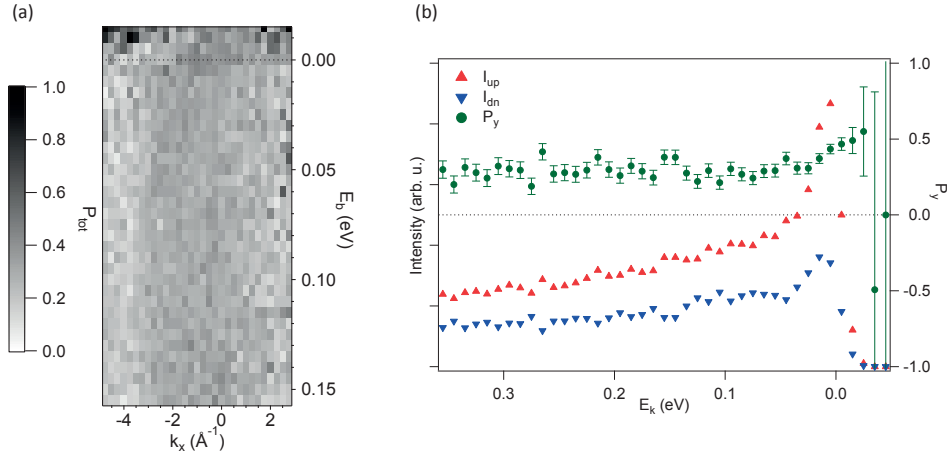


Figure 6.7: (a) Total spin polarization obtained from Fig. 6.6(c). The zero of the  $k_x$  axis is set at  $k_F$ . (b) High statistics spin-resolved EDC along  $y$  performed close to  $k_F$ .

In this Chapter, the nature of the interfering transitions in BSCCO 2212 has not been addressed. Whereas in Cu(111), as discussed in Chapter 5, they are suggested to be the two spatial parts of the double group representation that are selected by in-plane and out-of-plane components of the  $E$  field of the light, in BSCCO 2212 the situation can be more complicated. In fact, further possibilities must be considered, such as the contribution from bonding and antibonding states, *umklapp* states, and the intrinsic hybridization of the  $d$ -derived states of Cu and  $p$ -derived states of O. A possibility to explain the observations of Fig. 6.6 is to consider the fact that at the low photon energy of the laser compared to the synchrotron radiation, the final state reached by the photoelectrons might have a single well defined orbital composition. This would mean that only one single transition is allowed from the CuO<sub>2</sub> state, and therefore no interference between different partial channels can occur. If this is the case, the phase and time information would not be accessible by SARPES, since it implies that the parameter  $r$  is either  $r \rightarrow 0$  or  $r \rightarrow +\infty$ , and therefore according to Eq. (4.7) no spin polarization is produced. In order to be confirmed, this argument certainly requires theoretical calculations of the final states composition, which are currently being performed [163].

## Chapter 6. Experimental results: the strongly correlated material BSCCO

For the time being, an observation that supports the argument of one single transition at this photon energy is shown in Fig. 6.8, where the photoemission intensity integrated in an energy and angular range that covers the full  $\text{CuO}_2$  state displayed in Fig. 6.6(a) is plotted versus the light polarization vector orientation. The intensity of the light is independent of

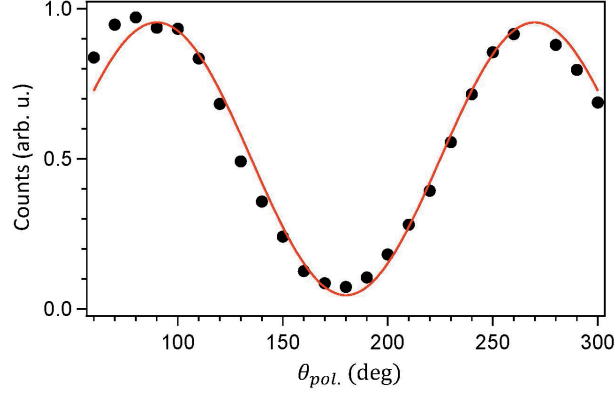


Figure 6.8: Photoemission intensity of the  $\text{CuO}_2$  state versus light polarization angle ( $\theta_{pol} = 0$  for  $\pi$  polarization). The curve is fitted with Eq. (6.1).

the polarization in the laser setup, and the angle  $\theta_{pol}$  is defined to be 0 when the light is  $\pi$  polarized. The photoemission intensity is maximum when the light is  $\sigma$  polarized, as required by the symmetry of the initial state. If only two transitions are allowed, a simple scenario that is considered throughout this Thesis, then the photoemission intensity [124] would be given by

$$I(\theta_{pol.}) \propto |c_2|^2 \sin^2 \theta_{pol.} + |c_1|^2 \cos^2 \theta_{pol.} = |c_2|^2 \sin^2 \theta_{pol.} + (1 - |c_2|^2)(1 - \sin^2 \theta_{pol.}), \quad (6.1)$$

where  $c_{1,2}$  are the complex weights of the two channels. Fitting the curve in Fig. 6.8 with Eq. (6.1) gives  $|c_2|^2 = 0.955$ , which is very close to 1, and the parameter  $r$  can be calculated as

$$r = \frac{R_2}{R_1} = \sqrt{\frac{|c_2|^2}{|c_1|^2}} = \sqrt{\frac{|c_2|^2}{1 - |c_2|^2}} = \sqrt{\frac{I_{max}}{I_{min}}}, \quad (6.2)$$

where  $I_{max}$  and  $I_{min}$  are the photoemission intensity obtained in this case with  $\sigma$  and  $\pi$  polarization, respectively<sup>1</sup>. Using Eq. (6.2) one finds  $r \approx 4.6$  for the measurement on BSCCO 2212, which is large but not  $r \rightarrow +\infty$ . However, it is important to consider also the fact that the light polarization of the laser is 95% linear, a value that accounts well for  $|c_2|^2$  being not exactly 1.

At this point, the reason why a net constant spin polarization is observed still remains an open question. First of all, such a constant could be an offset of the experimental setup. In a spin

<sup>1</sup> Interestingly, the expression  $\sqrt{\frac{I_{max}}{I_{min}}}$  also gives  $\tan \theta_{pol}^0$  when spin polarized states are considered, where  $\theta_{pol}^0$  is the special light polarization angle for which the spin polarization component corresponding to the initial state spin polarization vanishes because of interference (and the perpendicular component is maximum), as discussed in Ref. [124].

polarized photoelectron beam, a small offset can be easily overlooked when compared to the actual spin signal, but if the  $\text{CuO}_2$  state gives perfectly unpolarized electrons at the laser photon energy then it becomes an issue. Even if more unlikely in a VLEED detector rather than in a Mott detector, still it is difficult to exclude this completely. On the other hand, it might still be that at this low photon energy the  $\text{CuO}_2$  state of BSCCO does give rise to spin polarized electrons for other reasons, for example with contributions from its incoherent tail. Once again, spin-resolved one-step photoemission calculations will help to elucidate this point.



## 7 Discussion on EWS time delays in photoemission and concluding remarks

*"Ἀλλὰ καὶ ἐπιχειροῦντί τοι τοῖς καλοῖς καλὸν καὶ πάσχειν σὶ ἀν τῷ συμβῆ παθεῖν"*  
*"In striving after Beauty, also whatever one must go through is beautiful."*  
- Plato, *Phaedrus*, 274b (ca. 370 BC)

The chronoscopy of photoemission is a fundamental topic in modern physics [22]. Time-resolved photoemission experiments show that the time scale of the process is in the attosecond ( $10^{-18}$  s) domain, which is the natural time scale of atomic processes. In order to grasp the meaning of 18 orders of magnitude in time, one can consider the following. By calling  $\mathcal{U}$  the estimated age of the universe (13.8 billion years [187]), one second corresponds to 2.3 atto $\mathcal{U}$ . Back to the atomic scale, in 20 a photon travels for 6 nm, and an electron of  $E_k = 125$  eV classically travels over a distance that corresponds to the copper atomic radius in the metallic state (1.28 Å, defined as half of the nearest neighbor distance of the *fcc* lattice). Also, one period of electromagnetic radiation with  $h\nu = 130$  eV correspond to 32 as. On a much shorter time scale, i.e. with much less than one cycle, the electromagnetic wave that interacts with the electrons of a solid would not even be well defined.

An intrinsic characteristic of time-resolved experiments is that the time delay of a photoelectron beam from a certain state is measured with respect to a different photoelectron beam, which can be from a reference gas system [47], or a different level of the same system [36, 161], or the very same state but under different experimental geometry [42]. Clearly, the measurement of a finite *relative* time delay suggests the existence of a finite *absolute* time delay of photoemission for each beam, even though this issue has been experimentally addressed only recently and still relies on comparison with theoretical calculations [38, 48].

A different, complementary approach to the chronoscopy of photoemission has been suggested to be through the spin polarization of the photoelectrons [67]. In fact, attosecond time delays in the photoemission process and the spin polarization of photoelectrons are

## Chapter 7. Discussion on EWS time delays in photoemission and concluding remarks

---

both related to the phase information in the matrix elements<sup>1</sup>. The aim of this Thesis was to investigate the relationship between spin polarization and time delay in photoemission from solid state targets, with particular focus on dispersive spin-degenerate states. Both quantities can be modeled by considering the photoemission process as an electron half-scattering process, which highlights the central role of the phase shifts. In particular, in Chapter 4 the relationship between the two phase terms has been shown:  $\phi$ , corresponding to the full matrix element, and  $\phi_s = \phi_2 - \phi_1$ , corresponding to the relative shift between two interfering channels. Correspondingly, the two time delays  $\tau_{EWS}$  and  $\tau_{EWS}^s$  have been introduced. In particular, in Chapter 4 it has been shown how to estimate, under certain assumptions, these two quantities for a dispersive band from the measurement of  $\dot{P}$ , the variation of spin polarization with binding energy, and with an accurate description of the experimental geometry.

Two points need to be clarified about the applicability of this methodology. First, if in a particular case no interference occurs in the matrix element (for example,  $r \rightarrow 0$  or  $r \rightarrow +\infty$ ), then no spin polarization is produced in the photoemission process. The phase term  $\phi_s$  would not be well defined, and therefore  $\tau_{EWS}^s$  neither. However, a time delay might still take place, just it would not be accessible by spin-resolved ARPES. Second, whereas this Thesis has dealt mainly with the case of spin-degenerate initial states, it is possible to extend this approach to the case of spin-polarized states. Interference effects will be concealed though, since they will contribute only to a small degree of polarization when a spin quantization axis is well defined by the physics of the initial state. This remark explains why, whereas SARPES measurement very often confirm on a qualitative level the theoretical predictions made on the physics of the initial state, still a small rotation of the measured spin polarization away from the expected one is quite common. This situation has been outlined in Section 4.6.

Another important comment about the methodology presented in Chapter 4 is that it allows to extract the time information also from non-time-resolved calculations, as long as spin-resolved one-step photoemission calculations are considered. In fact in this case the photoemission matrix elements are fully described, and therefore the phase information is calculated and processed. This can be very powerful when employed on systems that are experimentally difficult to probe with time-resolved or spin-resolved ARPES, and shows in general that it is possible to improve the understandings of photoemission calculation outputs. This approach could prompt further advances in photoemission theory, and experts in one-step photoemission calculations are currently refining their code to access this information [163].

---

<sup>1</sup> The interconnection between *time*, *phase* and *spin* triggers some sort of chicken-or-egg philosophical question. On one side, one could consider the absolute time delay of photoemission as a fundamental property of the process, since it is necessary to have some finite time lag between the initial and the final state, even in the one-step model picture. Then the time delay requires a certain dependence of phases on energy according to Eq. (1.5), and as a consequence they determine a certain spin polarization according to Eqs.(4.1) and (3.32). On the other hand, one could think of the phase term of the matrix element describing the transition to be the fundamental quantity determined by the process, and then, as a consequence, time can be considered as an *emergent* property, at the same level as the spin polarization. This second view, even if less intuitive, has some similarities with other descriptions of the nature of time in different fields [5].



---

It is important to underline the nature of the interfering transitions responsible for the spin polarization. In the case of atomic photoionization, they correspond to the two final partial waves with orbital quantum number  $\ell \rightarrow \ell \pm 1$ . In solids, on the other hand, they are given by two <sup>2</sup> mixed spatial symmetries of the considered state in the double group symmetry representation, both in the initial and final states [147, 150], that are selected by the in-plane and out-of-plane components of the electric field of the light [152]. In any case, the interfering transitions are different photoemission channels which *do not correspond to different photoelectrons*, as in the case of time-resolved experiments, but *they together build up the photoelectron wavefunction*. As analogy, one could think of the well-known double slit experiment: also in this case the interference does not occur for two different particles, but each single particle has a behaviour that is result of the interference of the different possible paths.

An interesting point of view on time delays in photoemission is given by the so-called time-dependent configuration-interaction with single excitations (TDCIS) calculations [188]. It has been shown that the coherence of the hole configurations in atomic attosecond photoionization is strongly affected by pulse duration and energy, as well as by the interaction of the ion with the outgoing electron [189]. This is because the so-called interchannel coupling mechanism [190], i.e. the interference of different ionization channels mediated by the Coulomb interaction with the electron, results in an enhanced entanglement between photoelectron and ionic system, which last for a time delay in the attosecond domain [189]. An equivalent coupling mechanism should occur in dispersive states of a solid, where in addition intrinsic plasmonic satellites [162] might play a role. The interchannel coupling mechanism seems to be a model that goes beyond the sudden approximation of photoemission. However, as discussed in Section 3.1.2, this approximation intervenes only when the photoelectron wavefunction is already formed, or in other words when the photoelectron is not anymore entangled to the system left behind.

At this point it is necessary to discuss the physical meaning of time delay in photoemission, and in particular the two quantities  $\tau_{EWS}^s$  and  $\tau_{EWS}$ . In the three-step model of photoemission, it is easy to identify at least one step where a time delay takes place, that is in the second one. The travel time of the electron during the transport to the surface [161, 162], however, should not be considered in the model for the EWS time delays presented in this Thesis. In fact, the additional logarithmic correction term corresponding to  $\Delta t_n$  in Eq. (1.7) strongly depends on the length traveled by the electron (see Fig. 3.3), however it does not give any contribution to the interfering channels since it takes place only once the photoelectron is formed. This is reflected in the fact that the measured  $\dot{P}$  does not change for different kinetic energies of the electrons, at least within the experimental capabilities, as it is shown in Fig. 5.7 where different photon energies have been used to measure  $P(E_b)$  for the *sp* bulk band of Cu(111). The interpretation of time delays in photoemission is often made in terms of particle

---

<sup>2</sup> A more complex scenario can be considered where more than two channels interfere in the photoemission process. This situation has not been investigated in this Thesis, and it would require the use of Eq. (1.6) instead of Eq. (1.5) for the definition of the time delay, and a modification of Eqs. (4.1) and (3.32) for the description of the phases and the spin polarization, respectively. See also the footnote 1 in Section 4.1.

## Chapter 7. Discussion on EWS time delays in photoemission and concluding remarks

---

trajectories, since the description of EWS time delays can be made in close analogy with classical mechanics [46, 191]. Whereas this approach elucidates the meaning of the EWS formalism, ultimately one should consider that the three-step model and classical trajectories are just a simplification, and as such they should be extended to a fully quantum description.

In this sense, the one-step model is a better candidate, even though it has only been developed for the description of the energetics of the photoemission process and not its dynamics. In fact, it is difficult to tell which process among photon absorption, electron virtual transition and actual photoelectron emission might occur in a finite time. Indeed the influence of the time evolution of the  $E$  field on the phase shifts is under debate [192–194] and there might exist a time-threshold for light absorption. A finite decoherence time required by the wavefunction to be formed in the final state might also be an issue to consider [195]. Lastly, once the final state wavefunction is formed above the vacuum level the electron could spend a finite "sticking" time before reaching the free-particle state. In other words, the final state wavefunction will evolve in time such that the density of probability will move from the absorber site towards the outside of the crystal (in analogy with the tunneling process, where the particle wavefunction is already present on both sides of a potential barrier). The last part seems to be the one that better matches the half-scattering picture, but this separation is only artificial, since the process takes place as a whole.

Mathematically, the two EWS time delays  $\tau_{EWS}^s$  and  $\tau_{EWS}$  should correspond to the time delay between the interfering channels and the time delay of the scattering process in the sense of EWS, respectively. However, as already mentioned, the two interfering partial channels do not correspond to two separate events, but they together form the final photoelectron, and thus the interfering time delay should be associated to the time scale of the whole process. In Refs. [196, 197] it is discussed how an EWS time delay in photoemission only takes into account the pure scattering delay when the whole phase term is considered. Thus  $\tau_{EWS}$  corresponds to  $t_{EWS+C}$  of the scattering model [see Eq. (1.7)]. On the other hand, if an interference phase term is considered, then the time delay can be seen as a formation/release time and not only as a scattering delay. In Refs. [196, 197] the interference is considered between two photon transitions. *It is speculated in this Thesis that the same idea holds for the interfering partial channels of the matrix elements.* Therefore,  $\tau_{EWS}$  accounts for a time delay that is purely due to the (half-)scattering part, whereas  $\tau_{EWS}^s$  is the time delay of the actual photoemission process as a whole. This argument can explain why, in the model of Chapter 4,  $|\tau_{EWS}^s|$  is actually always larger than  $|\tau_{EWS}|$  for  $\phi_s$  within the chosen range  $[-\frac{\pi}{2}, +\frac{\pi}{2}]$ . On the other hand, as mentioned in Section 4.4, there exist the possibility that  $|\tau_{EWS}| > |\tau_{EWS}^s|$  for certain values of  $\dot{r} \neq 0$ , therefore the relationship between the two time delays certainly deserves further theoretical investigations.

The fact that both  $\tau_{EWS}^s$  and  $\tau_{EWS}$  refer to an absolute time scale can be also understood by considering that in Eq.(4.1) the choice  $\phi_1 = 0$  has been made. Both  $\phi$  and  $\phi_s$  are thus defined with respect to the same reference. This reference is such that  $\phi_s = \phi_2$ , which shows that the associated  $\tau_{EWS}^s$  is an intrinsic property of the interfering transitions that together build up the

---

final photoelectron. The possible different signs of all the phases lead to time delays that can be positive or negative. In the electron scattering model, the time delay can indeed be negative, meaning that the process is such that the actually scattered electron leaves the sticking region earlier than an electron that would not feel the scatterer potential. In Section 1.3, however, it has been pointed out that this is true only in the formalism developed by F. Smith, whereas in the approach of L. Eisenbud the choice of the references is always such that the time delays are positive. Anyway this would be certainly correct for the quantity  $\tau_{EWS}$ , whereas  $\tau_{EWS}^s$  should always be positive given the interpretation presented here. In fact the meaning of  $\tau_{EWS}^s < 0$  is just that  $\phi_2 < \phi_1$ , which does not have a direct physical significance. Because of this, and because of the difficulties of carefully determining all the possible sources of a positive or negative sign of the phases in the model and in the experiment, in Chapter 4 only the absolute value of the EWS time delays has been considered.

The main experimental findings of this Thesis, presented in Chapters 5-6, are the following:

- In Cu(111), the  $sp$  bulk-derived band has been considered. The measurement of spin polarization from this spin-degenerate state gives the following estimates of time delays:  $26 \text{ as} \leq |\tau_{EWS}^s| \leq 134 \text{ as}$  and  $11 \text{ as} \leq |\tau_{EWS}| \leq 115 \text{ as}$ . Furthermore, under the assumption that the ratio of the radial term of the interfering matrix elements  $r$  is given by the different projection of the electric field vector of the light onto the sample's surface  $r = E_{\parallel}/E_z$ , one finds  $|\tau_{EWS}^s| \approx 26 \text{ as}$  and  $|\tau_{EWS}| \approx 11 \text{ as}$ . The spin polarization from the  $d$  bands and from the  $3p$  core levels has also been investigated. The results on Cu(111) highlight the presence of a double polarization feature (DPF) in dispersive states, contrary to localized states, which could be interpreted in the lights of self-energy corrections and photoelectron-photohole interaction (see Section 5.2.1).
- The measurements on BSCCO, on the other hand, despite the difficulties of the experiment lead to EWS time delays that are at least three times higher than in Cu(111). The band under consideration was the  $\text{CuO}_2$ -derived state, which is the relevant one for the superconductivity of the material.

The fact that the EWS time delays are larger in the correlated system BSCCO 2212 than in the Fermi liquid system Cu(111) could be due to the enhanced electron correlations in the copper oxide planes of BSCCO. As a coarse explanation, it might be the case that the photoemission of strongly correlated electrons requires a longer "sticking" time before they may enter into quasi-free particle states than those in a simple Fermi liquid system. Further more systematic studies are necessary in order to understand if time delays are indeed affected by correlations. If this would be the case, then the methodology presented in this Thesis will allow to shed light on possible asymmetries of correlations, for example when going from the nodal to the antinodal direction in cuprate superconductors, providing a qualitatively new kind of information in the study of correlated materials and unconventional high- $T_C$  superconductivity. Also the influence of the phase of matter on the time delays needs to be investigated, for example by systematically varying temperature and stoichiometry of the samples.

## **Chapter 7. Discussion on EWS time delays in photoemission and concluding remarks**

---

As a note, self-energy corrections due to electron-quasiparticles coupling might cause an EWS time delay variation within the band, as presented in Appendix B for measurements on a quasi-free-standing monolayer of graphene, which also deserves further more systematic studies.

A clear limit of the indirect access to time delay presented in this Thesis is the necessity of having *quantitative* information about the spin polarization for possibly *all the three spatial components*. Given the extremely low efficiency of spin detectors, the required experiments are highly time-consuming, and therefore a systematic approach will become possible only with the next generation of high efficiency spin detectors [113, 198].

Finally, a possible future development of the project presented in this Thesis is the following. By combining time-resolved techniques with the measurement of spin polarization, one could cross-compare the different estimates of time delays and have a reliable reference for time-zero. An *attosecond- and spin-resolved photoemission experiment* could allow to time the formation of the spin polarization during the photoemission process, tackling the entanglement of the photoelectron with the photohole left in the system, and thus shedding light on the meaning of time delays in quantum mechanics on a very fundamental level.

# A Explicit formulas for the estimate of time delays

## A.1 Atomic photoionization

In atomic photoionization with linearly polarized light, the spin polarization along the direction  $\mathbf{n}$  perpendicular to the reaction plane is given by Eq. (3.31). The explicit expressions of the dynamical parameters  $\beta$  and  $\xi$  are the following [127]:

$$\beta_\ell = \frac{(\ell - 1) + (\ell + 2)r^2 + 6\sqrt{\ell(\ell + 1)}r \cos \phi_s}{(2\ell + 1)(r^2 + 1)}, \quad \xi_{\ell,j} = \frac{3(-1)^{j-\ell-1/2}\sqrt{\ell(\ell + 1)}r \sin \phi_s}{(2j + 1)(r^2 + 1)}. \quad (\text{A.1})$$

It has to be mentioned that  $\xi$  differs by a factor of  $-2$  when compared to other references [64].

If one would apply the model presented in Chapter 4 in order to estimate EWS time delays in atomic photoionization, it would be necessary to evaluate the expression  $\frac{dP}{d\phi_s}$  and  $\frac{dP}{dr}$ . They are given by

$$\frac{dP_{\ell,j}(r, \phi_s, \gamma)}{d\phi_s} = \Upsilon_{\phi_s}^j \frac{N_{\phi_s}}{D}, \quad \frac{dP_{\ell,j}(r, \phi_s, \gamma)}{dr} = \Upsilon_r^j \frac{N_r}{D}, \quad (\text{A.2})$$

with the following substitutions:

$$\begin{aligned} N_{\phi_s} &= (2\ell + 1)r \sin 2\gamma \left\{ \cos 2\gamma \left[ \sqrt{\ell(\ell + 1)}(\ell + (\ell + 2)r^2 - 1) \cos \phi_s + 6\ell(\ell + 1)r \right] + \sqrt{\ell(\ell + 1)} \left[ 3\ell + (3\ell + 2)r^2 + 1 \right] \cos \phi_s + 2\ell(\ell + 1)r \right\}, \\ N_r &= (2\ell + 1) \sin 2\gamma \sin \phi_s \left\{ \cos \gamma^2 \left[ 1 - \ell + (\ell + 2)r^2 \right] + \ell(r^2 - 1) - 1 \right\}, \\ D &= \left\{ \ell + \cos \gamma^2 \left[ \ell + (\ell + 2)r^2 + 6\sqrt{\ell(\ell + 1)}r \cos \phi_s - 1 \right] + \ell r^2 - 2\sqrt{\ell(\ell + 1)}r \cos \phi_s + 1 \right\}^2, \\ \Upsilon_{\phi_s}^{\ell-1/2} &= -\frac{1}{2\ell}, \\ \Upsilon_{\phi_s}^{\ell+1/2} &= +\frac{1}{2(\ell + 1)}, \\ \Upsilon_r^{\ell-1/2} &= +\frac{\sqrt{\ell(\ell + 1)}}{\ell}, \\ \Upsilon_r^{\ell+1/2} &= -\frac{\ell}{\sqrt{\ell(\ell + 1)}}. \end{aligned}$$

## A.2 Solid state photoemission

In Chapter 4 several functions have been defined but not calculated, since they are lengthy and not very insightful in their explicit form. For completeness, they are reported in the following. By deriving Eq. (4.1) with respect to kinetic energy one obtains eq. (4.13), where the two functions  $w(r, \phi_s)$  and  $w'(r, \phi_s)$  are given by:

$$w(r, \phi_s) \doteq \frac{r(r + \cos \phi_s)}{1 + 2r \cos \phi_s + r^2}, \quad w'(r, \phi_s) \doteq \frac{\sin \phi_s}{1 + 2r \cos \phi_s + r^2}. \quad (\text{A.3})$$

In Eq. (4.7) the function  $c(r, t)$  has been defined, such that  $P = c(r, t) \sin \phi_s$ . In the expressions for the estimates of the EWS time delays, it is necessary to evaluate the derivatives  $dP/d\phi_s$  and  $dP/dr$ . They are given by:

$$\frac{dP}{d\phi_s} = c(r, t) \frac{d \sin \phi_s}{d\phi_s} = \frac{-4t(1-t^2)r}{4t^2 + r^2(1-t^2)^2} \cos \phi_s, \quad (\text{A.4})$$

$$\frac{dP}{dr} = \frac{dc(r, t)}{dr} \sin \phi_s = \frac{-4t(1-t^2) \left[ 4t^2 - r^2(1-t^2)^2 \right]}{\left[ 4t^2 + r^2(1-t^2)^2 \right]^2} \sin \phi_s. \quad (\text{A.5})$$

The function  $m \doteq (dP/d\phi_s)/w$  is introduced in Eq. (4.11) for the estimate of  $|\tau_{EWS}|$ . Its full expression is given by:

$$m(r, \phi_s, t) = \frac{-4t \cos \phi_s (1-t^2) (1+2r \cos \phi_s + r^2)}{(r + \cos \phi_s) \left[ 4t^2 + r^2(1-t^2)^2 \right]}. \quad (\text{A.6})$$

Finally, Eqs. (4.9) and (4.13) give the expressions for  $\tau_{EWS}^s$  and  $\tau_{EWS}$ . By combining all the previous equations, one obtains the following explicit forms:

$$\tau_{EWS}^s = \hbar \dot{P} \frac{4t^2 + r^2(1-t^2)^2}{4rt(1-t^2)} \sec \phi_s + \hbar \dot{r} \frac{4t^2 - r^2(1-t^2)^2}{r \left[ 4t^2 + r^2(1-t^2)^2 \right]} \tan \phi_s, \quad (\text{A.7})$$

$$\tau_{EWS} = \frac{\left[ 4t^2 + r^2(1-t^2)^2 \right] (r + \cos \phi_s) \sec \phi_s}{4t(1-t^2)(1+2r \cos \phi_s + r^2)} \left\{ \hbar \dot{P} + \hbar \dot{r} \frac{4rt(1-t^2) \left[ 4t^2 - r^2(1-t^2)^2 - 2r(1-t^2)^2 \cos \phi_s \right] \sin \phi_s}{(r + \cos \phi_s) \left[ 4t^2 + r^2(1-t^2)^2 \right]^2} \right\}, \quad (\text{A.8})$$

where the dependence on  $\dot{P}$  and  $\dot{r}$  has been highlighted. As an example, for  $t = 0.28$ ,  $r = 0.67$  and  $\phi_s = 0.1$  these last two equations yield  $\tau_{EWS}^s \approx \hbar \dot{P} - 0.01 \hbar \dot{r}$  and  $\tau_{EWS} \approx 0.4 \tau_{EWS}^s$ , as plotted in Fig. 4.4(b) for  $\dot{P} = 0.04 \text{ eV}^{-1}$ .

## B Further studies: quasi-free-standing graphene monolayer

In this Appendix further studies of the spin polarization from spin-degenerate states will be briefly presented for another model system: a monolayer of graphene. Graphene is a well-known bidimensional material which has become the paradigm for studying low dimensionality in condensed matter physics [199]. From the perspective of photoemission, it is a gapless semiconductor with conical conduction and valence bands, which meet at the Fermi energy at the six  $K$  points of the Brillouin Zone. This results in the famous Dirac cone-like linear dispersion with vanishing density of states at Fermi. The photoemission intensity in graphene is known to be strongly dependent on light polarization and photon energy, because of an interference process between the two equivalent atomic site in the honeycomb lattice. This results in the so-called *dark corridor* of graphene, for which only one part of the cone is visible [200].

The sample measured at COPHEE was a H intercalated quasi-free-standing monolayer of graphene on SiC substrate, which has been provided by Florian Speck and Thomas Seyller from the Technische Universität of Chemnitz. The results are summarized in Fig. B.1. In panel (a) the photoemission intensity measured at COPHEE is shown for  $\pi$  polarized light of  $h\nu = 56$  eV. Only the portion of the cone at  $k < k_D$  is visible, whereas the other half is completely suppressed. In panels (c)-(e) the spin polarization plots of the bandmap for the  $x$ ,  $y$  and  $z$  spatial directions are shown respectively, multiplied by the total intensity to better display the features. Also in this case, a DPF is observed in the spin signal. To be noted how the step size in binding energy is much smaller than the other measurements presented in this Thesis, thanks to the extremely high cross-section of graphene at this photon energy. Also, it has to be mentioned that the asymmetry for the  $y_M$  component is not the one measured by the dedicated detectors at COPHEE but is obtained from Eq. (3.25). In panel (b) the total spin polarization is shown, where red lines indicate the cuts of the bandmap that are shown in the stacked plot in panel (f). These curves (which are neither EDCs nor MDCs) show the spin polarization through the band (i.e. along lines that are parallel to the linear dispersion of the band), so that they can be directly used for an estimate of  $|\tau_{EWS}^s| \geq \hbar |\dot{P}|$  according to Eq. (4.10).



## Appendix B. Further studies: quasi-free-standing graphene monolayer

Interestingly, the dependence of  $P(E_b)$  is not simply linear for different cuts, but can be split into two different lines with opposite slope, as indicated by an arrow in the cut shown in red in panel (f), which corresponds to the maximum of the photoemission intensity peak. In this cut, for example, the part deeper in energy gives a slope of  $0.05 \text{ eV}^{-1}$ . This value is very similar to the one found for the free-electron-like  $sp$  bulk band of Cu(111) in Chapter 5. On the other hand, the part closer to the Dirac point has a much higher absolute slope of  $0.24 \text{ eV}^{-1}$ , which corresponds to  $|\tau_{EWS}^s| \geq 160 \text{ as}$ . Further systematic studies are required to understand this change of slope at about  $E_b = 400 \text{ meV}$ , but this could be interpreted in the light of the different energy scale of electron-electron, electron-plasmon and electron-phonon coupling [201]. Also, this observation might help to better understand the nature of the DPE.

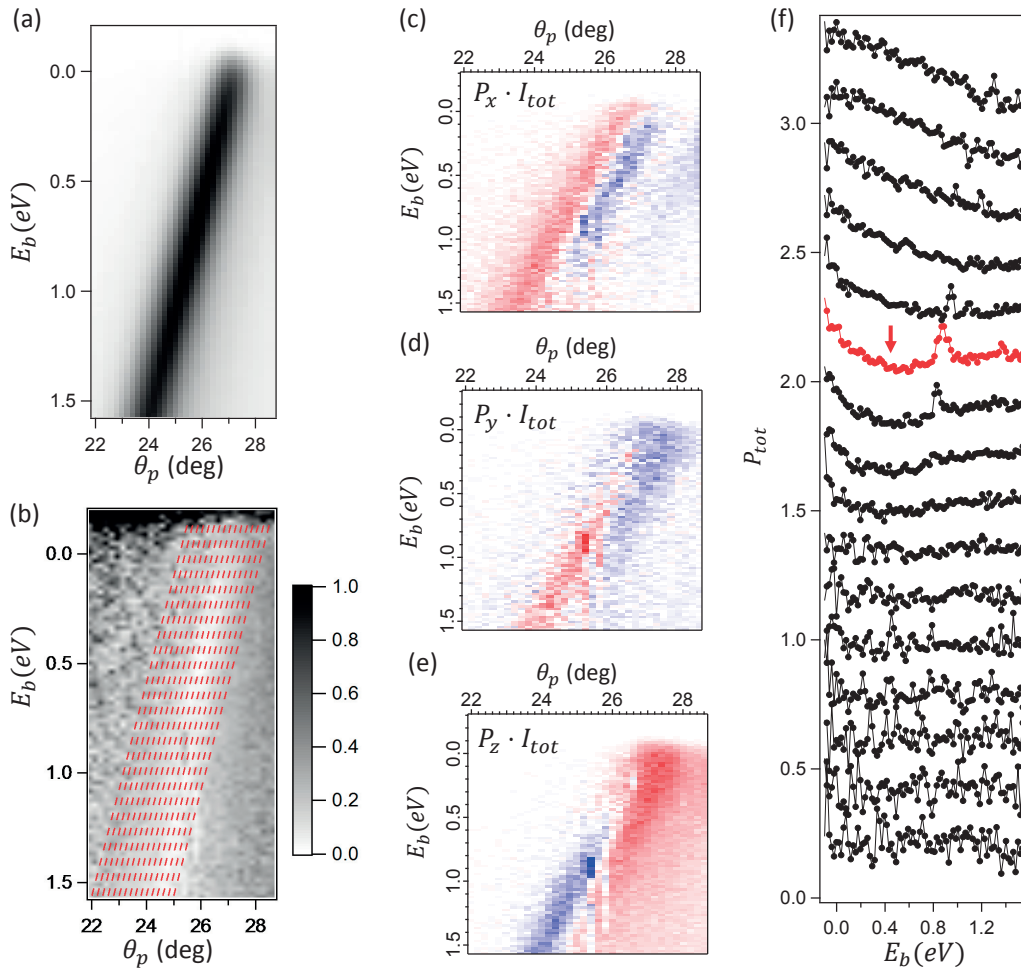


Figure B.1: (a) Linear dispersion of graphene, probed with  $\pi$  polarized light of  $h\nu = 56 \text{ eV}$ . (b) Total spin polarization  $P$  of the bandmap. The corresponding spin polarization components along the  $x$ ,  $y$  and  $z$  directions are shown in (c)-(e), respectively. (f) Total spin polarization  $P$  evaluated along the red lines of (b), where the curves from bottom to top correspond to the lines from left to right. The curve in red corresponds to the line passing through the maximum of the photoemission intensity peak. The sharp peak at  $\approx 0.9 \text{ eV}$  is a measurement glitch, as can be seen in (c)-(e). The arrow indicates a change of slope.



# Bibliography

- [1] Anaximander. Fr. 12, B1 (Simplicius). Mid-6th century B.C.
- [2] Aristotle. *Physics*, ca. 322 B.C.
- [3] Plato. *Timaeus*, ca. 360 B.C.
- [4] Tony Roark. *Aristotle on Time: a study of the physics*. Cambridge University Press, 2011.
- [5] Carlo Rovelli. *The order of time*. Allen Lane, 2018.
- [6] Wolfgang Pauli. *Die allgemeine prinzipien der wellenmechanik*. Springer, Berlin, 1933.
- [7] Paul Busch. On the Energy-Time Uncertainty Relation. Part I: Dynamical Time and Time Indeterminacy. *Foundations of Physics*, 20(1):1–32, 1990.
- [8] Gordon N. Fleming. Time in quantum mechanics. *Studies in History and Philosophy of Science Part B: Studies in History and Philosophy of Modern Physics*, 36(1):181–190, 2005.
- [9] David Griffiths. *Introduction to quantum mechanics*. Prentice Hall, Englewood Cliffs, N.J., 1995.
- [10] L. Mandelstam and I. Tamm. *The Uncertainty Relation Between Energy and Time in Non-relativistic Quantum Mechanics*, pages 115–123. Springer Berlin Heidelberg, Berlin, Heidelberg, 1991.
- [11] Jan Hilgevoord. Time in quantum mechanics: a story of confusion. *Studies in History and Philosophy of Science Part B: Studies in History and Philosophy of Modern Physics*, 36(1):29–60, 2005.
- [12] Massimiliano Sassoli de Bianchi. Time-delay of classical and quantum scattering processes: a conceptual overview and a general definition. *Open Physics*, 10:282, 2012.
- [13] J.G. Muga, R. Sala Mayato, and Í. L. Egusquiza, editors. *Time in Quantum Mechanics*, volume 734 of *Lecture Notes in Physics*. Springer Berlin Heidelberg, Berlin, Heidelberg, 2007.
- [14] E. Schrödinger. Are there quantum jumps? Part II. *The British Journal for the Philosophy of Science*, III(11):233–242, 1952.
- [15] Bhart-Anjan S. Bhullar, Zachary S. Morris, Elizabeth M. Sefton, Atalay Tok, Masayoshi Tokita, Bumjin Namkoong, Jasmin Camacho, David A. Burnham, and Arhat Abzhanov. A molecular mechanism for the origin of a key evolutionary innovation, the bird beak and palate, revealed by an integrative approach to major transitions in vertebrate history. *Evolution*, 69(7):1665–1677, 2015.
- [16] C. N. Yang. On Quantized Space-Time. *Phys. Rev.*, 72(9):874, 1947.
- [17] P. Caldirola. The introduction of the chronon in the electron theory and a charged-Lepton mass formula. *Lettere al Nuovo Cimento (1971-1985)*, 27(8):225–228, 1980.
- [18] Matthias F. Kling and Marc J. J. Vrakking. Attosecond electron dynamics. *Annual review of physical chemistry*, 59:463–492, 2008.
- [19] J. M. Dahlström, A. L’Huillier, and A. Maquet. Introduction to attosecond delays in photoionization. *Journal of Physics B: Atomic, Molecular and Optical Physics*, 45(18):183001, 2012.
- [20] Luis Plaja, Ricardo Torres, and Amelle Zaïr, editors. *Attosecond Physics*, volume 177 of *Springer Series in Optical Sciences*. Springer, Berlin, Heidelberg, 2013.

## Bibliography

---

- [21] Alfred Maquet, Jérémie Caillat, and Richard Taïeb. Attosecond delays in photoionization: time and quantum mechanics. *Journal of Physics B: Atomic, Molecular and Optical Physics*, 47(20):204004, 2014.
- [22] Renate Pazourek, Stefan Nagele, and Joachim Burgdörfer. Attosecond chronoscopy of photoemission. *Rev. Mod. Phys.*, 87(3):765–802, 2015.
- [23] David Ayuso, Alvaro Jiménez-Galán, Felipe Morales, Misha Ivanov, and Olga Smirnova. Attosecond control of spin polarization in electron–ion recollision driven by intense tailored fields. *New Journal of Physics*, 19(7):73007, 2017.
- [24] M. Büttiker and R. Landauer. Traversal Time for Tunneling. *Phys. Rev. Lett.*, 49(23):1739–1742, 1982.
- [25] P. Eckle, A. N. Pfeiffer, C. Cirelli, A. Staudte, R. Dörner, H. G. Muller, M. Büttiker, and U. Keller. Attosecond Ionization and Tunneling Delay Time Measurements in Helium. *Science*, 322(5907):1525–1529, 2008.
- [26] Adrian N. Pfeiffer, Claudio Cirelli, Mathias Smolarski, Darko Dimitrovski, Mahmoud Abu-samha, Lars Bojer Madsen, and Ursula Keller. Attoclock reveals natural coordinates of the laser-induced tunnelling current flow in atoms. *Nature Physics*, 8:76, 2011.
- [27] Enderalp Yakaboylu, Michael Klaiber, and Karen Z. Hatsagortsyan. Wigner time delay for tunneling ionization via the electron propagator. *Phys. Rev. A*, 90(1):12116, 2014.
- [28] Alexandra S. Landsman, Matthias Weger, Jochen Maurer, Robert Boge, André Ludwig, Sebastian Heuser, Claudio Cirelli, Lukas Gallmann, and Ursula Keller. Ultrafast resolution of tunneling delay time. *Optica*, 1(5):343–349, 2014.
- [29] Alexandra S. Landsman and Ursula Keller. Attosecond science and the tunnelling time problem. *Physics Reports*, 547:1–24, 2015.
- [30] Minghu Yuan, PeiPei Xin, TianShu Chu, and HongPing Liu. Exploring tunneling time by instantaneous ionization rate in strong-field ionization. *Opt. Express*, 25(19):23493–23501, 2017.
- [31] M. Hentschel, R. Kienberger, Ch. Spielmann, G. A. Reider, N. Milosevic, T. Brabec, P. Corkum, U. Heinzmann, M. Drescher, and F. Krausz. Attosecond metrology. *Nature*, 414(6863):509–513, 2001.
- [32] P. M. Paul, E. S. Toma, P. Breger, G. Mullot, F. Augé, Ph. Balcou, H. G. Muller, and P. Agostini. Observation of a Train of Attosecond Pulses from High Harmonic Generation. *Science*, 292(5522):1689–1692, 2001.
- [33] Markus Drescher, Michael Hentschel, Reinhard Kienberger, Gabriel Tempea, Christian Spielmann, Georg A. Reider, Paul B. Corkum, and Ferenc Krausz. X-ray Pulses Approaching the Attosecond Frontier. *Science*, 291(5510):1923–1927, 2001.
- [34] L. Cattaneo, J. Vos, M. Lucchini, L. Gallmann, C. Cirelli, and U. Keller. Comparison of attosecond streaking and RABBITT. *Opt. Express*, 24(25):29060–29076, 2016.
- [35] R. Kienberger, E. Goulielmakis, M. Uiberacker, A. Baltuska, V. Yakovlev, F. Bammer, A. Scrinzi, Th. Westerwalbesloh, U. Kleineberg, U. Heinzmann, M. Drescher, and F. Krausz. Atomic transient recorder. *Nature*, 427(6977):817–821, 2004.
- [36] A. L. Cavalieri, N. Muller, Th. Uphues, V. S. Yakovlev, A. Baltuska, B. Horvath, B. Schmidt, L. Blumel, R. Holzwarth, S. Hendel, M. Drescher, U. Kleineberg, P. M. Echenique, R. Kienberger, F. Krausz, and U. Heinzmann. Attosecond spectroscopy in condensed matter. *Nature*, 449(7165):1029–1032, 2007.
- [37] M. Schultze, M. Fieß, N. Karpowicz, J. Gagnon, M. Korbman, M. Hofstetter, S. Neppl, A. L. Cavalieri, Y. Komninos, Th. Mercouris, C. A. Nicolaides, R. Pazourek, S. Nagele, J. Feist, J. Burgdörfer, A. M. Azzeer, R. Ernstorfer, R. Kienberger, U. Kleineberg, E. Goulielmakis, F. Krausz, and V. S. Yakovlev. Delay in Photoemission. *Science*, 328(5986):1658–1662, 2010.
- [38] M. Ossiander, F. Siegrist, V. Shirvanyan, R. Pazourek, A. Sommer, T. Latka, A. Guggenmos, S. Nagele, J. Feist, J. Burgdorfer, R. Kienberger, and M. Schultze. Attosecond correlation dynamics. *Nat. Phys.*, 2016.
- [39] H. G. Muller. Reconstruction of attosecond harmonic beating by interference of two-photon transitions. *Applied Physics B*, 74(1):17–21, 2002.
- [40] Johan Mauritsson, Mette B. Gaarde, and Kenneth J. Schafer. Accessing properties of electron wave packets generated by attosecond pulse trains through time-dependent calculations. *Phys. Rev. A*, 72(1):13401, 2005.

- 
- [41] C. Palatchi, J. M. Dahlström, A. S. Kheifets, I. A. Ivanov, D. M. Canaday, P. Agostini, and L. F. Di Mauro. Atomic delay in helium, neon, argon and krypton. *Journal of Physics B: Atomic, Molecular and Optical Physics*, 47(24):245003, 2014.
- [42] M. Lucchini, L. Castiglioni, L. Kasmi, P. Kliuiev, A. Ludwig, M. Greif, J. Osterwalder, M. Hengsberger, L. Gallmann, and U. Keller. Light-Matter Interaction at Surfaces in the Spatiotemporal Limit of Macroscopic Models. *Phys. Rev. Lett.*, 115(13):137401, 2015.
- [43] M. Quack and F. Merkt, editors. *Handbook of High-resolution Spectroscopy - Vol. 3*. John Wiley & Sons, 2011.
- [44] Petrisa Eckle, Mathias Smolarski, Philip Schlup, Jens Biegert, André Staudte, Markus Schöffler, Harm G. Muller, Reinhard Dörner, and Ursula Keller. Attosecond angular streaking. *Nature Physics*, 4(7):565–570, 2008.
- [45] Adrian N. Pfeiffer, Claudio Cirelli, Mathias Smolarski, and Ursula Keller. Recent attoclock measurements of strong field ionization. *Chemical Physics*, 414(Supplement C):84–91, 2013.
- [46] Fabian Siek, Sergej Neb, Peter Bartz, Matthias Hensen, Christian Strüber, Sebastian Fiechter, Miquel Torrent-Sucarrat, Vyacheslav M. Silkin, Eugene E. Krasovskii, Nikolay M Kabachnik, Stephan Fritzsche, Ricardo Díez Muiño, Pedro M. Echenique, Andrey K. Kazansky, Norbert Müller, Walter Pfeiffer, and Ulrich Heinzmann. Angular momentum-induced delays in solid-state photoemission enhanced by intra-atomic interactions. *Science*, 357(6357):1274–1277, 2017.
- [47] Reto Locher, Luca Castiglioni, Matteo Lucchini, Michael Greif, Lukas Gallmann, Jürg Osterwalder, Matthias Hengsberger, and Ursula Keller. Energy-dependent photoemission delays from noble metal surfaces by attosecond interferometry. *Optica*, 2(5):405–410, 2015.
- [48] S. Neppl, R. Ernstorfer, A. L. Cavalieri, C. Lemell, G. Wachter, E. Magerl, E. M. Bothschafter, M. Jobst, M. Hofstetter, U. Kleineberg, J. V. Barth, D. Menzel, J. Burgdorfer, P. Feulner, F. Krausz, and R. Kienberger. Direct observation of electron propagation and dielectric screening on the atomic length scale. *Nature*, 517(7534):342–346, 2015.
- [49] Leonard Eisenbud. *Ph.D. thesis, Formal properties of nuclear collisions*. Unpublished, Princeton University, 1948.
- [50] Eugene P. Wigner. Lower Limit for the Energy Derivative of the Scattering Phase Shift. *Phys. Rev.*, 98(1):145–147, 1955.
- [51] Felix T. Smith. Lifetime Matrix in Collision Theory. *Phys. Rev.*, 118(1):349–356, 1960.
- [52] Helmut Haberzettl and Ron Workman. Time delay in a multichannel formalism. *Phys. Rev. C*, 76(5):58201, 2007.
- [53] John D. Dollard. Asymptotic Convergence and the Coulomb Interaction. *Journal of Mathematical Physics*, 5(6), 1964.
- [54] D. Bollé, F. Gesztesy, and H. Grosse. Time delay for long-range interactions. *Journal of Mathematical Physics*, 24(6):1529–1541, 1983.
- [55] Robert Eisberg and Robert Resnick. *Quantum Physics of atoms, molecules, solids, nuclei and particles*. John Wiley & Sons, New York, 2nd edition, 1985.
- [56] Keh-Ning Huang. Theory of angular distribution and spin polarization of photoelectrons. *Phys. Rev. A*, 22(1):223–239, 1980.
- [57] Z.-M Wang and D. S. Elliott. Determination of the Phase Difference between Even and Odd Continuum Wave Functions in Atoms through Quantum Interference Measurements. *Phys. Rev. Lett.*, 87(17):173001, 2001.
- [58] T. Barillot, C. Cauchy, P.-A. Hervieux, M. Gisselbrecht, S. E. Canton, P. Johnsson, J. Laksman, E. P. Mansson, J. M. Dahlström, M. Magrakvelidze, G. Dixit, M. E. Madjet, H. S. Chakraborty, E. Suraud, P. M. Dinh, P. Wopperer, K. Hansen, V. Loriot, C. Bordas, S. Sorensen, and F. Lépine. Angular asymmetry and attosecond time delay from the giant plasmon resonance in C60 photoionization. *Phys. Rev. A*, 91(3):33413, 2015.

## Bibliography

---

- [59] P. Hockett, E. Frumker, D. M. Villeneuve, and P. B. Corkum. Time delay in molecular photoionization. *Journal of Physics B: Atomic, Molecular and Optical Physics*, 49(9):95602, 2016.
- [60] Hiroshi Daimon, Takeshi Nakatani, Shin Imada, and Shigemasa Suga. Circular dichroism from non-chiral and non-magnetic materials observed with display-type spherical mirror analyzer. *Journal of Electron Spectroscopy and Related Phenomena*, 76(Supplement C):55–62, 1995.
- [61] M. Wießner, D. Hauschild, C. Sauer, V. Feyer, A. Schöll, and F. Reinert. Complete determination of molecular orbitals by measurement of phase symmetry and electron density. *Nature Communications*, 5:4156, 2014.
- [62] J. Kessler. *Polarized Electrons, 2nd edition*. Springer, Berlin Heidelberg, 1985.
- [63] U. Heinzmann. Experimental determination of the phase differences of continuum wavefunctions describing the photoionisation process of xenon atoms. Part I. Measurements of the spin polarisations of photoelectrons and their comparison with theoretical results. *Journal of Physics B: Atomic and Molecular Physics*, 13(22):4353, 1980.
- [64] U. Heinzmann. Experimental determination of the phase differences of continuum wavefunctions describing the photoionisation process of xenon atoms. Part II. Evaluation of the matrix elements and the phase differences and their comparison with data in the discrete spect. *Journal of Physics B: Atomic and Molecular Physics*, 13(22):4367, 1980.
- [65] N. Irmer, F. Frentzen, R. David, P. Stoppmanns, B. Schmiedeskamp, and U. Heinzmann. Photon energy dependence of spin-resolved photoemission spectra in normal emission from Pt(110) by linearly polarized light. *Surface Science*, 331:1147–1151, 1995.
- [66] C. Roth, F. U. Hillebrecht, W. G. Park, H. B. Rose, and E. Kisker. Spin Polarization in Cu Core-Level Photoemission with Linearly Polarized Soft X Rays. *Phys. Rev. Lett.*, 73(14):1963–1966, 1994.
- [67] Ulrich Heinzmann and J. Hugo Dil. Spin–orbit-induced photoelectron spin polarization in angle-resolved photoemission from both atomic and condensed matter targets. *Journal of Physics: Condensed Matter*, 24(17):173001, 2012.
- [68] Walther Gerlach and Otto Stern. Das magnetische Moment des Silberatoms. *Zeitschrift für Physik A Hadrons and Nuclei*, 9(1):353–355, 1922.
- [69] Bretislav Friedrich and Dudley Herschbach. Stern and Gerlach: How a Bad Cigar Helped Reorient Atomic Physics. *Physics Today*, 56(12):53–59, 2003.
- [70] G. E. Uhlenbeck and S. Goudsmit. Spinning Electrons and the Structure of Spectra. *Nature*, 117:264, 1926.
- [71] T. E. Phipps and J. B. Taylor. The Magnetic Moment of the Hydrogen Atom. *Phys. Rev.*, 29(2):309–320, 1927.
- [72] Hans C. Ohanian. What is spin? *American Journal of Physics*, 54(6):500–505, 1986.
- [73] F. J. Belinfante. On the spin angular momentum of mesons. *Physica*, 6(7):887–898, 1939.
- [74] W. Gordon. Der Strom der Diracschen Elektronentheorie. *Zeitschrift für Physik*, 50(9):630–632, 1928.
- [75] K. Blum. *Density Matrix Theory and Applications*. Springer Berlin Heidelberg, 3rd edition, 2012.
- [76] Noah Sherman. Coulomb Scattering of Relativistic Electrons by Point Nuclei. *Phys. Rev.*, 103(6):1601–1607, 1956.
- [77] J. W. Motz, H. Olsen, and H. W. Koch. Electron Scattering without Atomic or Nuclear Excitation. *Rev. Mod. Phys.*, 36(4):881–928, 1964.
- [78] G. Holzwarth and H. J. Meister. *Tables of asymmetry, cross-section, and related functions for Mott scattering of electrons by screened gold and mercury nuclei*. Inst. für Theoretische Physik d. Univ. München, 1964.
- [79] V. N. Petrov, V. V. Grebenshikov, B. D. Grachev, and A. S. Kamochkin. New compact classical 40 kV Mott polarimeter. *Review of Scientific Instruments*, 74(3):1278–1281, 2003.
- [80] Heinrich Hertz. Ueber den Einfluss des ultravioletten Lichtes auf die elektrische Entladung. *Ann. Phys.*, 31(983), 1987.
- [81] H. P. Bonzel and Ch. Kleint. On the history of photoemission. *Progress in Surface Science*, 48(1-4):179, 1995.

- [82] A. Einstein. Ueber einen die Erzeugung und Verwandlung des Lichtes betreffenden heuristischen Gesichtspunkt [Annalen der Physik 17, 132 (1905)]. *Annalen der Physik*, 14(S1):164–181, 2005.
- [83] R. A. Millikan. A Direct Determination of  $h$ . *Phys. Rev.*, 4(1):73–75, 1914.
- [84] M. P. Seah and W. A. Dench. Quantitative electron spectroscopy of surfaces: A standard data base for electron inelastic mean free paths in solids. *Surface and Interface Analysis*, 1(1):2–11, 1979.
- [85] Andrea Damascelli. Probing the Electronic Structure of Complex Systems by ARPES. *Physica Scripta*, 2004(T109):61, 2004.
- [86] S. Hüfner. *Photoelectron Spectroscopy: Principles and Applications*, 3rd edn. Springer, Berlin Heidelberg New York, 2003.
- [87] M. Grioni. *Photoelectron Spectroscopy*, pages 189–237. Springer Netherlands, Dordrecht, 2006.
- [88] H. Lüth. *Solid surfaces, interfaces and thin films*. Springer, Berlin Heidelberg, 4th edition, 2001.
- [89] C. N. Berglund and W. E. Spicer. Photoemission Studies of Copper and Silver: Theory. *Phys. Rev.*, 136(4A):1030–1044, 1964.
- [90] C. N. Berglund and W. E. Spicer. Photoemission Studies of Copper and Silver: Experiment. *Phys. Rev.*, 136(4A):1044–1064, 1964.
- [91] P. J. Feibelman and D. E. Eastman. Photoemission spectroscopy - Correspondence between quantum theory and experimental phenomenology. *Phys. Rev. B*, 10(12):4932–4947, 1974.
- [92] J. B. Pendry and J. F. L. Hopkinson. Theory of photoemission. *Le Journal de Physique Colloques*, 39(C4):C4–142–C4–148, 1978.
- [93] R. Courths and S. Hüfner. Photoemission experiments on copper. *Physics Reports*, 112(2):53–171, 1984.
- [94] G. Borstel. Theoretical aspects of photoemission. *Applied Physics A*, 38(3):193–204, 1985.
- [95] J. Braun. The theory of angle-resolved ultraviolet photoemission and its applications to ordered materials. *Reports on Progress in Physics*, 59(10):1267–1338, 1996.
- [96] H. Ebert, D. Ködderitzsch, and J. Minár. Calculating condensed matter properties using the KKR-Green's function method - recent developments and applications. *Reports on Progress in Physics*, 74(9):096501, 2011.
- [97] J. Minár, J. Braun, S. Mankovsky, and H. Ebert. Calculation of angle-resolved photo emission spectra within the one-step model of photo emission - Recent developments. *Journal of Electron Spectroscopy and Related Phenomena*, 184(3-6):91–99, 2011.
- [98] J. Braun, K. Miyamoto, A. Kimura, T. Okuda, M. Donath, H. Ebert, and J. Minár. Exceptional behavior of d-like surface resonances on W(110): the one-step model in its density matrix formulation. *New Journal of Physics*, 16(1):15005, 2014.
- [99] Simon Moser. An experimentalist's guide to the matrix element in angle resolved photoemission. *Journal of Electron Spectroscopy and Related Phenomena*, 214:29–52, 2017.
- [100] M. Bauer, A. Marienfeld, and M. Aeschlimann. Hot electron lifetimes in metals probed by time-resolved two-photon photoemission. *Progress in Surface Science*, 90(3):319–376, 2015.
- [101] Lars Hedin, John Michiels, and John Inglesfield. Transition from the adiabatic to the sudden limit in core-electron photoemission. *Phys. Rev. B*, 58(23):15565–15582, 1998.
- [102] M. Hoesch, T. Greber, V. N. Petrov, M. Muntwiler, M. Hengsberger, W. Auwaerter, and J. Osterwalder. Spin-polarized Fermi surface mapping. *Journal of Electron Spectroscopy and Related Phenomena*, 124(2-3):263–279, 2002.
- [103] J. Hugo Dil. Spin and angle resolved photoemission on non-magnetic low-dimensional systems. *Journal of Physics: Condensed Matter*, 21(40):403001, 2009.
- [104] B. M. Garraway and S. Stenholm. Does a flying electron spin? *Contemporary Physics*, 43(3):147–160, 2002.
- [105] Taichi Okuda. Recent trends in spin-resolved photoelectron spectroscopy. *Journal of Physics: Condensed Matter*, 29(48):483001, 2017.



## Bibliography

---

- [106] Taichi Okuda, Koji Miyamoto, Akio Kimura, Hirofumi Namatame, and Masaki Taniguchi. A double VLEED spin detector for high-resolution three dimensional spin vectorial analysis of anisotropic Rashba spin splitting. *Journal of Electron Spectroscopy and Related Phenomena*, 201(Supplement C):23–29, 2015.
- [107] Koichiro Yaji, Ayumi Harasawa, Kenta Kuroda, Sogen Toyohisa, Mitsuhiro Nakayama, Yukiaki Ishida, Akiko Fukushima, Shuntaro Watanabe, Chuangtian Chen, Fumio Komori, and Shik Shin. High-resolution three-dimensional spin- and angle-resolved photoelectron spectrometer using vacuum ultraviolet laser light. *Review of Scientific Instruments*, 87(5):53111, 2016.
- [108] Chiara Bigi, Pranab K. Das, Davide Benedetti, Federico Salvador, Damjan Krizmancic, Rudi Sergo, Andrea Martin, Giancarlo Panaccione, Giorgio Rossi, Jun Fujii, and Ivana Vobornik. Very efficient spin polarization analysis (VESPA): new exchange scattering-based setup for spin-resolved ARPES at APE-NFFA beamline at Elettra. *Journal of Synchrotron Radiation*, 24(4):750–756, 2017.
- [109] J. Kirschner and R. Feder. Spin Polarization in Double Diffraction of Low-Energy Electrons from W(001): Experiment and Theory. *Phys. Rev. Lett.*, 42(15):1008–1011, 1979.
- [110] D. Vasilyev, C. Tusche, F. Giebels, H. Gollisch, R. Feder, and J. Kirschner. Low-energy electron reflection from Au-passivated Ir(001) for application in imaging spin-filters. *Journal of Electron Spectroscopy and Related Phenomena*, 199:10–18, 2015.
- [111] D. Kutnyakhov, P. Lushchik, A. Fognini, D. Perriard, M. Kolbe, K Medjanik, E. Fedchenko, S. A. Nepijko, H. J. Elmers, G. Salvatella, C. Stieger, R. Gort, T. Bähler, T. Michlmayer, Y. Acremann, A. Vaterlaus, F. Giebels, H. Gollisch, R. Feder, C. Tusche, A. Krasnyuk, J. Kirschner, and G. Schönhense. Imaging spin filter for electrons based on specular reflection from iridium (001). *Ultramicroscopy*, 130(Supplement C):63–69, 2013.
- [112] Gerd Schönhense, Katerina Medjanik, and Hans-Joachim Elmers. Space-, time- and spin-resolved photoemission. *Journal of Electron Spectroscopy and Related Phenomena*, 200(Supplement C):94–118, 2015.
- [113] Vladimir N. Strocov, Vladimir N. Petrov, and J. Hugo Dil. Concept of a multichannel spin-resolving electron analyzer based on Mott scattering. *Journal of Synchrotron Radiation*, 22(3):708–716, 2015.
- [114] V. N. Petrov, M. Landolt, M. S. Galaktionov, and B. V. Yushenkov. A new compact 60 kV Mott polarimeter for spin polarized electron spectroscopy. *Review of Scientific Instruments*, 68(12):4385–4389, 1997.
- [115] V. N. Petrov, M. S. Galaktionov, B. V. Yushenkov, Yu. A. Mamaev, and M. Landolt. Novel compact 60-kV Mott detector for spin-polarization electron spectroscopy. *Technical Physics*, 43(8):991–996, 1998.
- [116] H. C. Siegmann. Emission of polarized electrons from magnetic materials. *Physics Reports*, 17(2):37–76, 1975.
- [117] R. Raue, H. Hopster, and R. Clauberg. Observation of Spin-Split Electronic States in Solids by Energy-, Angle-, and Spin-Resolved Photoemission. *Phys. Rev. Lett.*, 50(20):1623–1626, 1983.
- [118] Fabian Meier, J. Hugo Dil, Jorge Lobo-Checa, Luc Patthey, and Jürg Osterwalder. Quantitative vectorial spin analysis in angle-resolved photoemission: Bi/Ag(111) and Pb/Ag(111). *Physical Review B*, 77(16):165431, 2008.
- [119] Y. A. Bychkov and E. I. Rashba. Properties of a 2D Electron Gas with Lifted Spectral Degeneracy. *JETP Lett.*, 39(2):78–83, 1984.
- [120] M. Z. Hasan and C. L. Kane. Colloquium: Topological insulators. *Reviews of Modern Physics*, 82(4), 2010.
- [121] Gabriel Landolt, Steffen Schreyeck, Sergey V. Eremeev, Bartosz Slomski, Stefan Muff, Jürg Osterwalder, Evgueni V. Chulkov, Charles Gould, Grzegorz Karczewski, Karl Brunner, Hartmut Buhmann, Laurens W. Molenkamp, and J. Hugo Dil. Spin Texture of Bi<sub>2</sub>Se<sub>3</sub> Thin Films in the Quantum Tunneling Limit. *Phys. Rev. Lett.*, 112(5):057601, 2014.
- [122] Z.-H. Zhu, C. N. Veenstra, S. Zhdanovich, M. P. Schneider, T. Okuda, K. Miyamoto, S.-Y. Zhu, H. Namatame, M. Taniguchi, M. W. Haverkort, I. S. Elfimov, and A. Damascelli. Photoelectron Spin-Polarization Control in the Topological Insulator Bi<sub>2</sub>Se<sub>3</sub>. *Phys. Rev. Lett.*, 112(7):76802, 2014.
- [123] Ji Hoon Ryoo and Cheol-Hwan Park. Spin-conserving and reversing photoemission from the surface states of Bi<sub>2</sub>Se<sub>3</sub> and Au (111). *Phys. Rev. B*, 93(8):85419, 2016.

- [124] K. Kuroda, K. Yaji, M. Nakayama, A. Harasawa, Y. Ishida, S. Watanabe, C.-T. Chen, T. Kondo, F. Komori, and S. Shin. Coherent control over three-dimensional spin polarization for the spin-orbit coupled surface state of Bi<sub>2</sub>Se<sub>3</sub>. *Phys. Rev. B*, 94(16):165162, 2016.
- [125] R. Feder. Spin-polarised low-energy electron diffraction. *Journal of Physics C: Solid State Physics*, 14(15):2049, 1981.
- [126] Fabian Meier, Vladimir Petrov, Hossein Mirhosseini, Luc Patthey, Jürgen Henk, Jürg Osterwalder, and J. Hugo Dil. Interference of spin states in photoemission from Sb/Ag(111) surface alloys. *Journal of Physics: Condensed Matter*, 23(7):72207, 2011.
- [127] N. A. Cherepkov. *Spin polarization of atomic and molecular photoelectrons*, volume 19 of *Advances in Atomic and Molecular Physics*. Elsevier, 1983.
- [128] E. Tamura and R. Feder. Spin-polarized normal photoemission from non-magnetic (111)-surfaces by p-polarized light. *Solid State Communications*, 79(11):989–993, 1991.
- [129] Uwe Becker and David A. Shirley, editors. *VUV and Soft X-Ray Photoionization*. Springer US, Boston, MA, 1996.
- [130] U Fano. Spin Orientation of Photoelectrons Ejected by Circularly Polarized Light. *Phys. Rev.*, 178(1):131–136, 1969.
- [131] U. Heinzmann, G. Schönhense, and J. Kessler. Polarization of Photoelectrons Ejected by Unpolarized Light from Xenon Atoms. *Phys. Rev. Lett.*, 42(24):1603–1605, 1979.
- [132] B. Schmidtke, M. Drescher, N. A. Cherepkov, and U. Heinzmann. On the impossibility to perform a complete valence-shell photoionization experiment with closed-shell atoms. *Journal of Physics B: Atomic, Molecular and Optical Physics*, 33(13):2451, 2000.
- [133] N. A. Cherepkov and S. K. Semenov. On a complete experiment on photoionization of atoms. *Journal of Physics B: Atomic, Molecular and Optical Physics*, 37(6):1267, 2004.
- [134] N. A. Cherepkov. Complete experiments in photoionization of atoms and molecules. *Journal of Electron Spectroscopy and Related Phenomena*, 144-147(Supplement C):1197–1201, 2005.
- [135] G. Schönhense. Angular Dependence of the Polarization of Photoelectrons Ejected by Plane-Polarized Radiation from Argon and Xenon Atoms. *Phys. Rev. Lett.*, 44(10):640–643, 1980.
- [136] Daniel T. Pierce and Felix Meier. Photoemission of spin-polarized electrons from GaAs. *Phys. Rev. B*, 13(12):5484–5500, 1976.
- [137] E. Tamura, W. Piepke, and R. Feder. New spin-polarization effect in photoemission from nonmagnetic surfaces. *Physical Review Letters*, 59(8):934–937, 1987.
- [138] B. Schmiedeskamp, B. Vogt, and U. Heinzmann. Experimental verification of a new spin-polarization effect in photoemission: Polarized photoelectrons from Pt(111) with linearly polarized radiation in normal incidence and normal emission. *Phys. Rev. Lett.*, 60(7):651–654, 1988.
- [139] E. Tamura and R. Feder. Spin Polarization in Normal Photoemission by Linearly Polarized Light from Nonmagnetic (001) Surfaces. *Europhysics Letters*, 16(7):695–700, 1991.
- [140] J. B. Pendry. Theory of inverse photoemission. *Journal of Physics C: Solid State Physics*, 14(9):1381, 1981.
- [141] Markus Donath. Spin-dependent electronic structure at magnetic surfaces: the low-Miller-index surfaces of nickel. *Surface Science Reports*, 20(5):251–316, 1994.
- [142] H. Wortelen, H. Mirhosseini, K. Miyamoto, A. B. Schmidt, J. Henk, and M. Donath. Tuning the spin signal from a highly symmetric unpolarized electronic state. *Phys. Rev. B*, 91(11):115420, mar 2015.
- [143] J. Henk and R. Feder. Spin Polarization in Normal Photoemission by Linearly Polarized Light from Non-Magnetic (110) Surfaces. *Europhysics Letters*, 28(8):609–614, 1994.
- [144] N. A. Cherepkov and V. V. Kuznetsov. Fixed-molecule photoelectron angular distributions with defined spin polarisation. *Journal of Physics B: Atomic and Molecular Physics*, 20(5):L159, 1987.

## Bibliography

---

- [145] Mauro Fanciulli, Henrieta Volfová, Stefan Muff, Jürgen Braun, Hubert Ebert, Jan Minár, Ulrich Heinzmann, and J. Hugo Dil. Spin polarization and attosecond time delay in photoemission from spin degenerate states of solids. *Phys. Rev. Lett.*, 118(6):067402, 2017.
- [146] N. Irmer, F. Frentzen, S.-W. Yu, B. Schmiedeskamp, and U. Heinzmann. A new effect in spin-resolved photoemission from Pt(110) in normal emission by linearly polarized VUV-radiation. *Journal of Electron Spectroscopy and Related Phenomena*, 78:321–324, 1996.
- [147] S.-W. Yu, R. David, N. Irmer, B. Schmiedeskamp, N. Müller, U. Heinzmann, and N. A. Cherepkov. Determination of phase differences of transition matrix elements from Pt(110) by means of spin-resolved photoemission with circularly and linearly polarized radiation. *Surface Science*, 416(3):396–402, 1998.
- [148] H. Kramers. Théorie générale de la rotation paramagnétique dans les cristaux. *Proc. Amsterdam Akad.*, 33:959–972, 1930.
- [149] Martin Gradhand, Michael Czerner, Dmitry V. Fedorov, Peter Zahn, Bogdan Yu. Yavorsky, László Szunyogh, and Ingrid Mertig. Spin polarization on Fermi surfaces of metals by the KKR method. *Phys. Rev. B*, 80(22):224413, 2009.
- [150] C. M. Schneider, J. Garbe, K. Bethke, and J. Kirschner. Symmetry-dependent alignment of the electron-spin polarization vector due to electronic band hybridization observed in photoemission from Ag(100). *Phys. Rev. B*, 39(2):1031–1035, 1989.
- [151] E. Tamura, R. Feder, B. Vogt, B. Schmiedeskamp, and U. Heinzmann. Spin-resolved photoemission from Ag(111): Theory and experiment. *Zeitschrift für Physik B Condensed Matter*, 77(1):129–133, 1989.
- [152] N. Irmer, R. David, B. Schmiedeskamp, and U. Heinzmann. Experimental verification of a spin effect in photoemission: polarized electrons due to phase-shift differences in the normal emission from Pt(100) by unpolarized radiation. *Phys. Rev. B*, 45(7):3849–3852, 1992.
- [153] Koichiro Yaji, Kenta Kuroda, Sogen Toyohisa, Ayumi Harasawa, Yukiaki Ishida, Shuntaro Watanabe, Chuangtian Chen, Katsuyoshi Kobayashi, Fumio Komori, and Shik Shin. Spin-dependent quantum interference in photoemission process from spin-orbit coupled states. *Nature Communications*, 8:14588, 2017.
- [154] Cheol-Hwan Park and Steven G. Louie. Spin polarization of photoelectrons from topological insulators. *Physical Review Letters*, 109(9):097601, 2012.
- [155] Neil W. Ashcroft and N. David Mermin. *Solid State Physics*. Cengage Learning, 1976.
- [156] F. Reinert, G. Nicolay, S. Schmidt, D. Ehm, and S. Hüfner. Direct measurements of the L-gap surface states on the (111) face of noble metals by photoelectron spectroscopy. *Phys. Rev. B*, 63(11):115415, 2001.
- [157] J. Hugo Dil, Fabian Meier, and Jürg Osterwalder. Rashba-type spin splitting and spin interference of the Cu(111) surface state at room temperature. *Journal of Electron Spectroscopy and Related Phenomena*, 201:42–46, 2015.
- [158] K. Ishizaka, M. S. Bahramy, H. Murakawa, M. Sakano, T. Shimojima, T. Sonobe, K. Koizumi, S. Shin, H. Miyahara, A. Kimura, K. Miyamoto, T. Okuda, H. Namatame, M. Taniguchi, R. Arita, N. Nagaosa, K. Kobayashi, Y. Murakami, R. Kumai, Y. Kaneko, Y. Onose, and Y. Tokura. Giant Rashba-type spin splitting in bulk BiTeI. *Nat Mater*, 10(7):521–526, 2011.
- [159] Gabriel Landolt, Sergey V. Eremeev, Yury M. Koroteev, Bartosz Slomski, Stefan Muff, Titus Neupert, Masaki Kobayashi, Vladimir N. Strocov, Thorsten Schmitt, Ziya S. Aliev, Mahammad B. Babanly, Imamaddin R. Amiraslanov, Evgueni V. Chulkov, Jürg Osterwalder, and J. Hugo Dil. Disentanglement of Surface and Bulk Rashba Spin Splittings in Noncentrosymmetric BiTeI. *Phys. Rev. Lett.*, 109(11):116403, 2012.
- [160] A. Kimura, E. E. Krasovskii, R. Nishimura, K. Miyamoto, T. Kadono, K. Kanomaru, E. V. Chulkov, G. Bihlmayer, K. Shimada, H. Namatame, and M. Taniguchi. Strong Rashba-Type Spin Polarization of the Photocurrent from Bulk Continuum States: Experiment and Theory for Bi(111). *Phys. Rev. Lett.*, 105(7):076804, 2010.
- [161] S. Neppel, R. Ernstorfer, E. M. Bothschafter, A. L. Cavalieri, D. Menzel, J. V. Barth, F. Krausz, R. Kienberger, and P. Feulner. Attosecond Time-Resolved Photoemission from Core and Valence States of Magnesium. *Phys. Rev. Lett.*, 109(8):087401, 2012.



- [162] C. Lemell, S. Neppel, G. Wachter, K. Tókési, R. Ernstorfer, P. Feulner, R. Kienberger, and J. Burgdörfer. Real-time observation of collective excitations in photoemission. *Phys. Rev. B*, 91(24):241101, 2015.
- [163] J. Minár. Private communication.
- [164] Aimo Winkelmann, Christian Tusche, A. Akin Ünäl, Martin Ellguth, Jürgen Henk, and Jürgen Kirschner. Analysis of the electronic structure of copper via two-dimensional photoelectron momentum distribution patterns. *New Journal of Physics*, 14(4):43009, 2012.
- [165] J. Henk. Private communication.
- [166] Zhengkun Fu, Lianghai Huang, Zengming Meng, Pengjun Wang, Long Zhang, Shizhong Zhang, Hui Zhai, Peng Zhang, and Jing Zhang. Production of Feshbach molecules induced by spin-orbit coupling in Fermi gases. *Nature Physics*, 10:110, 2013.
- [167] H. Bentmann, H. Maaß, E. E. Krasovskii, T. R. F. Peixoto, C. Seibel, M. Leandersson, T. Balasubramanian, and F. Reinert. Strong Linear Dichroism in Spin-Polarized Photoemission from Spin-Orbit-Coupled Surface States. *Phys. Rev. Lett.*, 119(10):106401, 2017.
- [168] Mauro Fanciulli, Stefan Muff, Andrew P. Weber, and J. Hugo Dil. Spin polarization in photoemission from the cuprate superconductor  $\text{Bi}_2\text{Sr}_2\text{CaCu}_2\text{O}_{8+\delta}$ . *Phys. Rev. B*, 95(24):245125, 2017.
- [169] J. Bardeen, L. N. Cooper, and J. R. Schrieffer. Theory of Superconductivity. *Phys. Rev.*, 108(5):1175–1204, 1957.
- [170] W. L. McMillan. Transition Temperature of Strong-Coupled Superconductors. *Phys. Rev.*, 167(2):331–344, 1968.
- [171] J. G. Bednorz and K. A. Müller. Possible high $T_c$  superconductivity in the Ba-La-Cu-O system. *Zeitschrift für Physik B Condensed Matter*, 64(2):189–193, 1986.
- [172] Wikipedia The free Encyclopedia. "Bismuth strontium calcium copper oxide".
- [173] Chandra Varma. Mind the pseudogap. *Nature*, 468:184, 2010.
- [174] Y.-D. Chuang, A. D. Gromko, A. Fedorov, Y. Aiura, K. Oka, Y. Ando, H. Eisaki, S. I. Uchida, and D. S. Dessau. Doubling of the Bands in Overdoped  $\text{Bi}_2\text{Sr}_2\text{CaCu}_2\text{O}_{8+\delta}$ : Evidence for c-Axis Bilayer Coupling. *Phys. Rev. Lett.*, 87(11):117002, 2001.
- [175] P. D. Johnson, A. V. Fedorov, and T. Valla. Photoemission studies of self-energy effects in cuprate superconductors. *Journal of Electron Spectroscopy and Related Phenomena*, 117–118:153–164, 2001.
- [176] Andrea Damascelli, Zahid Hussain, and Zhi-Xun Shen. Angle-resolved photoemission studies of the cuprate superconductors. *Rev. Mod. Phys.*, 75(2):473–541, 2003.
- [177] T. J. Reber, N. C. Plumb, Z. Sun, Y. Cao, Q. Wang, K. McElroy, H. Iwasawa, M. Arita, J. S. Wen, Z. J. Xu, G. Gu, Y. Yoshida, H. Eisaki, Y. Aiura, and D. S. Dessau. The origin and non-quasiparticle nature of Fermi arcs in  $\text{Bi}_2\text{Sr}_2\text{CaCu}_2\text{O}_{8+\delta}$ . *Nat Phys*, 8(8):606–610, 2012.
- [178] H. Anzai, A. Ino, M. Arita, H. Namatame, M. Taniguchi, M. Ishikado, K. Fujita, S. Ishida, and S. Uchida. Relation between the nodal and antinodal gap and critical temperature in superconducting  $\text{Bi}_2\text{212}$ . *Nature Communications*, 4:1815, 2013.
- [179] Makoto Hashimoto, Inna M. Vishik, Rui-Hua He, Thomas P. Devereaux, and Zhi-Xun Shen. Energy gaps in high-transition-temperature cuprate superconductors. *Nat Phys*, 10(7):483–495, 2014.
- [180] N. B. Brookes, G. Ghiringhelli, O. Tjernberg, L. H. Tjeng, T. Mizokawa, T. W. Li, and A. A. Menovsky. Detection of Zhang-Rice Singlets Using Spin-Polarized Photoemission. *Phys. Rev. Lett.*, 87(23):237003, 2001.
- [181] S. Weyeneth, T. Schneider, and E. Giannini. Evidence for Kosterlitz-Thouless and three-dimensional XY critical behavior in  $\text{Bi}_2\text{Sr}_2\text{CaCu}_2\text{O}_{8+\delta}$ . *Phys. Rev. B*, 79(21):214504, 2009.
- [182] A. Piriou, E. Giannini, Y. Fasano, C. Senatore, and O. Fischer. Vortex phase diagram and temperature-dependent second-peak effect in overdoped  $\text{Bi}_2\text{Sr}_2\text{CuO}_{6+\delta}$  crystals. *Phys. Rev. B*, 81(14):144517, 2010.
- [183] H. Ding, A. F. Bellman, J. C. Campuzano, M. Randeria, M. R. Norman, T. Yokoya, T. Takahashi, H. Katayama-Yoshida, T. Mochiku, K. Kadowaki, G. Jennings, and G. P. Brivio. Electronic Excitations in  $\text{Bi}_2\text{Sr}_2\text{CaCu}_2\text{O}_{8+\delta}$ : Fermi Surface, Dispersion, and Absence of Bilayer Splitting. *Phys. Rev. Lett.*, 76(9):1533–1536, 1996.

## Bibliography

---

- [184] T. Kiss, T. Shimojima, K. Ishizaka, A. Chainani, T. Togashi, T. Kanai, X.-Y. Wang, C.-T. Chen, S. Watanabe, and S. Shin. A versatile system for ultrahigh resolution, low temperature, and polarization dependent Laser-angle-resolved photoemission spectroscopy. *Review of Scientific Instruments*, 79(2):23106, 2008.
- [185] Tadashi Togashi, Teruto Kanai, Taro Sekikawa, Shuntaro Watanabe, Chuangtian Chen, Chengqian Zhang, Zuyan Xu, and Jiyang Wang. Generation of vacuum-ultraviolet light by an optically contacted, prism-coupled KBe<sub>2</sub>BO<sub>3</sub>F<sub>2</sub> crystal. *Opt. Lett.*, 28(4):254–256, 2003.
- [186] Chuangtian Chen. Recent advances in deep and vacuum-UV harmonic generation with KBBF crystal. *Optical Materials*, 26(4):425–429, 2004.
- [187] Wikipedia The free Encyclopedia. "Universe".
- [188] Loren Greenman, Phay J. Ho, Stefan Pabst, Eugene Kamarchik, David A. Mazziotti, and Robin Santra. Implementation of the time-dependent configuration-interaction singles method for atomic strong-field processes. *Phys. Rev. A*, 82(2):23406, 2010.
- [189] Stefan Pabst, Loren Greenman, Phay J. Ho, David A. Mazziotti, and Robin Santra. Decoherence in Attosecond Photoionization. *Phys. Rev. Lett.*, 106(5):053003, 2011.
- [190] Anthony F. Starace. Trends in the theory of atomic photoionization. *Appl. Opt.*, 19(23):4051–4062, 1980.
- [191] Renate Pazourek, Stefan Nagele, and Joachim Burgdorfer. Time-resolved photoemission on the attosecond scale: opportunities and challenges. *Faraday Discuss.*, 163(0):353–376, 2013.
- [192] S. Nagele, R. Pazourek, J. Feist, and J. Burgdörfer. Time shifts in photoemission from a fully correlated two-electron model system. *Phys. Rev. A*, 85(3):033401, 2012.
- [193] C.-H. Zhang and U. Thumm. Electron-ion interaction effects in attosecond time-resolved photoelectron spectra. *Phys. Rev. A*, 82(4):043405, 2010.
- [194] C. H. Zhang and U. Thumm. Streaking and Wigner time delays in photoemission from atoms and surfaces. *Phys. Rev. A*, 84(3):033401, 2011.
- [195] Maximilian Schlosshauer. Decoherence, the measurement problem, and interpretations of quantum mechanics. *Rev. Mod. Phys.*, 76(4):1267–1305, 2005.
- [196] Jérémie Caillat, Alfred Maquet, Stefan Haessler, Baptiste Fabre, Thierry Ruchon, Pascal Salières, Yann Mairesse, and Richard Taïeb. Attosecond Resolved Electron Release in Two-Color Near-Threshold Photoionization of N<sub>2</sub>. *Phys. Rev. Lett.*, 106(9):93002, 2011.
- [197] Romain Gaillac, Morgane Vacher, Alfred Maquet, Richard Taïeb, and Jérémie Caillat. Attosecond photoemission dynamics encoded in real-valued continuum wave functions. *Phys. Rev. A*, 93(1):13410, 2016.
- [198] C. Tusche, M. Ellguth, A. A. Ünal, C.-T. Chiang, A. Winkelmann, A. Krasnyuk, M. Hahn, G. Schönhense, and J. Kirschner. Spin resolved photoelectron microscopy using a two-dimensional spin-polarizing electron mirror. *Applied Physics Letters*, 99(3):32505, 2011.
- [199] E. L. Wolf. *Graphene: A New Paradigm in Condensed Matter and Device Physics*. Oxford University Press, 2013.
- [200] Isabella Gierz, Jürgen Henk, Hartmut Höchst, Christian R. Ast, and Klaus Kern. Illuminating the dark corridor in graphene: Polarization dependence of angle-resolved photoemission spectroscopy on graphene. *Phys. Rev. B*, 83(12):121408, 2011.
- [201] Aaron Bostwick, Taisuke Ohta, Thomas Seyller, Karsten Horn, and Eli Rotenberg. Quasiparticle dynamics in graphene. *Nature Physics*, 3:36, 2006.

# Curriculum Vitæ

*Name* Mauro Fanciulli  
*Nationality* Italian  
*Birth* 22<sup>nd</sup> May 1989, Porto Ercole, Italy



## Education

- 2014-2018 ◇ **Ph.D. in Physics** at École Polytechnique Fédérale de Lausanne (CH)
- *Secondary affiliation:* Swiss Light Source, Paul Scherrer Institut, Villigen (CH)
  - *Advisor:* Prof. J. Hugo Dil
  - *Dissertation:* Spin polarization and attosecond time delay in photoemission from solids
  - Visiting student at University of Tokyo in the group of Prof. Shik Shin (2 weeks)
  - *Other projects:* Multiferroic Rashba systems, transition metal dichalcogenides, transition metal oxides, topological insulators, Weyl semimetals
- 2011-2013 ◇ **Master's Degree in Physics Engineering** at Politecnico di Milano (IT)
- *Training:* European Synchrotron Radiation Facility, Grenoble, France (7 months)
  - *Advisor:* Prof. Giacomo Ghiringhelli
  - *M.Sc. Thesis:* Spin-Orbit and Crystal Field excitations in Ce compounds probed by Resonant Inelastic X-ray Scattering (<http://hdl.handle.net/10589/88641>)
  - *Mark:* 110/110
- 2008-2011 ◇ **Bachelor's Degree in Physics Engineering** at Politecnico di Milano (IT)
- *Advisor:* Prof. Marco Finazzi
  - *B.Sc. Thesis:* Scanning Probe Optical Microscopy on metal nanostructures
  - *Mark:* 101/110
- 2003-2008 ◇ **High School diploma in scientific studies** at Liceo Scientifico G. Marconi, Grosseto (IT)
- *Mark:* 100/100 with honors
- **Doctoral School**
- 2 *etcs*, Using Mathematica to analyze and model experimental data, EPFL
  - 2 *etcs*, Wien2k Workshop, Université de Nantes (FR)
  - 2 *etcs*, Adv. exper. methods in cond. matt. and nanophys., Max Plank Stuttgart (D)
  - 2 *etcs*, Shedding light on correl. electrons, 6th MaNEP Winter School, Saas Fee (CH)
  - 3 *etcs*, Electronic Properties of Solids and Superconductivity, EPFL
  - 4 *etcs*, School on UV and X-ray spectrosc. of correl. electron systems, Les Houches (FR)

# Experience and interests

### Teaching

Teaching assistant at the EPFL for 7 semesters for different Bachelor programs. The main tasks were: preparation of the exercises, discussion at the blackboard and interaction with the students (2h/week), preparation and correction of the final exams.

- Electromagnetism, Computer Science, fall a.y. 14/15, 15/16, 16/17, 17/18, Prof. J. H. Dil
- Thermodynamics, Chemistry Engineering, spring a.y. 14/15, Prof. G. Margaritondo
- Quantum mechanics, Electronic Engineering, spring a.y. 15/16, 16/17, Prof. M. Grioni

### Experimental skills

- Large user facilities @ SLS (CH), ESRF (FR), MAX3 (SE), BNL (US), SOLEIL (FR)
- Ultra High Vacuum (UHV) tech @ SLS, EPFL, ESRF, MAX3, BNL, SOLEIL, UniTokyo (JP)
- Angle Resolved Photoemission Spectroscopy (ARPES) @ SLS, EPFL, UniTokyo
- Spin-resolved ARPES @ SLS, MAX3
- Spin-resolved laser ARPES @ UniTokyo
- Soft X-ray ARPES @ SLS
- Micro and Nano ARPES @SOLEIL
- Resonant Inelastic X-ray Scattering (RIXS) @ ESRF
- Low Energy Electron Diffraction (LEED) @ SLS, EPFL, BNL
- Low Energy Electron Microscopy (LEEM) @ BNL
- X-ray Linear Dichroism, X-ray Magnetic Circular Dichroism (XLD, XMCD) @ SLS, ESRF
- Extended X-ray Absorption Fine Structure (EXAFS) @ ESRF
- X-ray Photoelectron Diffraction (XPD) @SLS

### Computer skills

- Wolfram Mathematica
- Matlab
- Igor Pro
- Origin Pro

### Language skills

- Italian (mother tongue)
- English (professional)
- French (daily conversation)

### Interests

*Scientific* Spin- and time-resolved photoelectron spectroscopies, laser and synchrotron-based spectroscopies, spin interference, topology, correlations, fundamental aspects of QM

*Personal* Theater and literature, hiking, jazz piano, photography, board games, comics, running, tennis, table tennis, bouldering

## Public presentations

- 2015 • *Poster session*, New Trends in Topological Insulators (NTTI), San Sebastian, Spain
- 2016 • *Poster session*, Vacuum Ultraviolet and X-ray Physics (VUVX), Zurich, Switzerland
- *Contributed talk*, Swiss Physical Society Annual Meeting (SPS), Lugano, Switzerland
  - *Contributed talk*, European Conference On Surface Science (ECOSS), Grenoble, France
- 2017 • *Contributed talk*, German Physical Society Annual Meeting (DPG), Dresden, Germany
- *Invited Seminar*, Dep. of Phys., Ludwig Maximilians Univ. (LMU), Munich, Germany
  - *Invited Seminar*, Dep. of Phys., Technische Univ. München (TUM), Garching, Germany
  - *Poster session*, New Trends in Topological Insulators (NTTI), Ascona, Switzerland
  - *Oral presentation*, School on UV spectr. of correl. electr. syst., Les Houches, France
  - *Poster session*, Physics day EPFL, Lausanne, Switzerland
  - *Contributed talk*, Electr. and spin dynam. in corr. syst., Cergy-Pontoise, France
- 2018 • *Contributed talk*, German Physical Society Annual Meeting (DPG), Berlin, Germany

## Publications

1. **M. Fanciulli** and J. H. Dil, *Determination of the time scale of photoemission from the measurement of the spin polarization*, in preparation
2. **M. Fanciulli**, A. Zeugner, S. Muff, A. P. Weber, H. Bentmann, A. Isaeva and J. H. Dil, *Angle-resolved photoemission spectroscopy study of Bi<sub>2</sub>TeI*, in preparation
3. A. P. Weber, P. Rüßmann, N. Xu, S. Muff, **M. Fanciulli**, A. Magrez, P. Bugnon, H. Berger, N. C. Plumb, M. Shi, S. Blügel, P. Mavropoulos and J. H. Dil, *Three-dimensional spin-texture in T<sub>d</sub>-MoTe<sub>2</sub> with response to a polar lattice transition*, in review
4. J. Krempaský, S. Muff, J. Minár, N. Pilet, **M. Fanciulli**, A. P. Weber, V. V. Volobuiev, M. Gmitra, C. A. F. Vaz, V. Scagnoli, G. Springholz and J. H. Dil, *Operando imaging of all-electric spin texture manipulation in ferroelectric and multiferroic Rashba semiconductors*, in review
5. S. Muff, N. Pilet, **M. Fanciulli**, A. P. Weber, C. Wessler, Z. Ristić, Z. Wang, N. C. Plumb, M. Radović and J. H. Dil, *Observation of Wannier-Stark localization at the surface of BaTiO<sub>3</sub> films by photoemission*, in review
6. J. Krempaský, **M. Fanciulli**, N. Pilet, J. Minár, W. Khan, M. Muntwiler, F. Bertran, S. Muff, A. P. Weber, V. N. Strocov, V. V. Volobuiev, G. Springholz and J. H. Dil, *Spin-resolved electronic structure of ferroelectric  $\alpha$ -GeTe and multiferroic Ge<sub>1-x</sub>Mn<sub>x</sub>Te*, Journal of Physics and Chemistry of Solids, online <https://doi.org/10.1016/j.jpics.2017.11.010>, in press
7. P. Rüßmann, A. P. Weber, F. Glott, N. Xu, **M. Fanciulli**, S. Muff, A. Magrez, P. Bugnon, H. Berger, M. Bode, J. H. Dil, S. Blügel, P. Mavropoulos and P. Sessi, *Universal scattering response across the type-II Weyl semimetal phase diagram*, Physical Review B 97, 075106 (2018)

8. S. Muff, M. Fanciulli, A. P. Weber, N. Pilet, Z. Ristić, Z. Wang, N. C. Plumb, M. Radović and J. H. Dil, *Observation of a two-dimensional electron gas at CaTiO<sub>3</sub> film surfaces*, Applied Surface Science, 432A, 41 (2018)
9. C. Brand, S. Muff, M. Fanciulli, H. Pfnür, M. C. Tringides, J. H. Dil and C. Tegenkamp, *Spin-resolved band structure of a densely packed Pb monolayer on Si(111)*, Physical Review B 96, 035432 (2017)
10. M. Fanciulli, S. Muff, A. P. Weber, and J. H. Dil, *Spin polarization in photoemission from the cuprate superconductor Bi<sub>2</sub>Sr<sub>2</sub>CaCu<sub>2</sub>O<sub>8+δ</sub>*, Physical Review B 95, 245125 (2017)
11. E. Razzoli, T. Jaouen, M.-L. Mottas, B. Hildebrand, G. Monney, A. Pisoni, S. Muff, M. Fanciulli, N. C. Plumb, V. A. Rogalev, V. N. Strocov, J. Mesot, M. Shi, J. H. Dil, H. Beck and P. Aebi, *Selective Probing of Hidden Spin-Polarized States in Inversion-Symmetric Bulk MoS<sub>2</sub>*, Physical Review Letters 118, 086402 (2017)
12. M. Fanciulli, H. Volfová, S. Muff, J. Braun, H. Ebert, J. Minár, U. Heinzmann, and J. H. Dil, *Spin Polarization and Attosecond Time Delay in Photoemission from Spin Degenerate States of Solids*, Editors' suggestion, Physical Review Letters 118, 067402 (2017)
13. J. Krempaský, S. Muff, F. Bisti, M. Fanciulli, H. Volfová, A. P. Weber, N. Pilet, P. Warnicke, H. Ebert, J. Braun, F. Bertran, V. V. Volobuev, J. Minár, G. Springholz, J. H. Dil and V. N. Strocov, *Entanglement and manipulation of the magnetic and spin-orbit order in multiferroic Rashba semiconductors*, Nature Communications, 7, 13071 (2016)
14. S.-K. Mo, C. Hwang, Y. Zhang, M. Fanciulli, S. Muff, J. H. Dil, Z.-X. Shen and Z. Hussain, *Spin-resolved photoemission study of epitaxially grown MoSe<sub>2</sub> and WSe<sub>2</sub> thin films*, J. Phys. Cond. Matt. 28,454001 (2016)
15. A. Amorese, G. Dellea, M. Fanciulli, S. Seiro, C. Geibel, C. Krellner, I. P. Makarova, L. Braicovich, G. Ghiringhelli, D. V. Vyalikh, N. B. Brookes, and K. Kummer, *4f excitations in Ce Kondo lattices studied by resonant inelastic x-ray scattering*, Physical Review B 93, 165134 (2016)

